Economic Geology

BULLETIN OF THE SOCIETY OF ECONOMIC GEOLOGISTS

VOL. 101 December 2006 NO. 8

Geology of the Sari Gunay Epithermal Gold Deposit, Northwest Iran*

JEREMY P. RICHARDS,†

Department of Earth and Atmospheric Sciences, University of Alberta, Edmonton, Alberta, Canada T6G 2E3

DAMIEN WILKINSON,

Rio Tinto Minera Peru Limitada SAC, Av. Larco 1301, office 2102, Miraflores, Lima 18, Peru

AND THOMAS ULLRICH

Pacific Centre for Isotopic and Geochemical Research, Earth and Ocean Sciences, University of British Columbia, 6339 Stores Road, Vancouver, British Columbia, Canada V6T 1Z4

Abstract

The Sari Gunay epithermal gold deposit is located within a mildly alkaline latitic to trachytic volcanic complex in central-northwest Iran. Intrusive and volcanic rocks that host the deposit have been dated at between 11.7 and 11.0 Ma (with one younger sample at 8.0 Ma; $^{40}Ar/^{39}Ar$ dating of igneous biotite and hornblende), whereas sericitic alteration associated with an early stage of hydrothermal activity occurred between ~10.8 and ~10.3 Ma (the best age estimate is 10.7 Ma obtained by $^{40}Ar/^{39}Ar$ dating of sericite). The main hydrothermal system was structurally localized by a diatreme breccia complex centered on the Sari Gunay hill. Earliest hydrothermal activity, only encountered at depth (>300 m below surface), produced weak potassic alteration and quartz-sulfide-magnetite veining with low grades of Cu and Au mineralization, reminiscent of shallow-level (≤1.5-km depth) porphyry gold systems. Paragenetically later quartz-tourmaline breccias and veins followed the south-southwest–north-northeast trend of the diatreme breccias and produced strong sericitic alteration and silicification in igneous clasts and wall rocks. Fluid inclusions indicate temperatures of 246° to 360°C and salinities of 34.4 to 46.1 wt percent NaCl equiv in hypersaline inclusions coexisting with low-density, CO_2-bearing vapor-phase inclusions. These fluids do not appear to have deposited gold, but the breccias provided further structural permeability for flow of later mineralizing epithermal fluids.

Invisible gold occurs in solid solution in fine-grained arsenical pyrite and minor arsenopyrite, deposited in the early stages of quartz-adularia-pyrite-stibnite veins. Late-stage minerals in these veins include realgar, orpiment, cinnabar, and extremely rare wire gold. Liquid-rich fluid inclusions in these veins have an average homogenization temperature (≈trapping temperature) of 199° ± 24°C, salinities of 3.6 ± 1.1 wt percent NaCl equiv, and coexist with low-density CO_2-bearing vapor-phase inclusions, suggesting low-pressure conditions. Phase separation may have been a contributory cause of gold deposition, but precipitation of sulfides in response to rapid cooling of the system may have been the main control on deposition of pyrite-hosted gold.

The Sari Gunay gold deposit and its host volcanic system form part of the Takab belt of structurally controlled, middle Miocene, mildly alkaline volcano-plutonic complexes. The sediment-hosted Zarshuran gold deposit, located ~190 km to the north-northwest along the belt, is also related to middle Miocene magmatism. The Takab belt is marginally younger than, and displaced to the southwest of, the extensive Eocene-Miocene Urumieh-Dokhtar calk-alkaline volcanic arc, which hosts several large porphyry Cu deposits (e.g., Sar Cheshmeh, Meiduk). Rocks of the Takab belt are also distinctly more alkaline than the Urumieh-Dokhtar rocks. Viewed in the context of plate tectonic models for Neogene closure of a Neo-Tethys ocean between the Afro-Arabian and Eurasian plates, these differences may reflect a normal subduction zone origin for the Urumieh-Dokhtar arc and contained porphyry Cu deposits but a collisional origin for the slightly younger Takab belt volcanic rocks and epithermal gold deposits. The Sari Gunay deposit may thus be classified as a collision-related alkalic-type epithermal system, although it is less alkaline than classic deposits of this group such as Porgera, Emperor, or Cripple Creek (the latter apparently being related to postcollisional or back-arc extensional rather than syncollisional processes).

* A digital supplement with fluid inclusion data is available at<http://segweb.org/EG/papers/Abs 101-8_files/RichardsAppendix.pdf>.

† Corresponding author: e-mail, Jeremy.Richards@ualberta.ca

Vol. 101, pp.1455–1496
0361-0128/06/3630/1455-42

Introduction

Sari Gunay is a subvolcanic intrusion-related epithermal gold deposit, formed within a middle Miocene, high K subalkaline volcanic complex in central-northwestern Iran. It is located at 35°12'N 48°05'E in the province of Kordestan, ~60 km northwest of the city of Hamedan, in a region of rolling hills and semiarid, marginal farmland (Fig. 1). Prior to the discovery of this deposit, the immediate area was not known for gold mineralization, although small stibnite, orpiment, and realgar veins had been worked for antimony and arsenic. Farther to the northwest, however, sediment-hosted but intrusion-related epithermal-style gold deposits are known at Zarshuran and Agh Darreh (Fig. 1). These epithermal deposits are all distant from other known intrusion-related deposits in Iran, such as those in the Kerman porphyry copper belt to the southeast (e.g., Sar Cheshmeh, Meiduk) and the Sungun porphyry Cu deposit in the far northwest of the country (Fig. 1).

The potential for gold mineralization at Sari Gunay was first recognized by Rio Tinto geologists in 1999 during inspection of a site containing antimony-arsenic vein mineralization and old millstone quarries in silicified igneous rocks. Large areas of phyllic and argillic alteration were noted in a 16-km^2 area around the vein system, and samples were taken on the basis of similarities to epithermal-style mineralization. Significant gold values were detected in vein and wall-rock samples collected over a wide area, and Rio Tinto formed a joint venture partnership with the property owner, CESCO, to explore the deposit further. Ownership of the property exploitation license was transferred to the Zar Kuh Mining Company (70% Rio Tinto, 30% CESCO) in 2004, and diamond drilling to date has delineated a resource of 52 million metric tons (Mt) of oxide mineralization containing 1.77 g/t Au (1.0 g/t cutoff) within an area of 600 × 1,200 m and to a depth of at least 350 m.

The Sari Gunay discovery is of interest for several reasons. It is the first significant gold discovery in Iran in recent years and, if developed, will represent one of the first major investments by a foreign mining company in Iran since the Islamic Revolution of 1979. Geologically, the deposit lies off the known trends of middle- to late-Cenozoic arc magmatism and associated (mainly porphyry Cu-style) mineralization and therefore requires a more detailed analysis of tectonic and magmatic history in this region to explain its location.

In this paper, we provide an overview of the deposit geology, combined with geochronological ($^{40}Ar/^{39}Ar$) and whole-rock geochemical data on the host intrusive and extrusive rocks, to characterize the ore-forming system. The origin of the deposit is then discussed in the context of regional geologic history, with special reference to late Cenozoic closure of the Neo-Tethys ocean and related magmatic activity.

Geologic History of the Tethyan Margins in Iran

Iran is located along the Tethyan suture between Eurasia and Africa-Arabia and records the closure of at least two Tethyan oceans, the Paleo-Tethys in the Paleozoic and the Neo-Tethys in the Cenozoic. Detailed tectonic reconstructions are hampered by a paucity of modern geochronological and geochemical data in the region and poor exposure beneath Neogene sediments that cover much of the country.

The Paleo-Tethys ocean opened during the Ordovician and separated China and Indochina from Gondwana (Stampfli, 2000). At this time, Iran was located on the northern seaboard of Gondwana, and subduction occurred beneath this Paleo-Tethyan margin during the Silurian and Carboniferous.

In the Permian, subduction of the Paleo-Tethys ocean switched to the north beneath China-Indochina, and a new ocean basin, Neo-Tethys I, opened in the south, rifting continental fragments including Turkey, Iran, and Tibet from Gondwana (Hooper et al., 1994; Stampfli, 2000). These rifted fragments formed the Cimmerian continent and included the Sanandaj-Sirjan, Central Iranian, and Lut blocks of present-day Iran (Fig. 1).

By the Jurassic, the Paleo-Tethys ocean had been eliminated by subduction beneath the coalescing Eurasian continent, to which the Cimmerian continental fragments became attached. The southern Caspian Sea may be a remnant of this ocean basin, with the suture marked by the southern edge of the Kopet Dagh mountains (Fig. 1). Subduction of the Neo-Tethys I ocean was initiated northward beneath this accreted margin in response to opening of the Atlantic ocean (Hooper et al., 1994; Glennie, 2000). By the Late Cretaceous, southward-directed subduction beneath Arabia and northward-directed subduction beneath Eurasia contributed to the progressive destruction of this section of the Tethys ocean (Fig. 2A). Late Cretaceous calc-alkaline magmatism and related porphyry and epithermal deposits in the Balkans, Turkey, and Azerbaijan may be related to this period of northward subduction.

A small ocean basin, Neo-Tethys II, is suggested to have opened between the Cimmerian continent and Eurasia in the Late Triassic (Fig. 2A; Glennie, 2000), and the Cimmerian continent began to break up to form an archipelago of small microplates (Heydari et al., 2002). Closure of the Neo-Tethys I ocean basin between Arabia and Eurasia was probably a diachronous event, and its timing and the exact location of the suture zone are widely debated in the literature. Glennie (2000) considers that closure was complete by the Late Cretaceous (Maastrichtian), resulting in accretion of the Sanandaj-Sirjan and Lut blocks to the Arabian margin along the Zagros suture zone (Fig. 2A-B). In contrast, Hooper et al. (1994) and Agard et al. (2005) consider that docking occurred by the late Oligocene. Closure of Neo-Tethys I resulted in emplacement of ophiolites along the Zagros suture zone (Stoneley, 1981) and the onset of deformation in the Zagros fold-and-thrust belt.

Subduction of Neo-Tethys II to the north beneath the Urumieh-Dokhtar arc in the Late Cretaceous or Paleocene and arc magmatism along this belt in central Iran became extensive in the Eocene, continuing through the Miocene (Fig. 2C-D; Glennie, 2000; Mohajjel et al., 2003). Porphyry copper-related intrusive activity in the calc-alkaline Urumieh-Dokhtar belt occurred toward the end of this period in the middle Miocene (McInnes et al., 2003; Zarasvandi et al., 2005) and appears to represent the final phase of arc magmatism prior to collision.

Final closure of Neo-Tethys II was probably diachronous, with docking perhaps beginning in the Miocene in the northwest (Fig. 2D), whereas to the southeast docking has not yet occurred, and oceanic lithosphere still exists beneath the Gulf

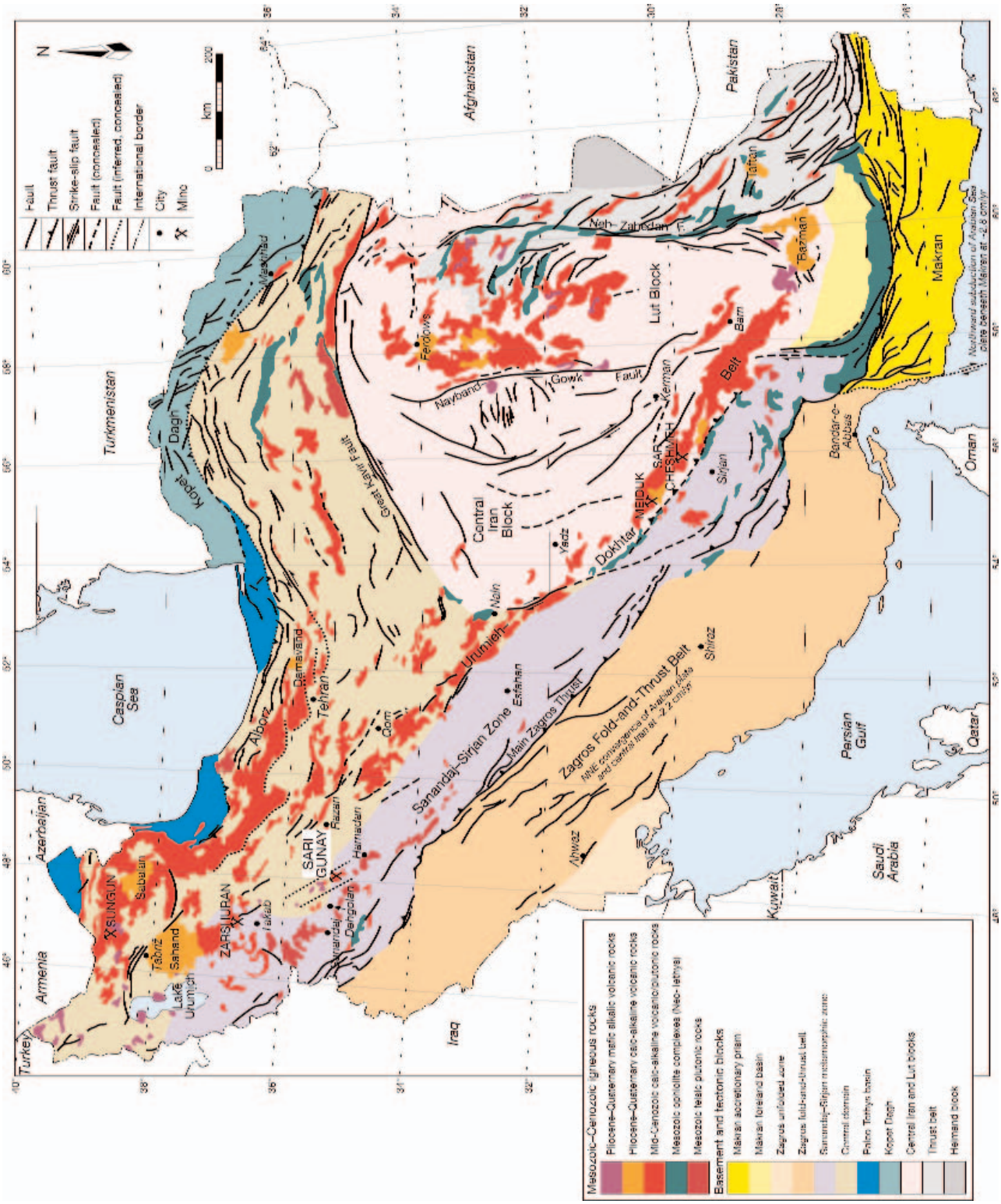

FIG. 1. Geology of Iran, showing the location of Sari Gunay and other major ore deposits and highlighting Mesozoic-Cenozoic igneous rocks and ophiolites. Note that Quaternary sediments cover large areas of Iran and basement and other tectonic blocks are inferred. Based on the 1:2,500,000 geologic map of Iran (Geological Survey of Iran, 1989, and unpub. data), with additional information from Berberian and King (1981), Bonini et al. (2003), Mohajjel et al. (2003), and Regard et al. (2005).

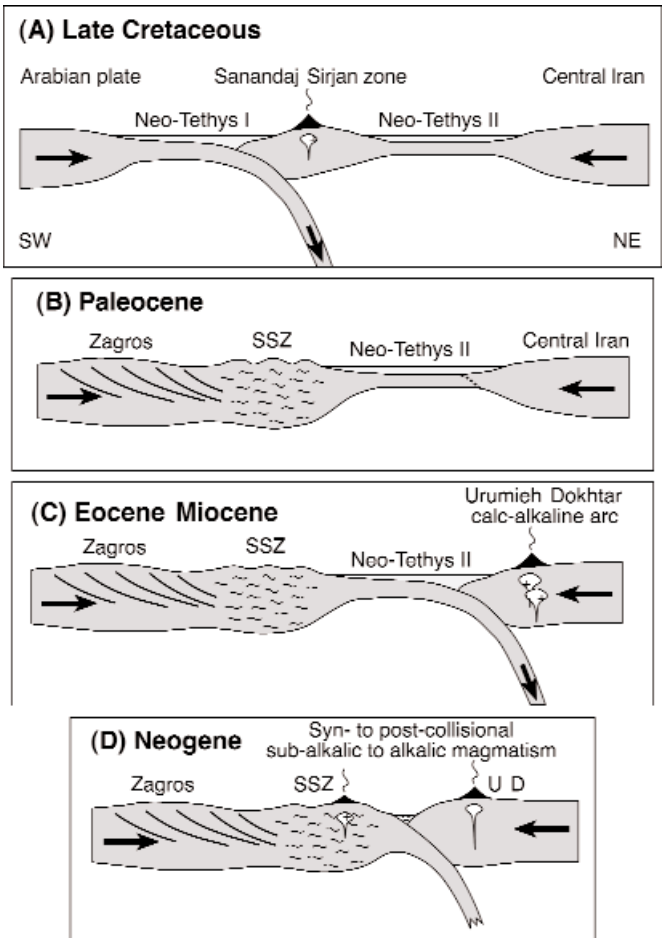

FIG. 2. Schematic cross sections showing (A) subduction of Neo-Tethys I beneath the Sanandaj-Sirjan zone (SSZ) during the Late Cretaceous, (B) closure of Neo-Tethys I during the latest Cretaceous or Paleocene, (C) onset of subduction of putative Neo-Tethys II beneath central Iran during the Eocene-Miocene to form the Urumieh-Dokhtar (U–D) magmatic arc, and (D) collision between the Sanandaj-Sirjan zone and central Iran during the Neogene.

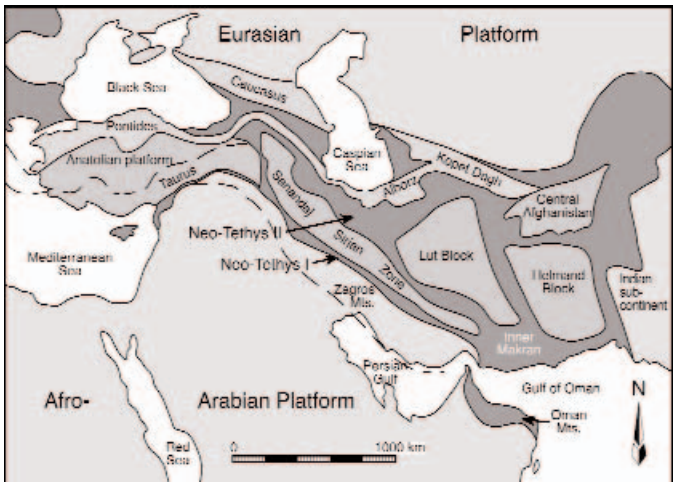

FIG. 3. Plate tectonic map of the Tethyan belt from Turkey to Pakistan (from Richards, 2003a, modified from Glennie, 2000). Areas shown in dark gray contain ophiolitic fragments and are believed to represent former oceanic areas separating small continental blocks (medium gray).

of Oman, subducting beneath the Makran accretionary complex (Fig. 1; Jacob and Quittmeyer, 1979). In southwestern Iran, progressive shortening since the Miocene resulted in crustal thickening and uplift of the Zagros Mountains (Giese et al., 1984; Snyder and Baranzangi, 1986; Glennie, 2000; Agard et al., 2005).

The suture marking closure of the Neo-Tethys II basin is unclear but is interpreted to lie between the Sanandaj-Sirjan zone and the Urumieh-Dokhtar arc where a series of basins with scattered ophiolite outcrops are interpreted to be forearc depressions, laterally equivalent to the Makran accretionary complex (e.g., Stoneley, 1974, 1981; Farhoudi and Karig, 1977; Farhoudi, 1978; McCall and Kidd, 1982; Alavi, 1994). Glennie (2000) based his interpretation of the location of the Neo-Tethys I and Neo-Tethys II sutures on this distribution of ophiolitic fragments (Fig. 3). It should be noted, however, that other reconstructions do not recognize a separate Neo-Tethys II ocean to the north of the Sanandaj-Sirjan zone (e.g., Stoneley, 1981; Alavi, 1994; Hooper et al., 1994; Mohajjel et al., 2003; Shahabpour, 2005). In these models, calc-alkaline magmatism in the Urumieh-Dokhtar belt is related to Neo-Tethys I subduction, although the timing of calc-alkaline magmatism in this belt (Eocene-Miocene) is delayed relative to the presumed Cretaceous-Oligocene(?) timing of Neo-Tethys I subduction and closure. On the other hand, the small size and short history of any Neo-Tethys II ocean, as constrained by global plate tectonic reconstructions, are also inconsistent with the scale and longevity of magmatism in the Urumieh-Dokhtar arc, as is the absence of any other significant magmatic belt related to Neo-Tethys I subduction beneath Iran. The question of a Neo-Tethys II ocean remains unresolved.

Tectonic and magmatic activity since closure of the Zagros section of the Neo-Tethys reflects continued shortening across the orogen, with transpressional deformation in central Iran and sparse but widespread eruption of mafic alkalic lavas throughout the region. The geographic transition between continental collision to the northwest and subduction to the southeast is marked by a complex zone of north-trending strike-slip faults that bound the Lut and Helmand basement blocks in eastern Iran and western Afghanistan (Fig. 1), such that the Lut block appears to be rotated between the dextral Nayband-Gowk and Neh-Zahedan fault systems. Between 2.3 and 3.5 cm/yr of north-northeast-trending convergence along the collisional section of the suture is accommodated in part by contractional deformation in the Zagros fold-and-thrust belt and by deformation in the Alborz-Kopet Dagh mountains that mark the edge of the Eurasian stable platform (Fig. 1; Regard et al., 2005). Further shortening is accommodated by eastward escape of central Iran by strike-slip faulting within a transpressional orogen (Bonini et al., 2003). Movement along these various faults is reflected in the active seismicity of Iran.

Cenozoic Porphyry and Epithermal Mineralization in Iran

The main porphyry copper deposits in Iran occur in the Urumieh-Dokhtar belt (Fig. 1) and are mostly of middle Miocene age, associated with subduction-related calc-alkaline plutonism. In the Kerman section of the Urumieh-Dokhtar

belt, the largest deposit, Sar Cheshmeh, is an operating mine and contains ~1.1 Gt of ore at 0.64 percent Cu and 0.03 percent Mo; it has been dated at 13.6 ± 0.1 Ma (U-Pb zircon; McInnes et al., 2003). The smaller Meiduk deposit (~170 Mt of ore at 0.82% Cu, 0.006% Mo) is currently being stripped prior to production and has a similar middle Miocene U-Pb zircon age of 12.5 ± 0.1 Ma (McInnes et al., 2003). The only other porphyry mine currently being developed in Iran is the Sungun deposit in the far northwest of the country, which is also currently undergoing prestripping. The deposit is estimated to contain 500 Mt of ore at 0.76 percent Cu and 0.01 percent Mo and is also thought to be middle Miocene in age (Hezarkhani and Williams-Jones, 1998; an unpublished age estimate of 12.5 Ma is cited in Hedenquist and Daneshfar, 2001).

Prior to the discovery of Sari Gunay, only a few epithermal gold deposits were known in Iran. The largest of these is the Carlin-like Zarshuran prospect, a sediment-hosted "invisible" gold deposit in northwest Iran (Fig. 1; ~80 t Au at grades of 3–4 g/t: Mehrabi et al., 1999; Asadi, 2000; Asadi et al., 2000a, b; Daliran et al., 2002). Submicroscopic gold is present in arsenian pyrite and sphalerite, disseminated within altered Precambrian carbonates and black shales. Base metal sulfides and sulfosalts, as well as realgar, orpiment, stibnite, and telluride minerals accompany the pyrite as disseminations and in quartz veins. Alteration includes decalcification, silicification, and argillization, and mineralization is inferred to have taken place at temperatures between 350° and 150°C during phase separation in a CO_2-rich aqueous fluid (Asadi, 2000). A K-Ar date of ~14 Ma was obtained from altered metapelite hosting the deposit (Daliran et al., 2002). These lithologic units are intruded by an Oligocene to Miocene granitoid, which is also altered and locally mineralized, and a relationship between this intrusive event and mineralization has been suggested by Asadi et al. (2000b) and Daliran et al. (2002). Similar mineralization occurs nearby at the Agh Darreh deposit (~50 t Au at grades of 3–4 g/t: Daliran et al., 2002). As is shown below, the age and style of mineralization, if not the predominant host rock, are similar to those found at Sari Gunay.

High-sulfidation alteration has been reported in the western Alborz, where hydrothermal kaolinite, alunite, and vuggy quartz deposits occur in volcanic rocks at Takand and in the Qazvin-Rasht area (Förster, 1978), possibly related to underlying intrusive activity (B. Samani, pers. commun., 2002). Intermediate-sulfidation Au-Ag and base metal sulfide deposits have also been reported by Shamanian et al. (2004) at Gandy and Abolhassani in the eastern Alborz of northern Iran, hosted by late Eocene calc-alkaline volcanic and volcaniclastic rocks, but little is known about the geodynamic setting of these deposits.

Geologic Setting of Sari Gunay

The Sari Gunay gold deposit is hosted by a middle Miocene volcanic complex that forms a range of small hills in an area ~10 km across, flanked to the east and southeast by shallowly sloping lahar and block-and-ash-flow deposits (Fig. 4). Volcanic structures appear to have been rapidly degraded by coeval lahar formation, such that the core of the system is locally eroded down to its hypabyssal intrusive roots, with vertically flow-banded necks forming prominent remnant spires. Hydrothermal alteration (especially silicification) has also resulted in erosional resistance of the Sari Gunay and adjacent Agh Dagh hills (Fig. 5).

The complex lies unconformably on Jurassic schists and limestones on its eastern side and Eocene to Oligocene intermediate to felsic volcanic rocks and limestone to the southeast. These contacts are rarely well exposed, and some may be structural, but several drill holes through volcanic and subvolcanic intrusive rocks at Sari Gunay have penetrated paleoweathering horizons overlying basement schist, and schist clasts are found in some of the fragmental volcanic facies. Rafts of schist and limestone also occur locally within the volcanic complex (e.g., near Sari Gunay at 0235400E, 3899500N: UTM grid, WGS84 projection).

The margins of the complex to the north, south, and west slope gently below Quaternary alluvial deposits, such that precise outcrop limits are hard to constrain.

To the northwest, a small Quaternary volcanic complex near the village of Qezeljeh Kand projects through the alluvial cover and includes basanitic cinder cones (locally worked for pumice abrasives) and trachytic lavas.

Structural setting

Although mappable faults are rarely observed in the field area due to Quaternary alluvial cover, a regional block faulting structure is suggested by outcrop distributions and geomorphological features (Fig. 4), evident both in topographic maps and Landsat images. Most prominent is a major north-northwest–south-southeast–trending structural corridor, which appears to enclose the Miocene Sari Gunay volcanic complex and also to control the location of other Pliocene-Quaternary volcanic centers to the north-northwest, perhaps extending as far as the Zarshuran gold deposit (Figs. 1, 4). This structural and magmatic lineament is referred to as the Takab trend. Its regional extent and linear form suggest a strike-slip origin, with a general orientation similar to other regional-scale thrust and strike-slip faults that accommodate orogenic transpressional deformation in central Iran. In the Sari Gunay area, the corridor appears to have been sectioned by a series of small, late, northeast-southwest–trending block faults, with small inferred vertical displacements (little consistent strike-slip movement is in evidence). Two such faults have been mapped, one to the west of Sari Gunay and the other between Sari Gunay and Agh Dagh (covered, but intersected in drill core, and followed by a major stibnite vein), which may explain an apparent difference in erosional level in these two systems (see below).

It is tempting to speculate on the control that such a strike-slip corridor may have had on magma emplacement and ore formation (e.g., Tosdal and Richards, 2001), but the structural history and framework of this region is not well enough established to warrant further comment.

Geology and Petrology of the Sari Gunay Volcanic Complex

The Sari Gunay volcanic complex consists of a partially eroded composite volcano and its coeval volcaniclastic flank deposits, which include shallowly outward-dipping block-and-ash flows and lahars (Fig. 6A, C). In the effusive part of

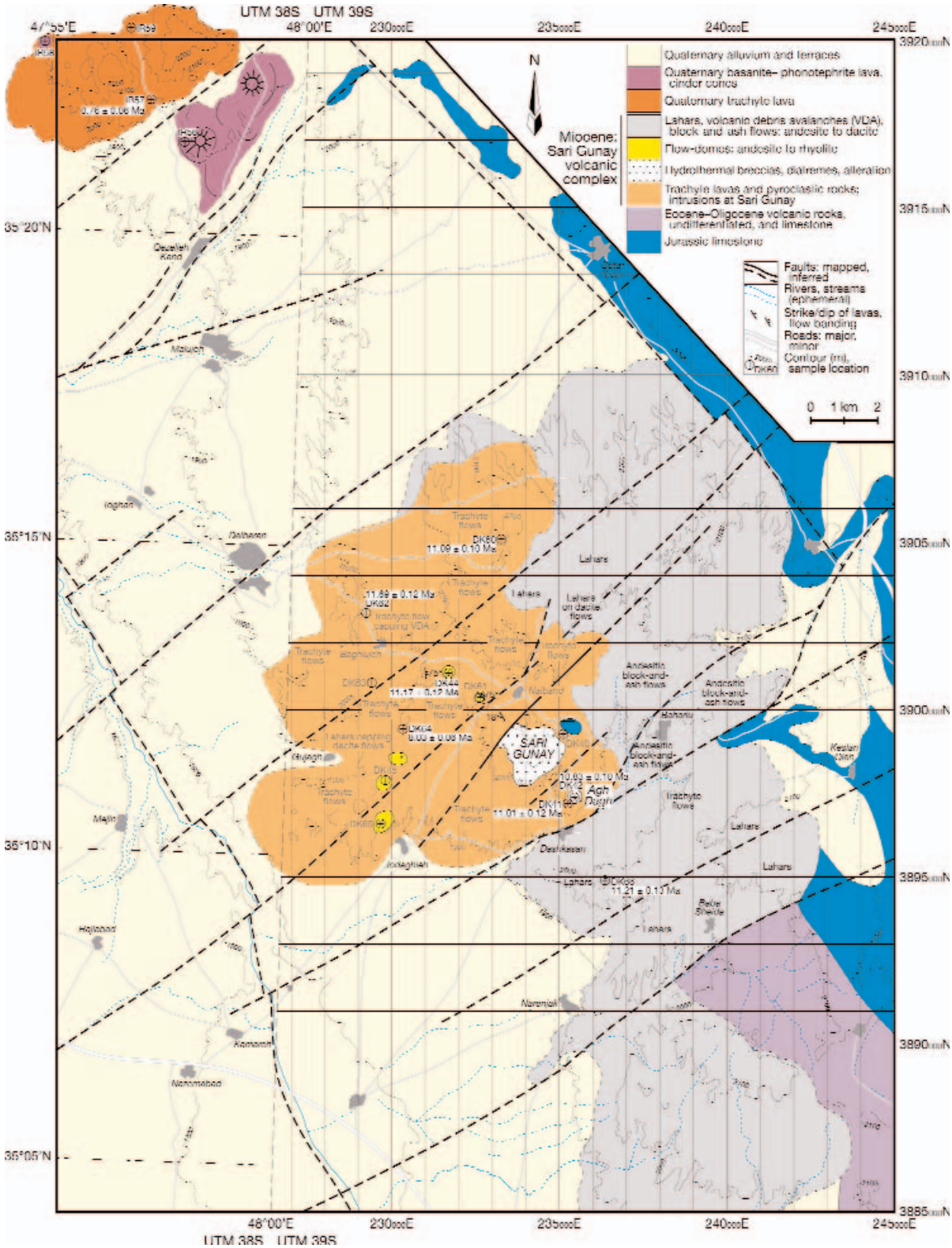

FIG. 4. Geologic map of the Sari Gunay area compiled from mapping by M. Namin (Zar Kuh Mining Company) and the first author, combined with information from the Sanandaj and Kabudar Ahang 1:250,000 geologic maps (available from the Geological Survey of Iran; quadrangles C5 and D5, respectively) and Landsat images. Because of extensive alluvial cover and weathering, structural interpretations are largely based on recognition of topographic and Landsat lineaments, except in the immediate vicinity of Sari Gunay where drilling and trenching have provided fault exposures. Topographical information is from available 1:25,000 and 1:50,000 sheets. Note that the region straddles the boundary between UTM zones 38S and 39S; maps in the western zone 38S were available only in latitude-longitude grid.

FIG. 5. Composite photograph of the Sari Gunay (center) and Agh Dagh (left) hills, looking south; strong hydrothermal silicification has rendered these hills resistant to erosion. Lavas exposed in the small hill on the right (west) dip away from Sari Gunay, and suggest the preerosional profile of the central volcano; however, a fault runs through the valley between these hills, so vertical correlation across the fault may be invalid. Peaks in the distance are formed by Mesozoic granitic and metamorphic rocks of the Sanandaj-Sirjan zone.

FIG. 6. Photographs of volcanic and volcaniclastic deposits in the Sari Gunay volcanic complex. (A). Shallowly westward-dipping lahar deposits above Gujagh village (near 0228000E, 3899000N). (B). Juvenile andesitic volcanic fragment (with lobate borders) in volcanic debris avalanche deposit, near Baghlujeh (0229250E, 3902881N). (C). Andesitic block-and-ash flow, near Baharlu (0238331E, 3900132N). (D). Steeply to vertically flow-banded latite lava dome or volcanic neck, near Jodaghieh (sample DK65; 0229681E, 3896588N; hill is approx 50 m high).

the system, intermediate composition lava flows slope more steeply away from the prominent central peaks of Sari Gunay and Agh Dagh (Fig. 5), and the flows are locally intercalated with volcanic debris avalanche deposits containing juvenile volcanic fragments (as indicated by lobate and breadcrust surface textures of some clasts; Fig. 6B). Small peaks formed by erosionally resistant domes or volcanic necks, ranging in composition from dacite to rhyolite, project through the shallowly dipping lavas and display strong near-vertical flow banding (Fig. 6D). In one case (sample DK45), welded fragmental textures are preserved in the dome material and a small ignimbrite deposit occurs nearby, suggesting an origin as a pyroclastic flow-dome complex.

Volcanic rocks range in texture from porphyritic to vitrophyric, with devitrification of glassy matrices in most instances and variable oxidation of mafic phenocryst phases. In the following descriptions, the total alkali versus silica classification scheme of Le Maitre (1989) is used for rock nomenclature, based on geochemical data presented below (recalculated free of volatiles).

Latite porphyry lavas (Fig. 7A) contain abundant phenocrysts of zoned plagioclase (commonly in glomeroporphyritic clusters) and hornblende (variably oxidized), with lesser amounts of biotite (also variably oxidized), clinopyroxene, and orthopyroxene. The matrix is fine grained or glassy (brown where fresh, but commonly devitrified), containing abundant feldspar crystallites and variably oxidized microphenocrysts of magnetite; minor amounts of carbonate occur as alteration products in the matrix. The freshest sample of latite lava (sample DK66; Fig. 7A) forms a capping flow on a thick sequence of lahars to the southeast of Dashkasan village.

Porphyritic trachyte lavas (Fig. 7B) are the most abundant volcanic rock type in the complex, forming low featureless hills in the western half of the area. Biotite is more abundant than in latites, although hornblende is still commonly the dominant ferromagnesian silicate mineral; both are variably oxidized. Plagioclase phenocrysts are abundant and commonly zoned and intergrown, yielding a glomeroporphyritic texture; clinopyroxene forms sparse clusters of small crystals. Rare rounded quartz and large sanidine phenocrysts occur in more felsic and potassic compositions, respectively. The matrix is very fine grained to glassy (clear where fresh, but commonly devitrified), with abundant feldspar crystallites.

Rhyolite (Fig. 7C) is not abundant but occurs as flow-banded domes or pyroclastic deposits, forming prominent hills. $^{40}Ar/^{39}Ar$ age determinations (presented below) show that some of these rhyolites are significantly younger than the intermediate suite of volcanic rocks (see below). Quartz phenocrysts are abundant and are variably euhedral to rounded and embayed. Sanidine phenocrysts are also abundant, with minor plagioclase and biotite; hornblende, where present, is oxidized. The matrix consists of variably devitrified glass, which commonly accentuates flow-banding textures.

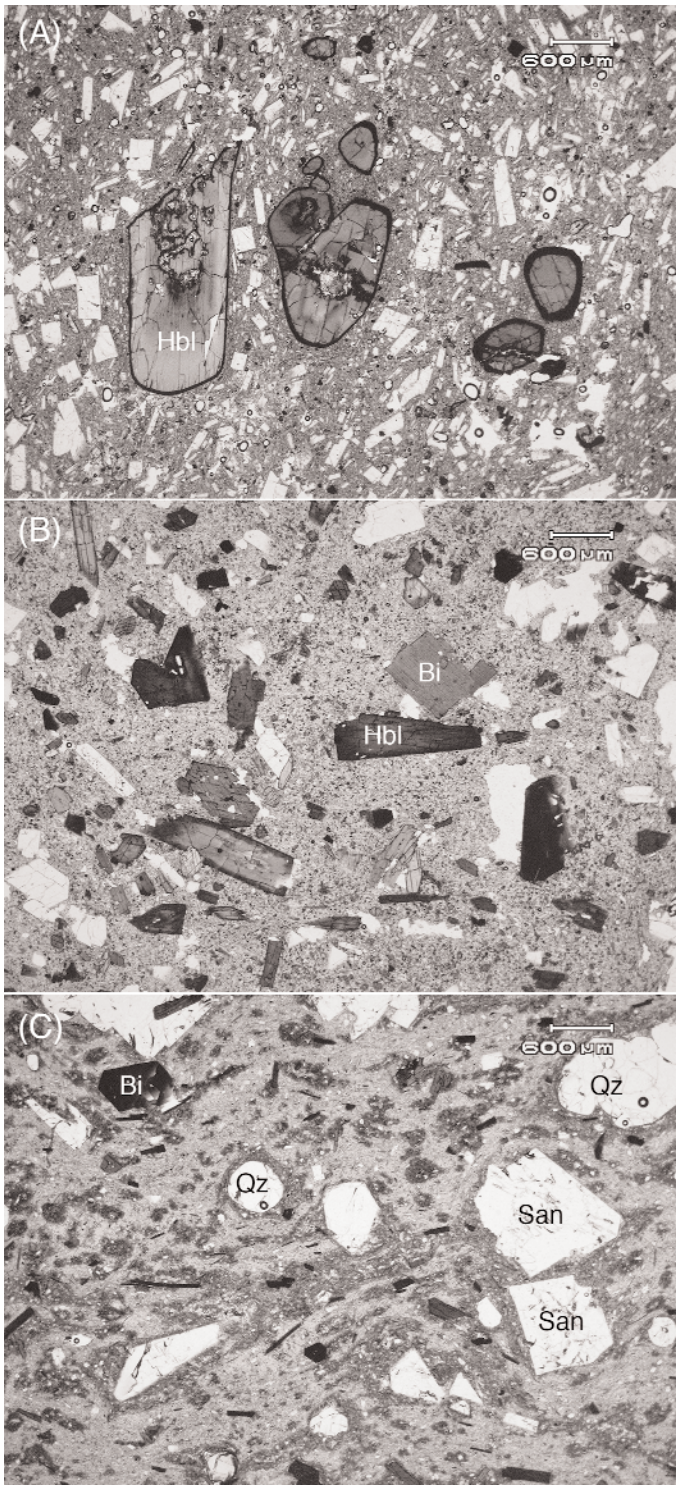

FIG. 7. Photomicrographs of volcanic rocks from the Sari Gunay volcanic complex. (A). Latite lava flow, with prominent brown hornblende (with thin oxidation rims) and smaller plagioclase phenocrysts, set in a slightly vesicular, brown glassy matrix containing abundant plagioclase crystallites (sample DK66). (B). Trachyte lava flow, with hornblende, biotite, and plagioclase phenocrysts, set in clear glassy matrix with plagioclase crystallites (sample DK60). (C). Rhyolite flow dome, with rounded quartz, euhedral sanidine, and minor biotite phenocrysts, set in a partially devitrified, flow-banded glassy matrix (sample DK64).

Igneous Geochemistry of the Sari Gunay Volcanic Complex

Samples

Twenty-six samples of fresh and altered igneous rocks from the Sari Gunay volcanic complex and 44 samples from other

volcanic and intrusive centers in central and northwestern Iran were collected for whole-rock geochemical analysis. Sample locations and brief descriptions are given in Table 1. Full geochemical data for 22 least altered samples from the Sari Gunay volcanic complex are listed in Table 2, which includes details of the analytical methods used. The data for other samples shown for comparison on various geochemical plots are listed in Table A1. Four different laboratories were used at various times over the four-year period of this project, and analyses of standards and duplicate samples at these various laboratories indicate accuracy for major elements to within 5 relative percent (<3% for SiO_2 and Al_2O_3) and for minor and trace elements to within 10 relative percent. With one exception (sample IR60) we report data from Actlabs Laboratories, Ontario, Canada, in Table 2, which appeared to produce the most reproducible and accurate results.

Major element compositions

The compositions of igneous rocks from the Sari Gunay volcanic complex are plotted on the total alkali-silica diagram of Le Maitre (1989) in Figure 8. All samples are high K, and the majority of least altered samples from Sari Gunay plot within the trachyte and dacite fields, but four samples plot within the latite field (including two samples of alkalic hornblende-phyric latite, which are essentially duplicates from the same drill hole), and three plot at distinctly higher silica contents in the rhyolite field. Altered trachytic and/or dacitic rocks, characterized by varying degrees of sericitization and silicification, show more variable alkali contents and generally higher silica contents than unaltered rocks.

Harker diagrams showing variations of major and minor oxides with silica for least altered igneous rocks from Sari Gunay (Fig. 9) reveal normal fractionation trends, consistent with these samples being broadly comagmatic. Most oxides decrease with increasing silica except for K_2O, which shows slight enrichment. The two most mafic latite samples are broadly collinear with these fractionation trends but are distinguished by slightly higher alkali contents, suggesting a possibly distinct parentage.

The compositions of other igneous rocks from northwestern and central Iran are included in Figure 8 for comparison with the Sari Gunay suite. Two of the five samples from the Quaternary volcanic complex near Qezeljeh Kand in the extreme northwest corner of the map area (Fig. 4) plot as medium K dacite and trachyte, similar to the Sari Gunay rocks, but three other samples from mafic cinder cones plot as high K basanite and phonotephrite. Similar alkaline rocks occur in scattered Quaternary volcanic centers throughout northwestern and central Iran, including the Shebe Jazireh Shahi basanitic volcano, which forms an island in Lake Urumieh, and more felsic alkaline rocks (high K shoshonites, latites, and trachytes) from the Badamlu, Sar Cheshmeh, and Meiduk areas (Figs. 1, 8). These alkaline volcanic rocks are likely the products of postcollisional magmatism and are found throughout the Neo-Tethyan orogen from Iran to Turkey (e.g., Yilmaz et al., 1998; Aldanmaz, 2002).

Miocene volcanic rocks from the Dehgolan area, approximately 70 km northwest of Sari Gunay, have high K latite-trachyte-rhyolite compositions similar to the Sari Gunay complex, but Neogene volcanic rocks farther northwest in the Zarshuran area (Fig. 1) are predominantly medium to high K andesites (Fig. 8). This northwest-southeast–trending volcanic array (Takab-Dehgolan-Sari Gunay) constitutes the Takab belt and is distinguished both spatially and compositionally from the predominantly medium K, calc-alkaline, andesitic-dacitic volcanic rocks of the Kerman belt (Fig. 8).

The Kerman belt is the southeastern part of the extensive mid-Tertiary Urumieh-Dokhtar volcanic arc and hosts important middle Miocene porphyry copper deposits at Sar Cheshmeh and Meiduk (Fig. 1), as well as smaller showings at Abdar and Iju (samples of associated volcanic rocks are plotted in Fig. 8). The Urumieh-Dokhtar belt becomes diffuse (faulted and covered) to the northwest but may include medium K dioritic intrusive rocks to the west and northwest of Razan (north and east of Sari Gunay; Figs. 1, 8) where porphyry-style alteration has been noted.

The large Miocene to Quaternary Sahand volcano in northwest Iran (Fig. 1) consists of lavas and pyroclastic rocks of medium K basaltic andesite to rhyolite composition (Fig. 8), which are somewhat less alkaline than either the Takab or Kerman belt rocks.

Trace element compositions

Trace element compositions are tightly grouped for all Sari Gunay samples except rhyolites, and the alkalic latites are not distinguishable from other intermediate composition rocks beyond expected fractionation effects (Figs. 10, 11). In a mantle-normalized diagram (Fig. 10), latites show relatively smaller enrichments in large ion lithophile elements (LILE) but marginally higher concentrations of middle and heavy rare earth elements (MREE, HREE) compared with more evolved samples. Positive anomalies for Pb and Sb are common for arc-related igneous rocks, but the Sari Gunay suite displays unusually high concentrations of these elements, especially Sb, which extends up to 32,600 × primitive mantle values in felsic rocks. Antimony (as stibnite) is a major component of mineralized veins in the hydrothermal system. Listric-shaped REE patterns (Figs. 10, 11) are consistent with fractionation of normal phenocryst assemblages including clinopyroxene and amphibole during crustal ascent and emplacement (hornblende in particular preferentially partitions MREE, leading to listric-shaped patterns in fractionated rocks: e.g., Frey et al., 1978; Hanson, 1980; Lang and Titley, 1998). Elevated magmatic water contents (as evidenced by amphibole phenocrysts) and oxidation state (as suggested by abundant magnetite in intermediate rocks) likely explain the lack of europium anomalies (Fig. 11), respectively by suppression of feldspar crystallization until late stages of differentiation and the presence of europium in the Eu^{3+} oxidation state, as opposed to Eu^{2+} which can partition into feldspar (Hanson, 1980).

Rhyolites from the Sari Gunay volcanic complex display distinctive trace element patterns, characterized by relative enrichments in LILE but lower concentrations of high field strength elements (HFSE) and REE compared with intermediate rocks (Figs. 10, 11). Phosphorus and titanium are also strongly depleted in rhyolites, likely due to extensive fractionation of apatite and Ti-bearing phases (magnetite, hornblende, biotite). Rhyolite REE patterns show significantly lower concentrations of light REE (LREE) and MREE but

TABLE 1. Whole-Rock Sample Locations and Descriptions

Sample no.[1]	UTM Easting (WGS84)	UTM Northing (WGS84)	General location	Drill hole: depth	Elevation, azimuth/dip	Sample description	Lithology (total alkali-silica terminology; see Fig. 8)	Ar-Ar plateau age (Ma ± 2σ)[2]
DK3	39S 0234258	3898912	Sari Gunay	DDH11: 92.4–92.7m	2167m, 130/-70°	Biotite andesite porphyry	Dacite (hi K)	11.03 ± 0.16
DK5	39S 0234258	3898912	Sari Gunay	DDH11: 119.3–119.6m	2167m, 130/-70°	Hornblende andesite porphyry	Latite (hi K)	
DK6	39S 0234258	3898912	Sari Gunay	DDH11: 120.1–120.4m	2167m, 130/-70°	Hornblende andesite porphyry	Latite (hi K)	
DK16+17	39S 0235334	3897653	Agh Dagh	DDH10: 247.0–247.3m	2065m, 130/-50°	Phyllic altn in K-feldspar porphyry	Altered	
DK18	39S 0234869	3899325	Sari Gunay	DDH25: 99.2–99.5m	2056m, 130/-50°	Biotite andesite porphyry	Trachyte (hi K)	
DK19	39S 0234869	3899325	Sari Gunay	DDH25: 101.2–101.6m	2056m, 130/-50°	Biotite andesite porphyry	Trachyte (hi K)	
DK20	39S 0234869	3899325	Sari Gunay	DDH25: 175.7–177.2m	2056m, 130/-50°	Plagioclase-biotite porphyry	Dacite (hi K)	11.16 ± 0.16
DK21	39S 0234390	3898914	Sari Gunay	DDH4: 128.2–129.5m	2203m, 130/-51°	Sericitic alteration	Altered	
DK22	39S 0234489	3898812	Sari Gunay	DDH9: 383.4–383.7m	2198m, 130/-45°	Sericitic alteration	Altered	
DK23	39S 0234489	3898812	Sari Gunay	DDH9: 393.1–393.4m	2198m, 130/-45°	Sericitic alteration	Altered	
DK26	39S 0234489	3898812	Sari Gunay	DDH9: 415.3–415.5m	2198m, 130/-45°	Sericitic alteration	Altered	10.69 ± 0.10
DK27	39S 0234489	3898812	Sari Gunay	DDH9: 424.2–424.5m	2198m, 130/-45°	Sericitic alteration	Altered	
DK28	39S 0234519	3898931	Sari Gunay	DDH19: 95.6–95.8m	2192m, 130/-60°	Sericitic alteration	Altered	10.27 ± 0.10
DK39	39S 0234643	3898941	Sari Gunay	DDH20B: 318.2–318.9m	2132m, 130/-55°	Sericitic alteration	Altered	
DK40	39S 0235139	3899263	Sari Gunay			Biotite dacite porphyry	Trachyte (hi K)	
DK41	39S 0235266	3897195	Qare Dagh			K-feldspar-plagioclase-biotite porphyry	Trachyte (hi K)	11.01 ± 0.12
DK42	39S 0235469	3897382	Agh Dagh			Phyllic altn in K-feldspar porphyry	Altered	10.83 ± 0.10
DK44	39S 0231696	3901092	Sari Gunay regional			Rhyolitic volcanics	Rhyolite (hi K)	11.17 ± 0.12[3]
DK45	39S 0229827	3897885	Sari Gunay regional			Dacitic ignimbrite	Dacite (hi K)	
DK60	39S 0233286	3905084	Sari Gunay regional			Intermediate lava below mafic flow cap to hill	Trachyte (hi K)	11.09 ± 0.10
DK61	39S 0232648	3900364	Sari Gunay regional			Rhyolitic lava dome; flow banding 135/75°E	Rhyolite (hi K)	
DK62	39S 0229250	3902881	Sari Gunay regional			Intermediate lavas overlying lahar	Trachyte (hi K)	11.69 ± 0.12
DK63	39S 0229407	3900799	Sari Gunay regional			Intermediate flows/pyroclastics	Trachyte (hi K)	
DK64	39S 0230342	3899408	Sari Gunay regional			Rhyolitic flows/pyroclastics	Rhyolite (med K)	8.03 ± 0.06
DK65	39S 0229681	3896588	Sari Gunay regional			Lava dome	Latite (hi K)	
DK66	39S 0236374	3894901	Sari Gunay regional			Remnant lava flow capping hill	Latite (med K)	11.21 ± 0.13
IR1	38S 0653765	4169009	Sahand area			Quaternary monogenetic vent lava flow	Rhyolite (med K)	0.51 ± 0.01
IR2	38S 0640231	4168404	Sahand area			Basaltic andesite lava	Basaltic andesite (med K)	
IR4	40R 0375909	3315144	Sar Cheshmeh			Kuh-e-Ghool dacite dome	Dacite (med K)	
IR5	40R 0384295	3311562	Sar Cheshmeh			Sar Kuh andesitic dike	Andesite (med K)	
IR6	40R 0384191	3311196	Sar Cheshmeh			Sar Kuh granodiorite	Dacite (granodiorite; hi K)	
IR7	40R 0384494	3314916	Sar Cheshmeh			Purple (altered) lava	Dacite (med K)	
IR8	40R 0387079	3316587	Sar Cheshmeh			Trachybasaltic lava	Potassic trachybasalt (hi K)	
IR10	40R 0388666	3320641	Sar Cheshmeh			Vesicular trachytic lava	Trachyte (hi K)	
IR11	40R 0385736	3321796	Sar Cheshmeh			Oxidized felsic lava	Rhyolite (hi K)	
IR14	40R 0339064	3355367	Abdar			Dioritic intrusion	Benmoreite (med K)	
IR15	40R 0323784	3366841	Meiduk			Meiduk deposit, late dike	Shoshonite (hi K)	
IR16	40R 0320827	3364163	Meiduk			Meiduk area lava flow	Latite (hi K)	
IR17	40R 0320392	3362717	Meiduk			Meiduk area hornblende-phyric dike	Andesite (med K)	
IR18	40R 0320105	3362543	Meiduk			Meiduk area hornblende-phyric dike	Dacite (med K)	
IR19	40R 0320005	3362092	Meiduk			Meiduk area volcanic rock	Andesite (med K)	
IR20	40R 0303328	3380276	Iju			Iju area dike	Dacite (med K)	
IR21	40R 0303537	3379730	Iju			Iju area lava flow	Benmoreite (med K)	
IR50	38S 0722024	3935593	Dehgolan			Miocene volcanic rock	Trachyte (hi K)	9.77 ± 0.29
IR51	38S 0721888	3931891	Dehgolan			Miocene volcanic rock	Rhyolite (hi K)	
IR52	38S 0719458	3927705	Dehgolan			Miocene hornblende-biotite-plagioclase dacite porphyry	Dacite (hi K)	9.60 ± 0.21

TABLE 1. *(Cont.)*

Sample no.[1]	UTM Easting (WGS84)	UTM Northing (WGS84)	General location	Drill hole: depth	Elevation, azimuth/dip	Sample description	Lithology (total alkali-silica terminology; see Fig. 8)	Ar-Ar plateau age (Ma ± 2σ)[2]
IR53	38S 0722998	3925059	Dehgolan			Miocene lava	Latite (hi K)	
IR54	38S 0729817	3927172	Dehgolan			Miocene ignimbrite	Rhyolite (hi K)	
IR55	38S 0727040	3925280	Dehgolan			Young (Quaternary?) unwelded ignimbrite	Trachyte (hi K)	
IR56	38S 0769060	3916819	Qezeljeh Kand			Quaternary cinder cone, Kuh Siah quarry	Phonotephrite (hi K)	
IR57	38S 0767972	3917996	Qezeljeh Kand			Quaternary hornblende-phyric lava 6	Dacite (med K)	0.76 ± 0.0
IR58	38S 0764760	3919485	Qezeljeh Kand			Quaternary mafic lava flow	Basanite (hi K)	
IR59	38S 0767246	3920050	Qezeljeh Kand			Quaternary hornblende-plagioclase-phyric lava	Trachyte (med K)	
IR60	38S 0764957	3923278	Qezeljeh Kand			Quaternary cinder cone	Basanite (hi K)	
IR61	39S 0316648	3917328	W Razan			Miocene hornblende porphyritic gabbro	Basalt (gabbro; med K)	
IR62	39S 0309755	3916892	W Razan			Miocene, weakly propylitically altered hornblende porphyritic diorite	Basaltic andesite (diorite; med K)	
IR63	39S 0310000	3916595	W Razan			Miocene, fresher, locally megacrystic hornblende diorite porphyry	Shoshonite (diorite; hi K)	6.1 ± 1.6
IR64	39S 0292569	3938804	W Razan			Miocene weakly propylitically altered hornblende diorite	Dacite (diorite; med K)	8.6 ± 1.4
IR65	38S 0688918	4064893	Zarshuran area			Miocene, weakly propylitically altered (chloritized, purple) andesite	Andesite (hi K)	
IR66	38S 0690209	4070004	Zarshuran area			Miocene, weakly propylitically altered (chloritized, purple) lava	Latite (hi K)	
IR67	38S 0689710	4069812	Zarshuran area			Pliocene(?) moderately chloritized microdiorite intrusion	Andesite (microdiorite; med K)	
IR68	38S 0685040	4072401	Zarshuran area			Miocene, relatively fresh lava	Andesite (hi K)	
IR69	38S 0631648	4100001	Badamlu			Eocene, large float boulder of fresh biotite-plagioclase trachyte	Trachyte (hi K)	
IR70	38S 0638112	4100817	Badamlu			Moderately propylitically altered fragmental volcanic rock	Shoshonite (hi K)	
IR71	38S 0646647	4101380	Badamlu			Mild propylitic alteration in biotitic granite	Trachyte (granite; hi K)	
IR72	38S 0646550	4100495	Badamlu			Fresh coarse-grained biotitic granite	Trachyte (granite; hi K)	39.85 ± 0.25
IR73	38S 0551292	4189228	Shebe Jazireh Shahi			Plio-Pleistocene hornblende-rich mafic lava	Basanite (hi K)	
IR74	38S 0551291	4186693	Shebe Jazireh Shahi			Plio-Pleistocene hornblende-porphyritic mafic dike	Basanite (hi K)	
IR75	38S 0613744	4180295	Sahand volcano			Crystal-rich layer within Miocene ignimbrite	Dacite (med K)	7.02 ± 0.20
IR76	38S 0616541	4178311	Sahand volcano			Ignimbrite	Dacite (med K)	

Notes: hi K = high K, med K = medium K

[1] Samples with prefix DK from Sari Gunay area; samples with prefix IR from elsewhere in northwestern and central Iran

[2] Age data for DK samples and IR57 are summarized in Table 3 and presented in full in Table A2; data for other IR samples are available from the first author by request

[3] Inverse isochron age.

TABLE 2. Major and Trace Element Analyses of Least Altered Igneous

Sample no.		DK3	DK5	DK6	DK18	DK19	DK20	DK40	DK41	DK44
Lithology (total alkali-silica)	Analytical method[1]	Dacite (hi K)	Latite (hi K)	Latite (hi K)	Trachyte (hi K)	Trachyte (hi K)	Dacite (hi K)	Trachyte (hi K)	Trachyte (hi K)	Rhyolite (hi K)
Weight %										
SiO_2	Fusion-ICP	64.96	56.89	54.78	62.78	62.87	59.77	63.94	65.72	72.81
Al_2O_3	Fusion-ICP	14.13	16.14	15.96	15.85	15.91	15.62	17.04	16.02	14.10
CaO	Fusion-ICP	1.48	3.11	2.71	2.47	2.14	2.57	3.82	1.78	1.29
MgO	Fusion-ICP	2.68	4.31	4.73	2.12	2.09	2.51	0.84	0.97	0.16
Na_2O	Fusion-ICP	3.25	4.82	4.42	4.10	4.02	3.30	4.18	4.48	3.33
K_2O	Fusion-ICP	3.20	3.32	3.08	3.29	3.33	3.15	3.18	4.14	4.54
$Fe_2O_3^T$	Fusion-ICP	5.19	7.25	8.59	4.95	4.98	6.39	3.36	3.11	0.93
MnO	Fusion-ICP	0.12	0.19	0.25	0.22	0.23	0.25	0.03	0.04	0.01
TiO_2	Fusion-ICP	0.69	0.81	0.88	0.54	0.56	0.59	0.76	0.45	0.13
P_2O_5	Fusion-ICP	0.34	0.39	0.39	0.26	0.27	0.27	0.31	0.33	0.06
LOI	Fusion-ICP	2.75	2.40	3.41	2.39	2.64	4.08	1.55	2.16	1.20
S(%)	Total dissolution ICP	0.01	0.01	0.03	0.01	0.02	0.15	0.02	0.00	0.01
Sum		98.80	99.63	99.22	98.98	99.05	98.65	99.02	99.20	98.57
Ppm										
Cs	Fusion-ICP-MS	12.4	6.5	7.3	8.1	9.1	8.7	5.7	6.9	15.0
Tl	Fusion-ICP-MS	1.31	1.22	1.14	1.06	1.21	0.99	0.92	1.51	1.24
Rb	Fusion-ICP-MS	128	120	112	110	117	103	101	144	166
Ba	Fusion-ICP	1388	1611	1507	1659	1606	1873	2130	1773	1305
Th	Fusion-ICP-MS	21.4	24.3	23.9	27.7	28.7	28.4	27.6	47.9	17.4
U	Fusion-ICP-MS	6.84	7.92	8.53	8.69	8.87	9.36	7.92	13.70	9.00
Nb	Fusion-ICP-MS	17.5	21.3	22.6	19.7	20.2	20.1	20.3	22.9	16.9
Ta	Fusion-ICP-MS	1.3	1.4	1.5	1.5	1.5	1.5	1.5	1.7	1.7
La	Fusion-ICP-MS	66.2	73.1	74.2	67.5	69.8	70.8	71.4	92.8	19.0
Ce	Fusion-ICP-MS	116	130	132	114	116	117	120	160	34
Pb	Total dissolution ICP	49	23	36	81	100	144	28	169	73
Pr	Fusion-ICP-MS	12.0	13.9	14.0	11.5	11.9	11.9	12.3	16.8	3.6
Sr	Fusion-ICP	651	907	776	916	848	848	1001	935	613
Nd	Fusion-ICP-MS	40.8	48.4	49.4	37.1	38.6	39.3	40.0	55.0	12.2
Zr	Fusion-ICP-MS	155	207	197	187	172	185	194	261	103
Hf	Fusion-ICP-MS	3.9	4.9	4.8	4.5	4.3	4.3	4.7	6.5	3.1
Sm	Fusion-ICP-MS	6.8	8.4	8.8	6.1	6.4	6.5	6.8	8.9	2.6
Eu	Fusion-ICP-MS	1.76	2.18	2.32	1.58	1.60	1.70	1.81	2.10	0.74
Gd	Fusion-ICP-MS	4.9	6.4	7.0	4.5	4.8	5.0	5.1	6.2	2.3
Tb	Fusion-ICP-MS	0.67	0.90	0.98	0.65	0.68	0.73	0.72	0.78	0.37
Dy	Fusion-ICP-MS	3.4	4.6	5.0	3.5	3.6	3.8	3.8	3.8	2.1
Y	Fusion-ICP	17	24	29	20	21	23	20	19	14
Ho	Fusion-ICP-MS	0.59	0.83	0.92	0.65	0.66	0.73	0.69	0.65	0.42
Er	Fusion-ICP-MS	1.65	2.32	2.57	1.90	1.95	2.11	1.93	1.83	1.25
Tm	Fusion-ICP-MS	0.23	0.33	0.37	0.29	0.30	0.31	0.28	0.27	0.21
Yb	Fusion-ICP-MS	1.53	2.11	2.37	1.90	1.98	2.06	1.76	1.76	1.44
Lu	Fusion-ICP-MS	0.22	0.30	0.34	0.29	0.29	0.30	0.25	0.26	0.22
Be	Fusion-ICP-MS	2	3	4	3	3	3	3	3	3
Sc	Neutron activation	13.7	16.0	17.7	8.0	8.5	11.1	11.2	5.7	1.8
V	Fusion-ICP	110.0	131.0	137.0	74.0	82.0	97.0	90.0	65.0	13.0
Bi	Fusion-ICP-MS	2.9	4.4	22.5	1.8	1.5	3.9	2.7	2.9	1.5
Cr	Neutron activation	73	86	93	42	48	101	89	24	3
Co	Neutron activation	14	20	22	11	13	12	10	6	2
Ni	Total dissolution ICP	30	44	51	24	27	34	21	22	2
Cu	Total dissolution ICP	30	23	134	12	11	16	14	21	2
Zn	Neutron activation/ total dissolution ICP	231	132	129	192	206	145	97	267	21
As	Neutron activation	25	35	39	20	24	54	24	41	36
Sb	Neutron activation	37.8	21.7	27.2	6.9	5.9	11.8	1.6	27.2	2.1
Ga	Fusion-ICP-MS	17	20	20	19	19	19	20	20	18
Ge	Fusion-ICP-MS	1.3	1.4	1.5	1.3	1.3	1.0	1.2	1.5	1.5

Notes: hi K = high K, med K = medium K, n/a = not analyzed; all samples analyzed at Actlabs (Activation Laboratories, Ancaster, Ontario, Canada) except

[1] All samples were crushed and milled in a mild-steel swing mill, and analyzed using Actlabs' 4E-Research analytical package (combination of ICP, INAA,

[2] Sample IR60 was analyzed by XRF for major elements, and ICP-MS and ICP-AES for trace elements

Rocks from the Sari Gunay and Qezeljeh Kand Volcanic Complexes

DK45	DK60	DK61	DK62	DK63	DK64	DK65	DK66	IR56	IR57	IR58	IR59	IR60[2]
Dacite (hi K)	Trachyte (hi K)	Rhyolite (hi K)	Trachyte (hi K)	Trachyte (hi K)	Rhyolite (med K)	Latite (hi K)	Latite (med K)	Phonotephrite (hi K)	Dacite (med K)	Basanite (hi K)	Trachyte (med K)	Basanite (hi K)
61.98	61.30	72.91	61.61	65.12	71.30	60.01	59.57	47.67	67.29	44.83	65.40	45.41
16.51	15.86	13.92	17.54	16.88	15.29	16.51	16.51	12.78	15.58	14.18	15.94	13.99
4.88	5.01	0.30	4.50	3.16	2.19	5.17	5.67	11.07	3.07	9.40	3.35	10.03
2.07	2.17	0.16	1.08	0.71	0.56	2.16	2.32	7.90	0.97	9.84	1.00	9.06
3.95	4.23	0.95	4.79	4.33	4.56	4.18	4.20	4.75	4.84	3.88	5.30	4.76
2.73	3.11	8.44	2.62	3.43	2.97	2.85	2.37	3.39	2.94	2.31	3.04	2.91
4.87	4.21	0.78	4.92	3.27	1.58	5.24	4.66	8.04	2.39	10.60	2.47	9.88
0.09	0.09	0.02	0.09	0.02	0.02	0.11	0.09	0.11	0.04	0.14	0.05	0.14
0.58	0.49	0.08	0.65	0.48	0.25	0.57	0.56	1.68	0.43	2.33	0.43	1.98
0.33	0.25	0.03	0.34	0.27	0.09	0.30	0.33	1.80	0.22	0.95	0.24	1.24
2.48	2.65	1.77	1.75	2.30	1.09	2.72	3.21	0.35	2.17	1.36	1.93	0.74
0.00	0.16	0.06	0.06	0.05	0.01	0.14	0.33	0.08	0.00	0.00	0.01	n/a
100.47	99.53	99.42	99.95	100.02	99.92	99.96	99.81	99.62	99.95	99.82	99.15	100.14
3.3	5.8	14.6	2.0	5.3	7.6	5.4	3.5	1.8	1.9	0.9	2.2	1.4
0.29	0.57	5.35	0.61	0.61	0.70	0.24	0.30	0.26	0.46	0.11	0.55	0.12
86	96	322	77	105	99	82	67	61	68	65	68	49
1740	1666	1389	1483	1823	793	1695	1144	1748	1070	794	1425	1132
33.1	33.3	20.3	27.4	32.5	12.2	32.5	22.0	25.4	18.8	9.5	25.4	13.3
9.49	9.17	7.81	8.02	8.52	5.17	8.48	6.91	4.75	4.70	2.24	6.20	2.84
17.5	20.3	14.7	23.3	21.2	7.4	16.4	20.8	45.9	17.5	45.4	27.8	49.5
1.3	1.7	1.5	1.7	1.7	0.7	1.3	1.5	2.6	1.1	3	1.7	2.4
84.5	74.2	11.5	75.7	70.4	22.0	79.7	60.2	154	54.2	69.3	62.8	>100
143	129	22	131	125	40	144	105	285	86.6	128	103	>200
29	42	104	35	47	29	40	31	18	18	7	25	14
14.7	12.8	2.4	13.4	12.8	4.2	14.6	10.6	33.3	8.3	14.3	10.1	24.0
1164	1086	196	1064	1119	478	1167	995	2334	697	1177	961	>1200
48.5	42.9	9.1	44.2	43.3	14.3	48.5	35.0	119.0	25.7	51.9	32.3	87.4
198	191	96	211	204	143	177	193	322	200	244	202	247
4.8	5.0	3.4	5.2	5.5	3.8	4.7	4.8	7.0	4.6	5.3	4.8	5.2
7.8	6.7	2.2	6.7	6.7	2.4	7.3	5.4	17.6	3.9	8.8	4.7	12.6
1.93	1.66	0.63	1.87	1.72	0.66	1.93	1.49	4.58	0.98	2.62	1.23	3.26
5.8	5.2	2.0	5.3	4.9	2.0	5.8	4.3	11.4	2.5	7.0	3.2	8.6
0.77	0.71	0.36	0.73	0.64	0.26	0.75	0.59	1.22	0.31	0.91	0.42	1.05
4.0	3.8	2.1	3.8	3.2	1.3	4.0	3.1	5.3	1.6	4.5	2.1	5.0
21	22	14	23	17	8	22	18	24	8	20	13	23
0.72	0.69	0.42	0.72	0.54	0.23	0.72	0.59	0.81	0.28	0.75	0.39	0.85
2.13	2.02	1.30	2.14	1.50	0.64	2.11	1.74	2.04	0.78	1.91	1.16	2.11
0.31	0.31	0.22	0.31	0.22	0.09	0.31	0.26	0.26	0.11	0.26	0.17	0.27
2.01	1.93	1.48	2.00	1.42	0.59	1.99	1.68	1.52	0.72	1.48	1.12	1.66
0.31	0.29	0.22	0.28	0.22	0.08	0.29	0.25	0.20	0.10	0.20	0.17	0.22
3	n/a	n/a	n/a	n/a	n/a	n/a	n/a	n/a	n/a	n/a	n/a	n/a
9.7	7.7	1.4	7.1	6.8	2.5	10.3	6.6	12.1	3.3	17.6	3.0	n/a
91.0	69.0	6.0	70.0	63.0	18.0	94.0	65.0	146.0	31.0	199.0	32.0	n/a
1.1	n/a	n/a	n/a	n/a	n/a	n/a	n/a	2.5	2.3	0.7	3.1	n/a
30	49	< 0.5	26	16	8	42	39	169	12	231	14.3	n/a
10	10	1	11	7	3	13	13	31	7	45	6	n/a
12	58	11	20	13	11	17	30	164	6	186	7	n/a
10	217	57	33	21	16	21	25	46	9	40	11	n/a
52	60	51	70	56	42	71	70	84	52	85	56	n/a
4	16	48	10	10	8	9	13	3	3	2	4	n/a
0.4	1.3	163.0	1.2	1.2	0.7	10.0	1.1	0.8	0.2	0.1	0.2	n/a
20	18	16	20	19	17	18	18	20	18	20	19	n/a
1.1	1.3	2.3	1.4	1.4	1.3	1.3	1.0	1.1	0.8	1.1	0.9	n/a

IR60 at GEOLABS Geoscience Laboratories, Sudbury, Ontario, Canada)
and ICP-MS)

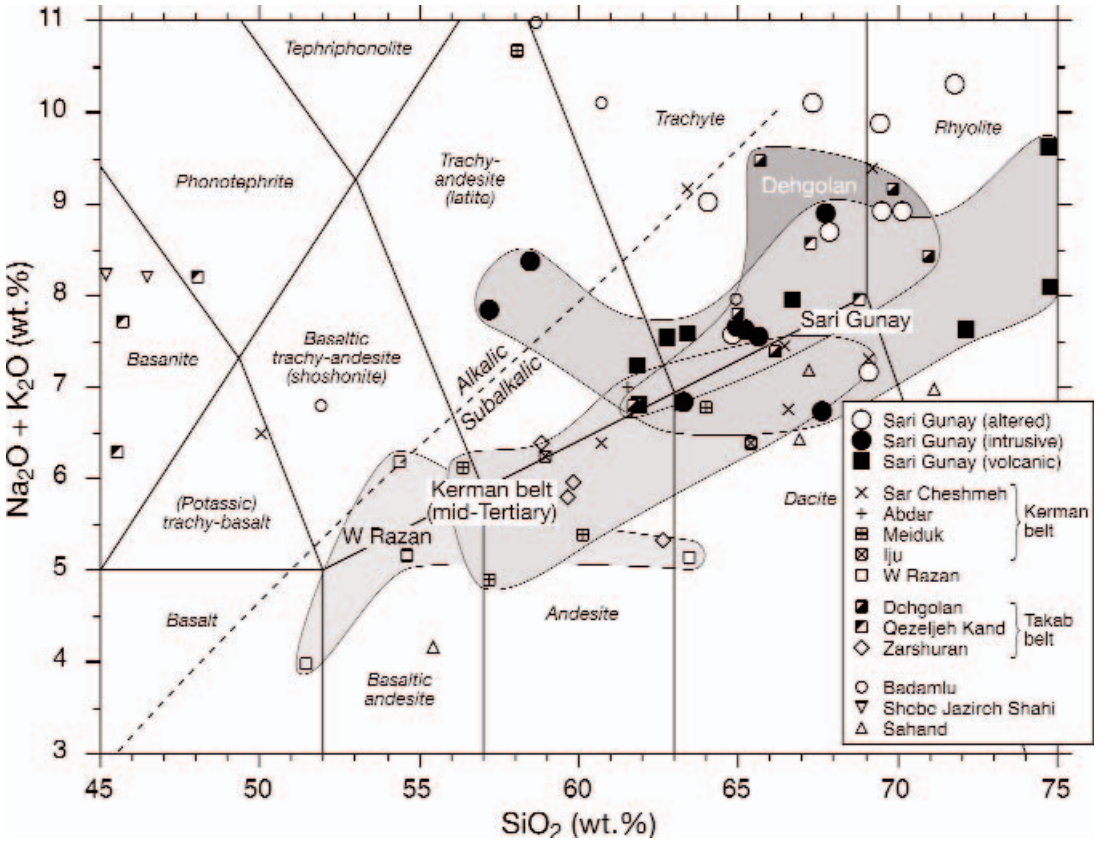

FIG. 8. Total alkali vs. silica diagram (Le Maitre, 1989), showing the compositions of least altered and altered (sericitized and silicified) hypabyssal intrusive rocks from Sari Gunay and Qare Dagh and fresh volcanic rocks from the Sari Gunay volcanic complex (data from Table 2 recalculated to 100% free of volatiles). Also shown are the compositions of Cenozoic volcanic and hypabyssal rocks from other regions of central and northwestern Iran, including the Kerman porphyry belt (Sar Cheshmeh, Abdar, Meiduk, and Iju areas), the Sahand and Shebe Jazireh Shahi volcanoes, and the Dehgolan, west Razan, Badamlu, and Zarshuran volcanic areas; Table A1). These areas include mid-Tertiary intermediate subalkaline and Quaternary mafic-intermediate alkaline volcanic rocks.

converge toward similar levels of HREE for two samples (DK44, DK61) when compared with intermediate rocks (Fig. 11). One sample of rhyolite (DK64) is relatively depleted in HREE, however; as will be shown later, this sample has a younger age than the rest of the suite, so may have a different parentage. In general, however, the rhyolite trace element patterns are consistent with extended fractionation of the intermediate suite. There are no obvious indications of a greater degree of crustal contamination in these felsic rocks, as might be observed in elevated abundances of elements such as Th or U (i.e., they are probably not crustal melts but largely derivative from the intermediate suite).

Trace element compositions of volcanic rocks from the other three localities sampled along the Takab belt (Qezeljeh Kand, Dehgolan, Zarshuran) and also from the Kerman belt are compared with the range of compositions of intermediate rocks from Sari Gunay in Figure 12. A relatively close overlap is observed between Sari Gunay and the Takab belt rocks, especially for the Miocene Dehgolan suite (Fig. 12A). Neogene igneous rocks from the Zarshuran area (Fig. 12B) are somewhat less enriched in LILE and HFSE but have higher HREE compositions compared with Sari Gunay rocks. Trachytic rocks from the Quaternary Qezeljeh Kand volcanic center (Fig. 12C) display very similar patterns to the Sari Gunay rocks, except for lower MREE and HREE. In contrast, the basanitic rocks from this center are quite distinctive in having somewhat lower LILE, higher HFSE and LREE, and overlapping but more steeply sloping MREE-HREE patterns compared with Sari Gunay rocks. Very similar patterns were obtained for samples from the Shebe Jazireh Shahi basanitic volcano in Lake Urumieh (not shown in Fig. 12).

A comparison with samples of subalkaline middle Tertiary rocks from the Kerman belt and western Razan (Fig. 12D) reveals that the Sari Gunay rocks are distinctly more enriched in all trace elements except HREE, which overlap the upper end of the range (characterized by rocks from western Razan). The Takab belt rocks are thus quite distinct from the Urumieh-Dokhtar belt rocks, both in major element (more alkaline) and trace element (incompatible element-enriched) compositions.

$^{40}Ar/^{39}Ar$ Geochronology of the Sari Gunay Volcanic Complex and Hydrothermal Alteration

Samples and methodology

Nine samples of least altered hornblende- and/or biotite-bearing volcanic and hypabyssal rocks were selected from a

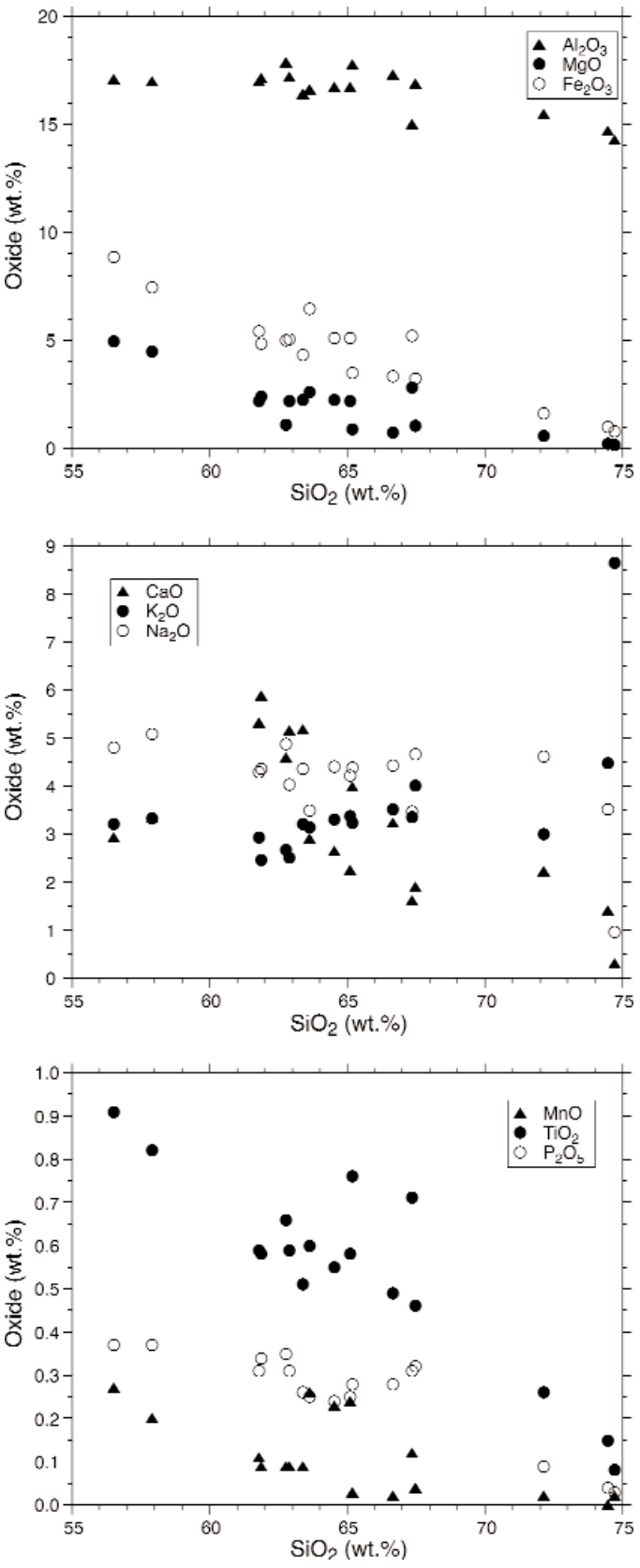

FIG. 9. Harker diagrams, showing variations of major and minor oxides with SiO_2 for least altered igneous rocks from Sari Gunay (data from Table 2 recalculated to 100% free of volatiles).

suite of 22 samples from the Miocene Sari Gunay volcanic complex and the Quaternary Qezeljeh Kand volcanic center for $^{40}Ar/^{39}Ar$ analysis. A further three samples of intensely sericitized intrusive rocks from the Sari Gunay epithermal system were also selected in order to date hydrothermal alteration associated with the mineralizing system.

In addition, seven other samples of volcanic or intrusive rock from elsewhere in northwestern Iran were dated as part of a regional reconnaissance study. The results for these regional samples are summarized in Table 1, and full data are available from the first author by request.

Whole single biotite crystals (0.5–1 mm) and fragments of hornblende phenocrysts (0.25–0.5 mm) were separated from crushed rocks by handpicking after sieving and heavy liquid concentration. Sericite was extracted with a dental pick from altered plagioclase phenocrysts, lightly crushed, and then handpicked to remove impurities. Selected crystals and fragments were wrapped in aluminum foil and stacked in an irradiation capsule with similar-aged samples and neutron flux monitors (Fish Canyon Tuff sanidine: 28.02 ± 0.28 Ma; Renne et al., 1998). The samples were irradiated at the McMaster nuclear reactor in Hamilton, Ontario, for 56 MWh, with a neutron flux of approximately 3×10^{16} neutrons/cm^2. Analyses (n = 54) of 18 neutron flux monitor positions produced errors of <0.5 percent in the J value.

Argon isotope compositions were analyzed in the Noble Gas Laboratory, Pacific Centre for Isotopic and Geochemical Research, University of British Columbia, Canada. The separates were step-heated at incrementally higher powers in the defocused beam of a 10W CO_2 laser (New Wave Research MIR10) until fused. The gas evolved from each step was analyzed by a VG5400 mass spectrometer equipped with an ion-counting electron multiplier. All measurements were corrected for total system blank, mass spectrometer sensitivity, mass discrimination, radioactive decay during and subsequent to irradiation, as well as interfering Ar from atmospheric contamination and the irradiation of Ca, Cl, and K.

$^{40}Ar/^{39}Ar$ results

A summary of geochronological results for the 12 samples from the study area is presented in Table 3, full isotopic data are presented in Table A2, and apparent age spectra are illustrated in Figure 13.

Three different age estimates are reported in Table 3: (1) the integrated age, which is essentially equivalent to a K-Ar date; (2) the plateau age, including the MSWD, number of steps used, and percentage of total ^{39}Ar released in the plateau segment; and (3) the inverse isochron age, including MSWD and initial $^{40}Ar/^{36}Ar$ ratio (e.g., Lanphere and Dalrymple, 1976; Dalrymple et al., 1988). Criteria for recognition of a plateau are those of Ludwig (2003, and references therein), with the additional requirement that the plateau should consist of contiguous steps containing >50 percent of the released ^{39}Ar (Fleck et al., 1977).

Eight least altered extrusive and intrusive rocks from the Sari Gunay volcanic complex mostly yield age spectra with good plateaus and calculated plateau ages that are within error of the inverse isochron ages. However, the plateau for sample DK44 consists of only 47 percent of the released ^{39}Ar, and the steps decrease sequentially in age, suggesting the

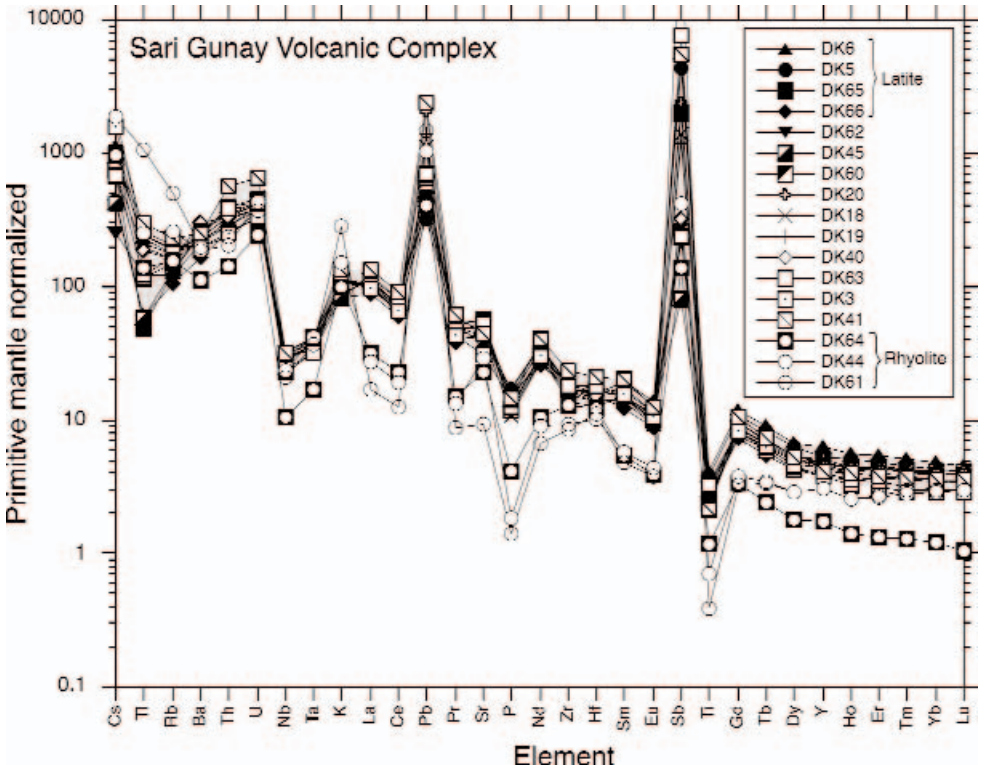

FIG. 10. Primitive mantle-normalized trace element diagram, showing least altered igneous rocks from the Sari Gunay volcanic complex. Intermediate lithologic (latite, andesite, trachyte, dacite) group tightly (range shown in gray background), but rhyolitic rocks are relatively depleted in HFSE and REE. Normalization values from Sun and McDonough (1989).

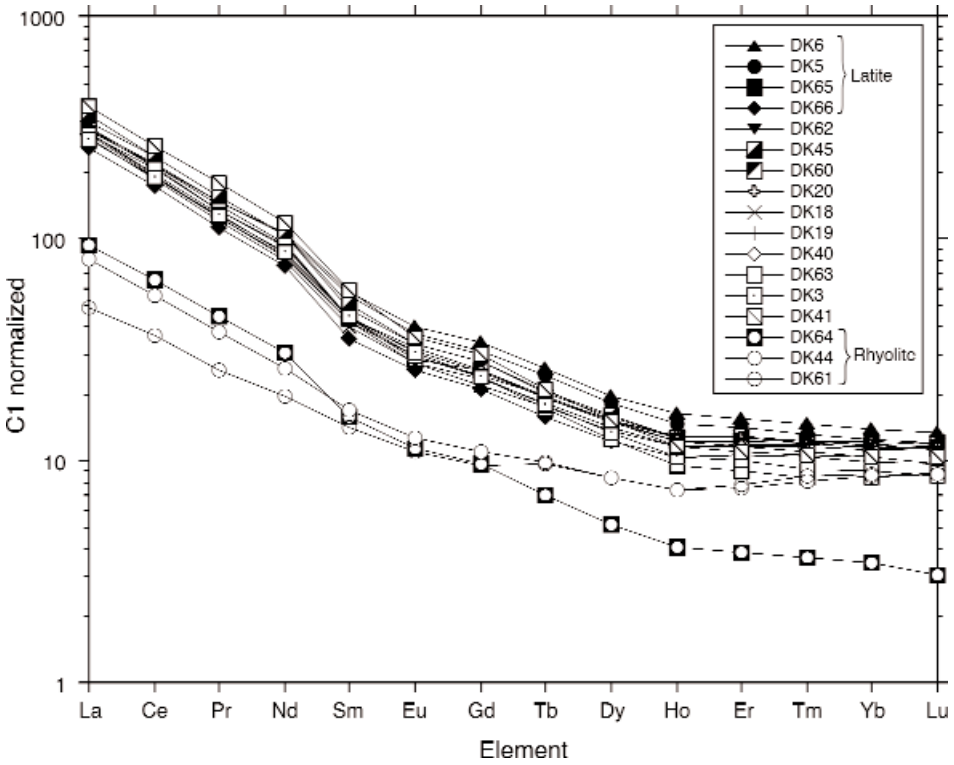

FIG. 11. Chondrite-normalized REE diagram, showing least altered igneous rocks from the Sari Gunay volcanic complex. Rhyolites are depleted in LREE and MREE relative to intermediate lithologic units, which group tightly. Sample DK64 has a younger age from the rest of the suite and has a distinctively low MREE-HREE pattern. Normalization values from Sun and McDonough (1989).

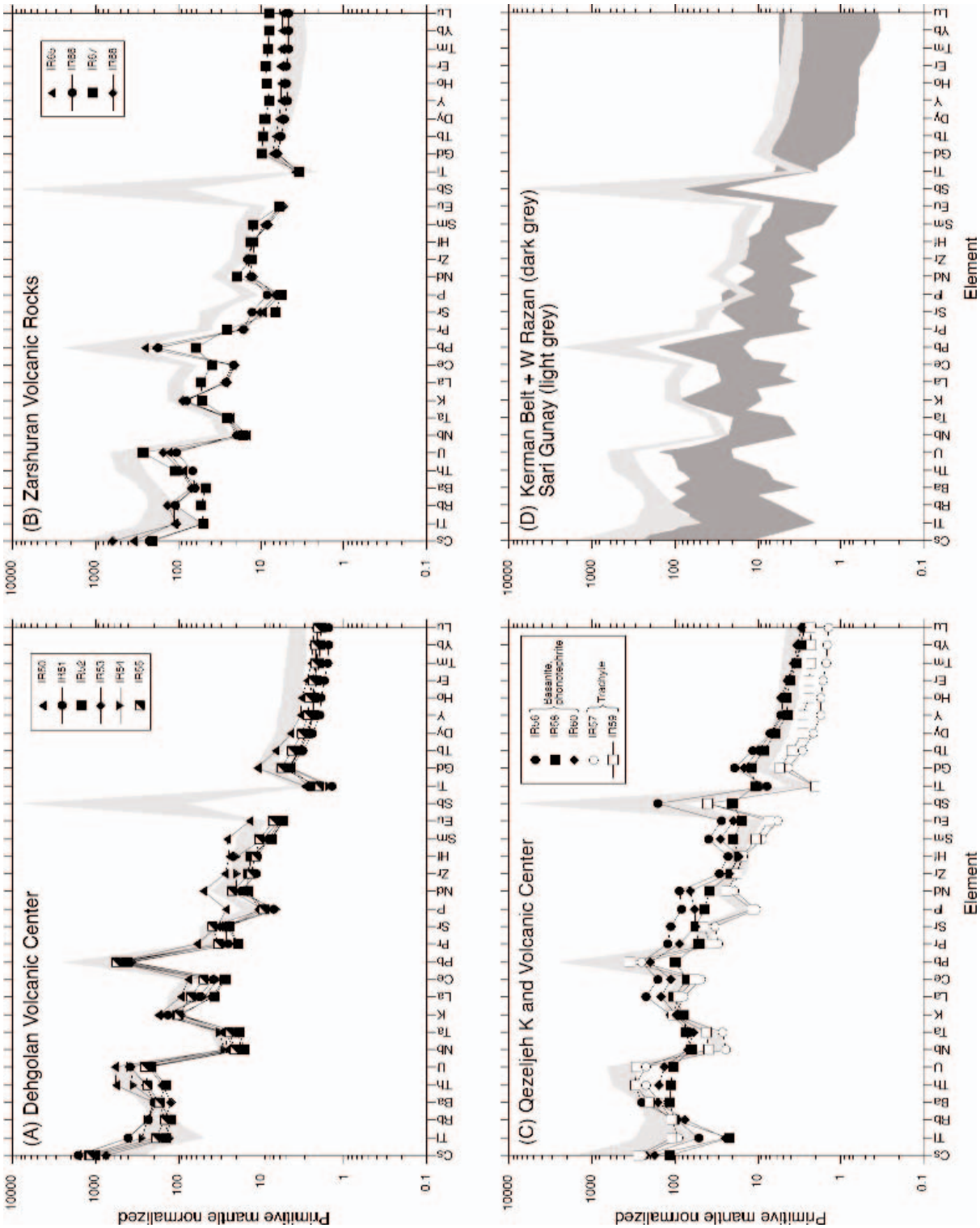

FIG. 12. Primitive mantle-normalized trace element diagrams, showing compositions of igneous rocks from the Takab belt (A–C) and the Kerman belt (D), compared with the range of compositions of intermediate rocks from Sari Gunay (light gray). Normalization values from Sun and McDonough (1989). See text for discussion.

TABLE 3. Summary of $^{40}Ar/^{39}Ar$ Dating Results for Samples from the Sari Gunay and Qezeljeh K and Volcanic Complexes[1]

Sample no.	Lithology (total alkali-silica)	Mineral	Integrated age ±2σ (Ma)	Plateau age ±2σ (Ma)	MSWD	No. of steps in plateau/ total steps	%^{39}Ar released (plateau)	Inverse isochron age ±2σ (Ma)	MSWD	Initial $^{40}Ar/^{36}Ar$[2]
Igneous minerals: main volcanic complex										
DK3	Dacite (hi K)	Biotite	10.59 ± 0.27	11.03 ± 0.16	0.43	7/12	84.1	11.07 ± 0.43	0.44	290 ± 17
DK20	Dacite (hi K)	Biotite	10.56 ± 0.26	11.16 ± 0.16	0.61	8/13	94.6	10.99 ± 0.50	0.68	299 ± 26
DK41	Trachyte (hi K)	Biotite	11.28 ± 0.19	11.01 ± 0.12	0.69	11/11	100	11.02 ± 0.07	0.70	293 ± 6
DK44	Rhyolite (hi K)	Biotite	11.46 ± 0.11	11.39 ± 0.07[4]	1.30	3/11	46.6	11.17 ± 0.12	0.40	375 ± 31
DK60	Trachyte (hi K)	Biotite	10.85 ± 0.11	11.09 ± 0.10	0.30	4/11	83.6	11.03 ± 0.41	0.49	298 ± 17
DK62	Trachyte (hi K)	Hornblende	11.61 ± 0.24	11.69 ± 0.12	0.63	7/8	84.2	11.69 ± 0.14	0.75	295 ± 4
DK66	Latite (med K)	Hornblende	11.18 ± 0.19	11.21 ± 0.13	0.81	10/10	100	11.24 ± 0.17	0.76	294 ± 3
Igneous minerals: younger volcanic rocks										
DK64	Younger rhyolite (med K)	Biotite	8.00 ± 0.08	8.03 ± 0.06	0.85	9/9	100	8.04 ± 0.06	0.92	294 ± 4
IR57	Qezeljeh Kand dacite (med K)	Biotite	0.57 ± 0.15	0.76 ± 0.06	1.05	5/9	74.9	0.75 ± 0.10	1.30	297 ± 15
Hydrothermal sericite										
DK26	Sericitized porphyry	Sericite	10.83 ± 0.10	10.69 ± 0.10	1.50	6/10	53.9	10.68 ± 0.14	1.46	296 ± 21
DK28	Sericitized porphyry	Sericite	11.38 ± 0.11	10.27 ± 0.10	1.60	4/10	25.3[3]	10.33 ± 0.14	1.70	261 ± 130
DK42	Sericitized porphyry	Sericite	11.36 ± 0.17	10.83 ± 0.10	1.60	5/9	42.4[3]	10.94 ± 0.33	1.90	264 ± 100

Notes: hi K = high K, med K = medium K

[1] Full isotopic data are listed in Table A1

[2] Expected composition of atmospheric argon = 295.5

[3] Samples DK28 and DK42 do not meet the commonly accepted criterion for a plateau of ≥50% of ^{39}Ar released (Fleck et al., 1977), but the plateaus are accepted as the best estimates of age

[4] Sample DK44 has a poorly defined, downstepping plateau and some evidence of minor excess ^{40}Ar; the inverse isochron age is therefore preferred

presence of minor amounts of excess ^{40}Ar (Fig. 13). In this case we prefer to use the inverse isochron age of 11.17 ± 0.12 Ma, and the slightly elevated initial $^{40}Ar/^{36}Ar$ ratio of 375 ± 31 confirms the presence of excess ^{40}Ar (Table 3).

With the exception of two samples, the igneous rock ages group tightly between 11.21 ± 0.13 Ma and 11.01 ± 0.12 Ma (samples DK3, DK20, DK41, DK44, DK60, DK66; all errors reported to 2σ). One sample of trachytic lava from the western part of the complex yielded a slightly older age of 11.69 ± 0.12 Ma (DK62), and one sample of rhyolitic pyroclastic rock yielded a younger age of 8.03 ± 0.06 Ma (DK64).

Three samples of sericite yielded well- to poorly constrained plateau ages between 10.83 ± 0.10 and 10.27 ± 0.10 Ma (DK26, DK28, DK42). The plateaus for samples DK28 and DK42 comprise less than 50 percent of the released ^{39}Ar (Fig. 13), and higher apparent ages for early steps in the spectra suggest the possibility of excess ^{40}Ar or minor loss of ^{39}Ar by recoil during irradiation. However, higher temperature steps do not appear to be affected by this problem, and the calculated plateau ages are within error of the inverse isochron ages. We therefore use these imperfect plateau ages as the best estimates of the ages of these samples and note that they agree reasonably well with the well-constrained plateau age of sample DK26 (10.69 ± 0.10 Ma).

The three sericite ages are up to 0.7 m.y. younger than the youngest dated intrusive rocks from Sari Gunay, consistent with the observation that mineralization and alteration overprint and are not crosscut by any intrusions. Within error, the oldest sericite date (10.83 ± 0.10 Ma: sample DK42) overlaps the youngest intrusion date (11.03 ± 0.16 Ma: sample DK3), such that there is no statistical separation of these two events.

The younger age for rhyolite sample DK64 (8.03 ± 0.06 Ma) suggests that a pulse of explosive felsic volcanism postdated both the main volcano-plutonic and hydrothermal stages of the complex.

A sample of hornblende-phyric dacite from the Qezeljeh Kand center to the northwest (Fig. 4) yielded a Quaternary age of 0.76 ± 0.06 Ma (IR57), confirming the much younger age of this system.

Geology of the Sari Gunay Epithermal Deposit

Main lithologic units

The Sari Gunay and Agh Dagh peaks (which respectively mean "Yellow or Sunny Place" and "White Mountain" in Turkish) are thought to represent the eroded roots of a large central volcano (Fig. 14). Exploration drilling and surface exposures on these hills have revealed a variety of hypabyssal intrusive and fragmental rock types, interpreted to be the core of a composite volcano that was breached by diatreme eruptions and later hydrothermal breccias. Several different lithologic units are recognized for the purposes of core logging and field mapping, including "andesite porphyry," "latite porphyry," "dacite porphyry," diatreme breccias and tuffisites, and quartz-tourmaline hydrothermal breccias (D.L. Wilkinson, unpub. report for Zar Kuh Mining Co., 2005, 87 p.). Broadly speaking, the subvolcanic units correspond to the latite and trachyte and/or dacite volcanic rocks described above, although hydrothermal alteration of rocks within the mineralized system hinders lithologic classification based on total alkali-silica compositions in many cases (see below). Several subdivisions of each unit, based on texture and

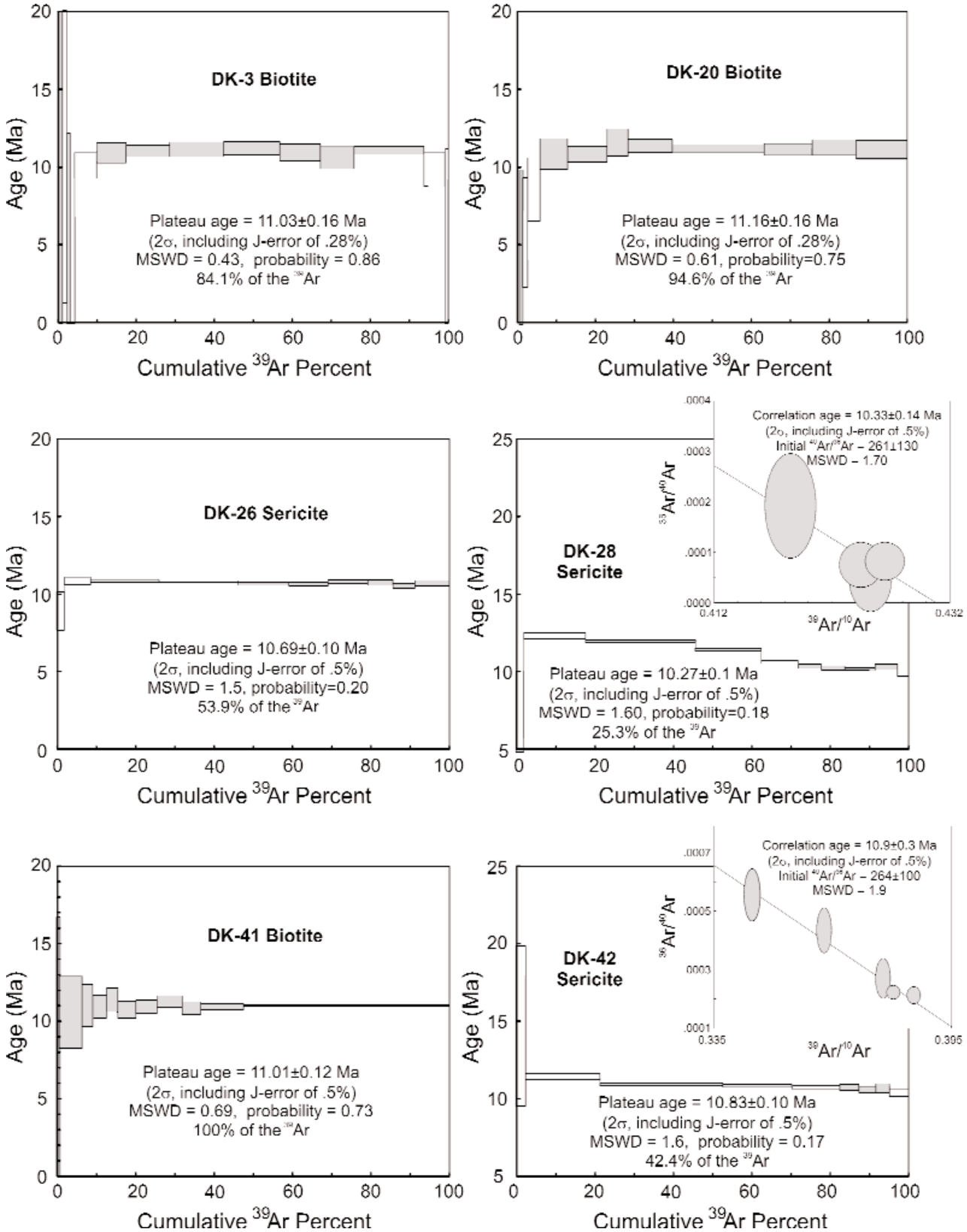

FIG. 13. Apparent $^{40}Ar/^{39}Ar$ age spectra for 12 samples of igneous hornblende and biotite and hydrothermal sericite from the Sari Gunay volcanic complex and nearby Qezeljeh Kand volcanic center. Three samples (DK28, DK42, and DK44) yielded poorly defined plateau ages, and inverse isochron correlation diagrams are included as a check for the accuracy of these age estimates. See Tables 3 and A2 for a summary of age data and complete isotopic data, respectively.

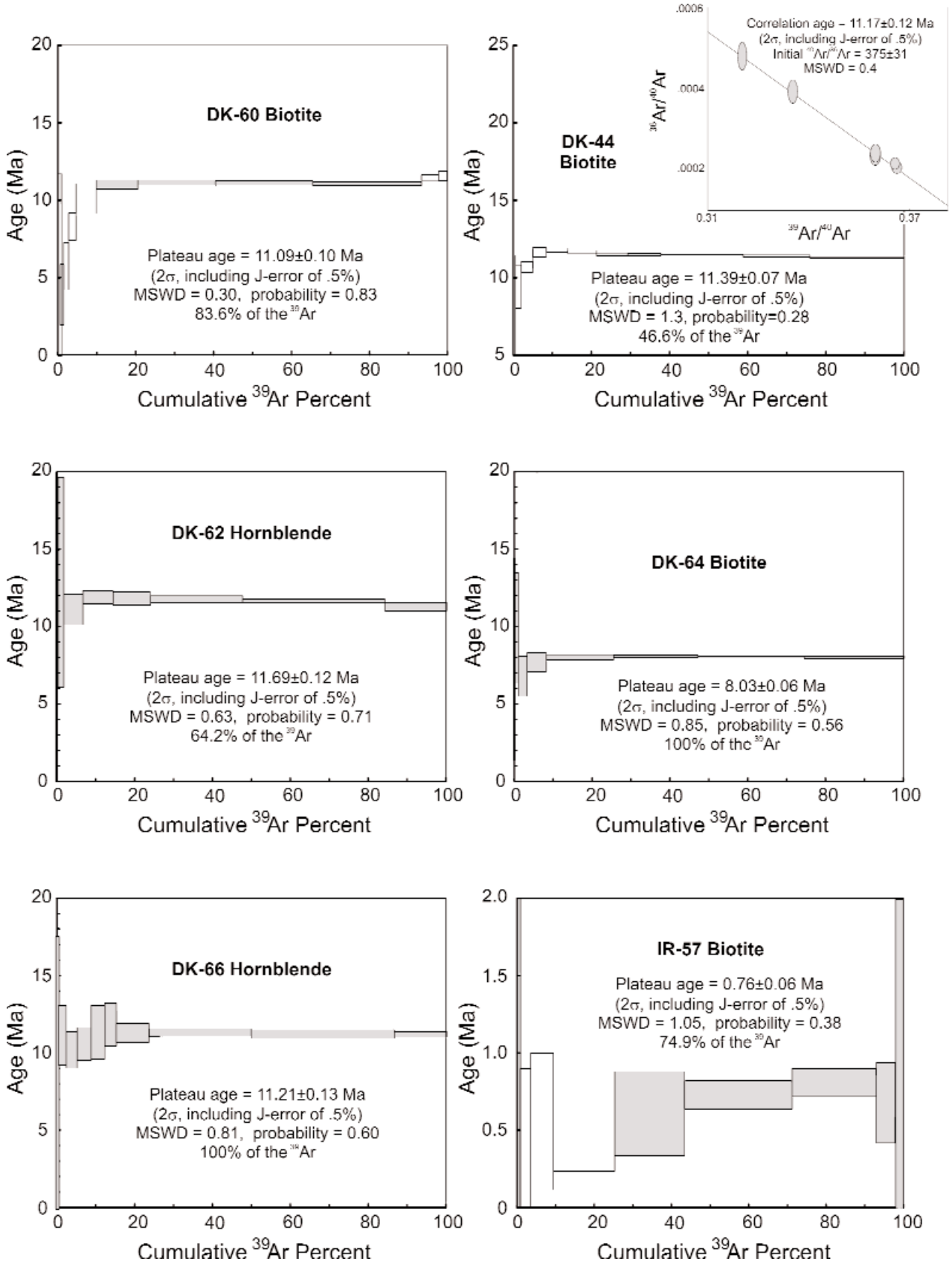
DK-60 Biotite
Plateau age = 11.09±0.10 Ma
(2σ, including J-error of .5%)
MSWD = 0.30, probability = 0.83
83.6% of the 39Ar
DK-44 Biotite
Correlation age = 11.17±0.12 Ma
(2σ, including J-error of .5%)
Initial 36Ar/40Ar = 375±31
MSWD = 0.4
Plateau age = 11.39±0.07 Ma
(2σ, including J-error of .5%)
MSWD = 1.3, probability=0.28
46.6% of the 39Ar
DK-62 Hornblende
Plateau age = 11.69±0.12 Ma
(2σ, including J-error of .5%)
MSWD = 0.63, probability = 0.71
64.2% of the 39Ar
DK-64 Biotite
Plateau age = 8.03±0.06 Ma
(2σ, including J-error of .5%)
MSWD = 0.85, probability = 0.56
100% of the 39Ar
DK-66 Hornblende
Plateau age = 11.21±0.13 Ma
(2σ, including J-error of .5%)
MSWD = 0.81, probability = 0.60
100% of the 39Ar
IR-57 Biotite
Plateau age = 0.76±0.06 Ma
(2σ, including J-error of .5%)
MSWD = 1.05, probability = 0.38
74.9% of the 39Ar
Age (Ma)
Cumulative 39Ar Percent
36Ar/40Ar
39Ar/40Ar

FIG. 13. *(Cont.)*

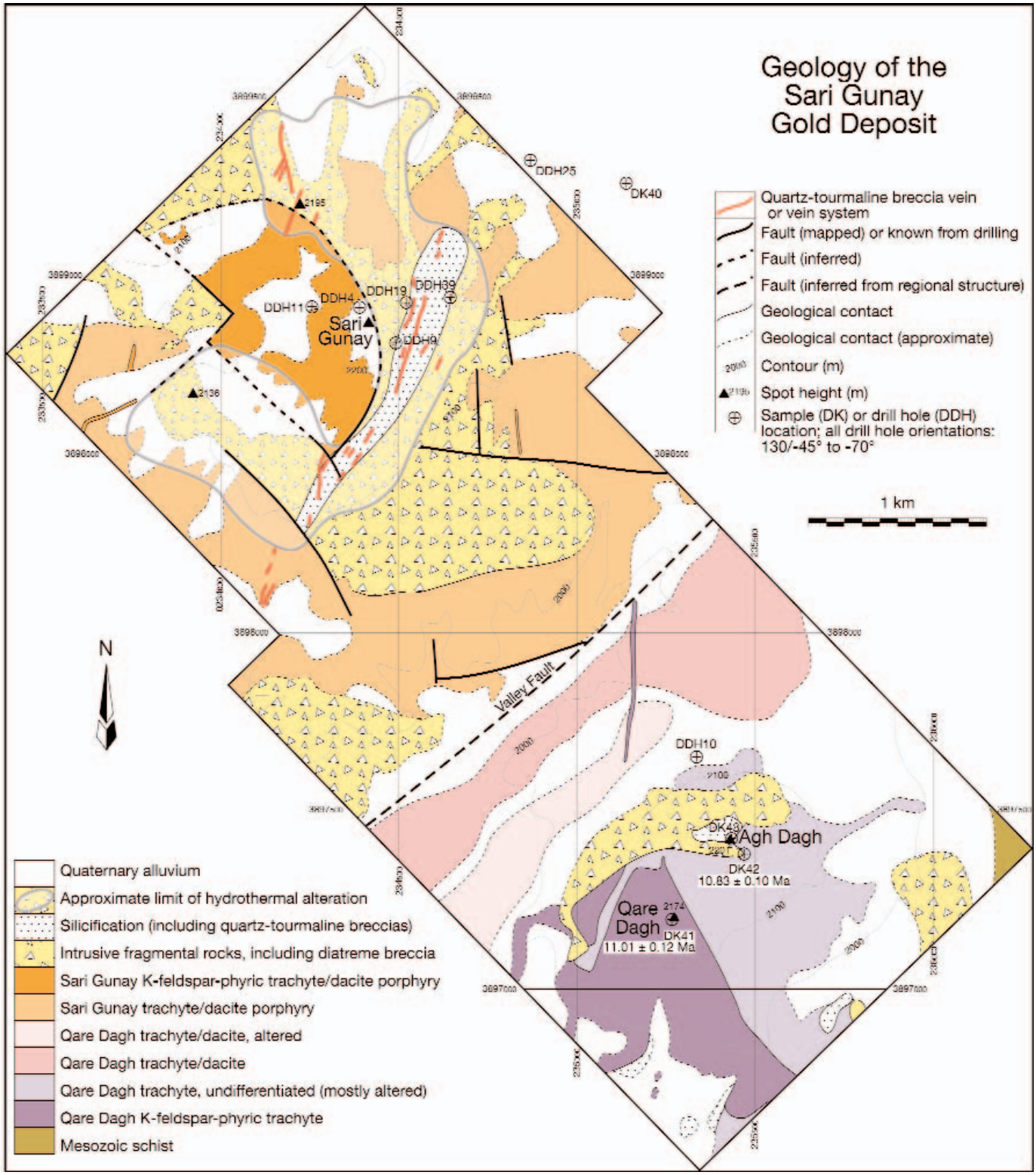

FIG. 14. Geologic map of the Sari Gunay and Agh Dagh subvolcanic and hydrothermal centers, compiled and simplified from company maps by D. Wilkinson and M. Namin (Zar Kuh Mining Company; UTM zone 39S).

phenocryst proportions, are applied for core-logging purposes. Some of the most distinctive rocks are trachytes containing large (centimeter-sized) sanidine phenocrysts (with lesser plagioclase, biotite, hornblende, and minor quartz). These rocks crop out on Qare Dagh ("Black Mountain," so-named because the fresher igneous rocks on this peak are dark colored; e.g., sample DK41) and also occur locally as small intrusions in drill core. Somewhat more mafic hornblende-bearing porphyries (latites) are encountered in drill core (e.g., samples DK5, DK6), but the majority of the intrusive rocks are biotite-plagioclase-phyric trachytes or dacites.

Crosscutting these subvolcanic rocks are two, steeply dipping, partial ring-shaped diatreme breccia and tuffisite bodies, one centered on Sari Gunay and the other on Agh Dagh (Fig. 14). These intrusive fragmentary bodies have been classified for core-logging purposes on the basis of clast composition and size and range from igneous clast-dominated breccias ("dacite crystal tuff"), through mixtures of igneous and basement clasts ("dacite lithic tuff"; Fig. 15A-B, to basement clast-dominated breccias ("lithic tuff breccia;" D. L. Wilkinson, unpub. report for Zar Kuh Mining Co., 2005, 87 p.); peperites are also recognized. Clast sizes range from 1 to 20 cm in size and are subangular to angular in shape. Lithic clasts consist of any of the basement lithologic units, including schist, siltstone, and earlier volcanic rocks. The matrix consists of disaggregated igneous crystals (hence the tuff terminology) and may show strong flow-banding and bedding textures. These breccia units are thought to have been generated by hydrovolcanic eruption processes and appear to postdate all other intrusive rocks (breccias are not observed to be crosscut by later intrusions).

Spatially associated with and overprinting these diatreme breccias are quartz-tourmaline hydrothermal breccia bodies, the largest of which forms a north-northeast–trending zone of silicification extending for almost 2 km on the southeast flank of Sari Gunay (Fig. 14). This body hosts the main high-grade ore zone (see below) and may have been emplaced along the same planes of structural weakness that localized the diatreme breccias. Quartz-tourmaline breccias range from clast to matrix supported (Fig. 15C), and sedimented geopetal textures are locally visible (Fig. 15D), particularly toward the margins of the breccia systems. Clasts within these hydrothermal breccias are typically derived from the local host rock, suggesting limited vertical transport; indeed, some breccias have a jigsaw-puzzle texture, suggesting in situ hydraulic fragmentation. The matrix consists of a dark-colored mixture of very fine grained blue-green tourmaline needles and quartz, with minor pyrite and rutile.

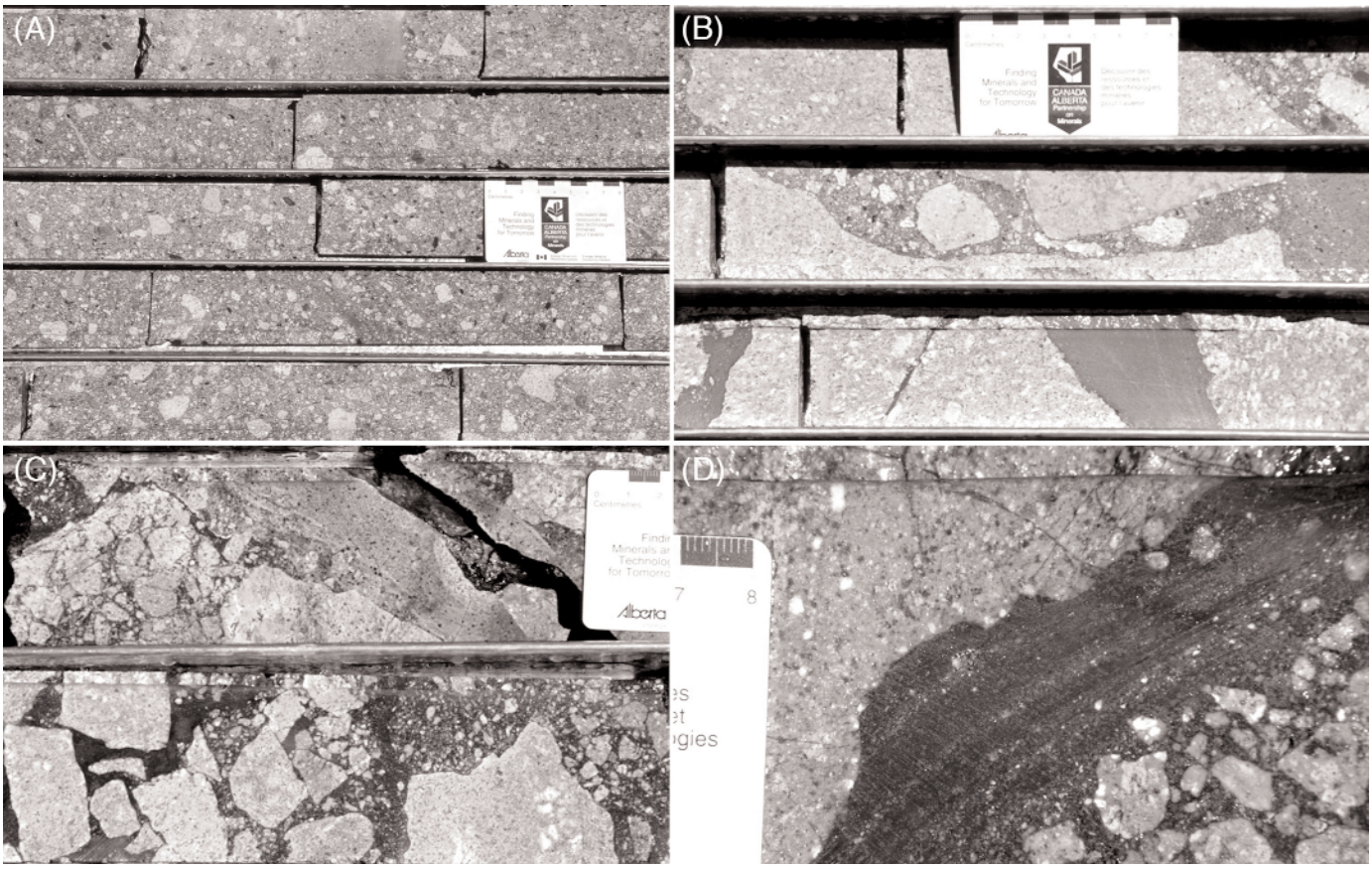

FIG. 15. Breccia textures in drill core. (A). Dacite lithic tuff, dominated by igneous clasts set in a matrix of disaggregated, tuffaceous igneous fragments and crystals (DDH10, 264–268m). (B). Intrusive breccia with andesite porphyry clasts cutting dacite porphyry; clasts include locally derived dacitic wall rock and sparse basement fragments (DDH10, ~215 m). (C). Quartz-tourmaline–cemented hydrothermal breccia (DDH19, ~106 m). (D). Detail of quartz-tourmaline–cemented hydrothermal breccia, showing sedimented textures (DDH19, ~110 m).

Although quartz-tourmaline breccias have also been encountered in drill core below Agh Dagh, they are less extensive and gold grades are lower than in Sari Gunay. Tourmaline is not present in the silicified rocks on the summit of Agh Dagh, and X-ray diffraction analysis of one sample (DK43) revealed peaks only for quartz and cristobalite against a high background, likely due to opaline silica. This mineralogy suggests low-temperature alteration, possibly at a paleowater table, which contrasts with the higher temperature hydrothermally altered subvolcanic rocks from elsewhere in the system. This observation also suggests that these rocks may lie close to the paleosurface, indicating a shallower level of exposure than on Sari Gunay. Such a difference in exposure level could simply reflect the outward-dipping paleosurface of a large stratocone centered on Sari Gunay (with Agh Dagh located at lower elevation on the flank), or it could reflect differential uplift along the southwest-northeast–trending Valley fault between the two peaks (Fig. 14).

Hydrothermal alteration

Chloritization: Propylitic chlorite alteration is extensively but relatively weakly developed in the volcanic rocks surrounding the main hydrothermal zones at Sari Gunay and Agh Dagh. Chloritization mainly affects ferromagnesian phenocrysts, such as hornblende and biotite, and is associated with minor calcite-quartz-pyrite-galena ± sphalerite veining.

Sericitization: Sericitization is the most common form of hydrothermal alteration at Sari Gunay and shows a close relationship to zones of silicification and quartz-tourmaline breccia veining. The degree of sericitization falls away quite rapidly around individual veins, but within intensely veined zones it can be pervasive across widths of tens of meters (up to hundreds of meters wide in the central parts of the hydrothermal system where vein density is high; Fig. 16A). In igneous wall rocks, sericitization first destroys the matrix and plagioclase (and hornblende) phenocrysts, then biotite

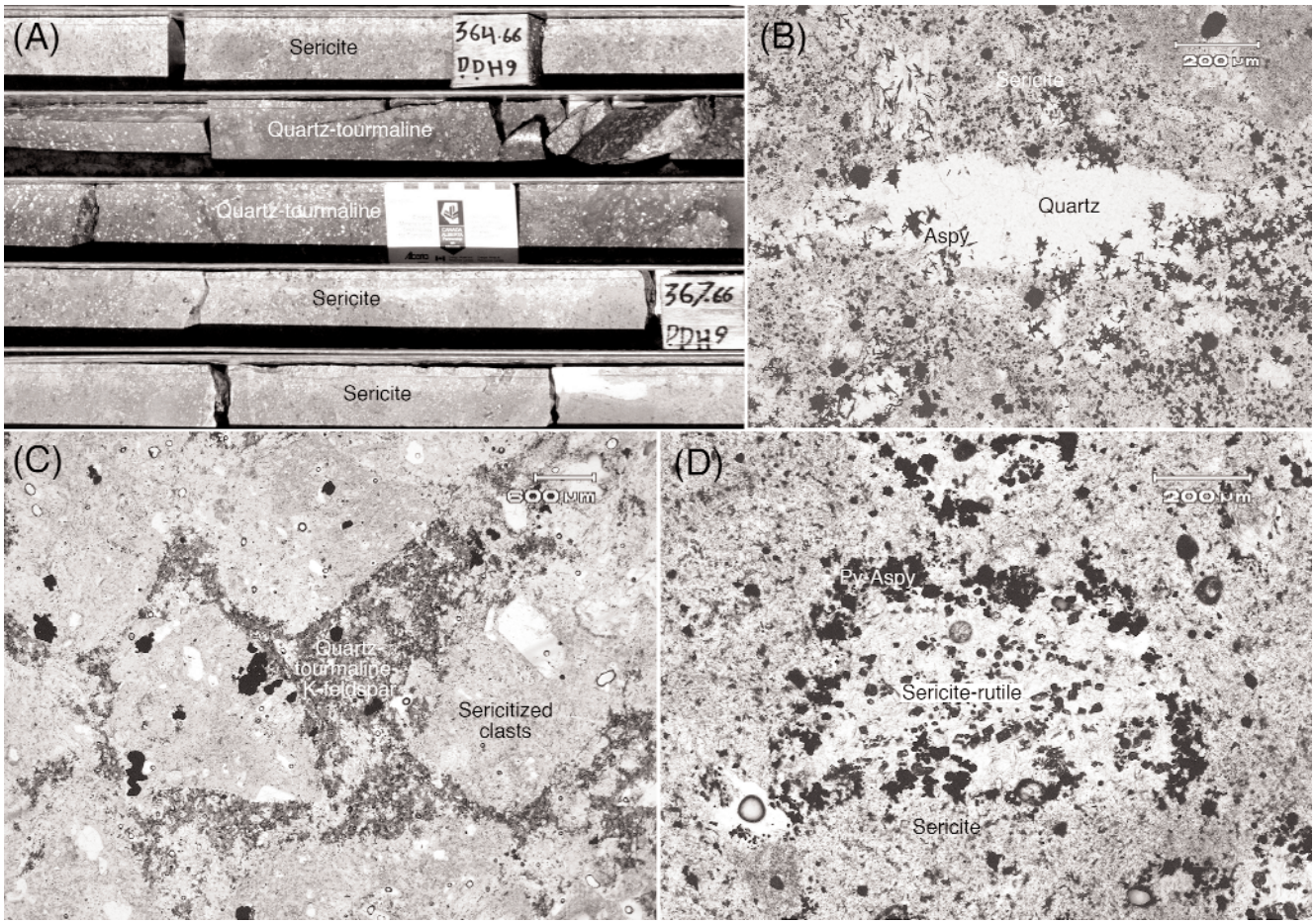

FIG. 16. Sericitic alteration in igneous rocks associated with quartz-tourmaline veining and brecciation. (A). Section of drill core from DDH9 (364–369 m), showing intensely sericitized halo (several meters wide) in dacite porphyry around a narrower inner zone of silicification and tourmalinization (darker gray); grades reach 33 ppm Au within the ~20-m-long zone of alteration that includes this section. (B). Photomicrograph showing quartz, sericite, and disseminated arsenopyrite rosettes in altered lithic tuff breccia (sample DK15: DDH10, ~201.5 m); this meter-length interval has a grade of 3.0 ppm Au. (C). Photomicrograph showing tourmaline-quartz-K-feldspar alteration of the matrix to dacitic breccia, with disseminated pyritohedra and intensely sericitized igneous clasts (sample DK29: DDH19, 104.7 m); this meter-length interval has a grade of 0.9 ppm Au. (D). Sericite pseudomorphous after biotite phenocryst and disseminated rutile, and rimmed by pyrite and minor arsenopyrite in sericitized matrix (sample DK26; DDH9, 415.4 m); this interval runs 3.6 ppm Au. All photomicrographs taken in plane-polarized light. Abbreviations: Aspy = arsenopyrite, Py = pyrite.

(sericite may be pseudomorphous after biotite; Fig. 16D). Minor amounts of carbonate also occur with sericite in less altered rocks. Rutile is a widespread minor alteration phase, particularly in pseudomorphs after mafic minerals (Fig. 16D), and pyrite is disseminated in sericitized rocks (Fig. 16B, D). This pyrite commonly contains small inclusions of chalcopyrite, galena, and rare stibnite, and overgrowths of fine-grained arsenopyrite. Sanidine phenocrysts have survived even quite extreme sericitization, suggesting that pH conditions were close to K-feldspar-sericite equilibrium (i.e., weakly acidic). Tourmaline locally occurs as fine green-brown-blue needles in this sericitic alteration (Fig. 16C), suggesting a close paragenetic relationship with the spatially associated quartz-tourmaline veins and breccias. This relationship becomes obvious at vein margins, where tourmaline, sericite, and quartz are intimately intergrown.

Tourmalinization and silicification: Tourmalinization and silicification, locally with fine-grained K-feldspar, characterize the inner zones of most intensive alteration, veining, and hydrothermal brecciation, and quartz and tourmaline represent the bulk mineralogy of veins and breccia cements. In altered wall rocks, tourmaline (and minor prehnite) commonly occurs as rosettes and clusters replacing mafic phenocrysts, as fillings in vesicles or drusy cavities and as small prisms disseminated in the matrix. Sericite also occurs with these minerals and is commonly preserved as pseudomorphs of plagioclase phenocrysts (white spots in the central part of Fig. 16A). The quartz-tourmaline-(sericite) assemblage therefore appears to indicate simply a greater intensity of alteration (higher fluid/rock ratios, closer to main fluid-flow path) rather than fundamentally different conditions from the more distal sericitic alteration. Infrared absorption spectra (using PIMA) indicate that the sericite is phengitic (i.e., enriched in Si and Fe) in the most intensely altered zones (D.L. Wilkinson, unpub. report for Zar Kuh Mining Co., 2005, 87 p.).

The largest zone of quartz-tourmaline alteration occurs on the southeast flank of Sari Gunay (Fig. 14) and coincides with the main mineralized zone. However, not all zones of quartz-tourmaline alteration are mineralized.

Low-temperature opaline silicification, without tourmaline, occurs on the peak of Agh Dagh, as noted above, and does not appear to be related directly to the higher temperature quartz-tourmaline alteration.

K-feldspar alteration: Potassic alteration typical of porphyry-type deposits is not well developed at current levels of exploration at Sari Gunay, but deep drilling (below ~300 m) has encountered zones of banded quartz-sulfide-magnetite veining associated with sericitization and minor K-feldspar alteration. The K-feldspar is not well developed, however, and conditions appear to have been close to K-feldspar-sericite equilibrium, as noted above.

Supergene alteration: Supergene oxidation extends to depths of 20 to 150 m, with partial oxidation locally extending to depths of ~300 m, commonly channeled by veins, joints, and fractures. In the oxidized zone, sulfides are replaced by oxides (limonite), jarosite, and rare alunite, and kaolinite locally replaces wall-rock feldspars or overprints sericite. Halloysite and montmorillonite have also been identified in PIMA spectra (D.L. Wilkinson, unpub. report for Zar Kuh Mining Co., 2005, 87 p.). Supergene oxidation is an important aspect of the project's economics, because much of the gold is refractory, being present as submicroscopic inclusions or in solid solution in sulfide minerals (see below); cyanide-leach recoveries of gold are consequently low in sulfide ores (5–15%). However, oxidation of these sulfide minerals has released the gold and made it much more amenable to cyanide leaching. High gold recoveries are obtained in test samples even from the partially oxidized zones because of preferential oxidation of sulfides in veins and fractures by downward percolating ground waters.

Vein paragenesis

The Sari Gunay hydrothermal system preserves a fairly simple record of veining, starting with high-temperature, porphyry-like veins, locally intersected at depth, followed by quartz-tourmaline brecciation and veining, and a final stage of epithermal-style quartz-pyrite-stibnite-realgar-orpiment veining, with which the bulk of the gold mineralization is associated. These vein styles are described below.

Quartz-sulfide-magnetite veins: Sparse porphyry-style banded quartz veins containing minor amounts of pyrite, chalcopyrite, tennantite, and magnetite have been encountered locally at depth beneath the main zone of quartz-tourmaline brecciation and epithermal mineralization. These veins are associated with sericitic and minor K-feldspar wall-rock alteration, and result in low-grade Cu mineralization (avg ~0.25 wt % Cu, locally up to 0.6 wt % Cu) with ≤0.5 ppm Au (except where overprinted by later epithermal veins, where grades may reach 4 g/t Au).

With increasing intensity of veining, magnetite (commonly partially oxidized to hematite) becomes dominant over sulfides and forms dark selvages to the veins. These veins locally form sheeted sets in silicified and sericitized wall rocks (Fig. 17A-B). Some relict biotite and K-feldspar is preserved in the wall rocks, but the dominant alteration style is sericitic (phyllic) as opposed to potassic. Quartz is typically fine grained and mosaic textured, suggesting recrystallization (Fig. 17C). Similar banded quartz-magnetite veins have been described by Muntean and Einaudi (2000) from porphyry gold deposits in the Maricunga belt of northern Chile, which they consider to have been formed by shallow-level exsolution and flashing of magmatic-hydrothermal fluids, leading to gold deposition. At Sari Gunay, however, these veins are largely barren or subeconomic, except where overprinted by later epithermal veins (see below).

Iron carbonates (mostly siderite, with minor ankerite and ferroan dolomite), intergrown with pyrite, chalcopyrite, tennantite, green-brown tourmaline, euhedral quartz, and minor K-feldspar are locally present as vuggy centerline fillings of veins (Fig. 17D) and as late fracture fillings. These late vein fillings provide a mineralogical link to the subsequent quartz-tourmaline vein stage.

Quartz-tourmaline veins and breccia cements: Quartz-tourmaline veins and breccias postdate the porphyry-style quartz-sulfide-magnetite veins (Fig. 17E) and are associated with intense sericitic wall-rock alteration that forms a halo up to tens of meters wide around major vein and breccia sets. The quartz-tourmaline veins contain only minor amounts of sulfide minerals, consisting mainly of pyrite (≤0.5 mm), fine-grained marcasite, rutile, and rare stibnite and alone do not

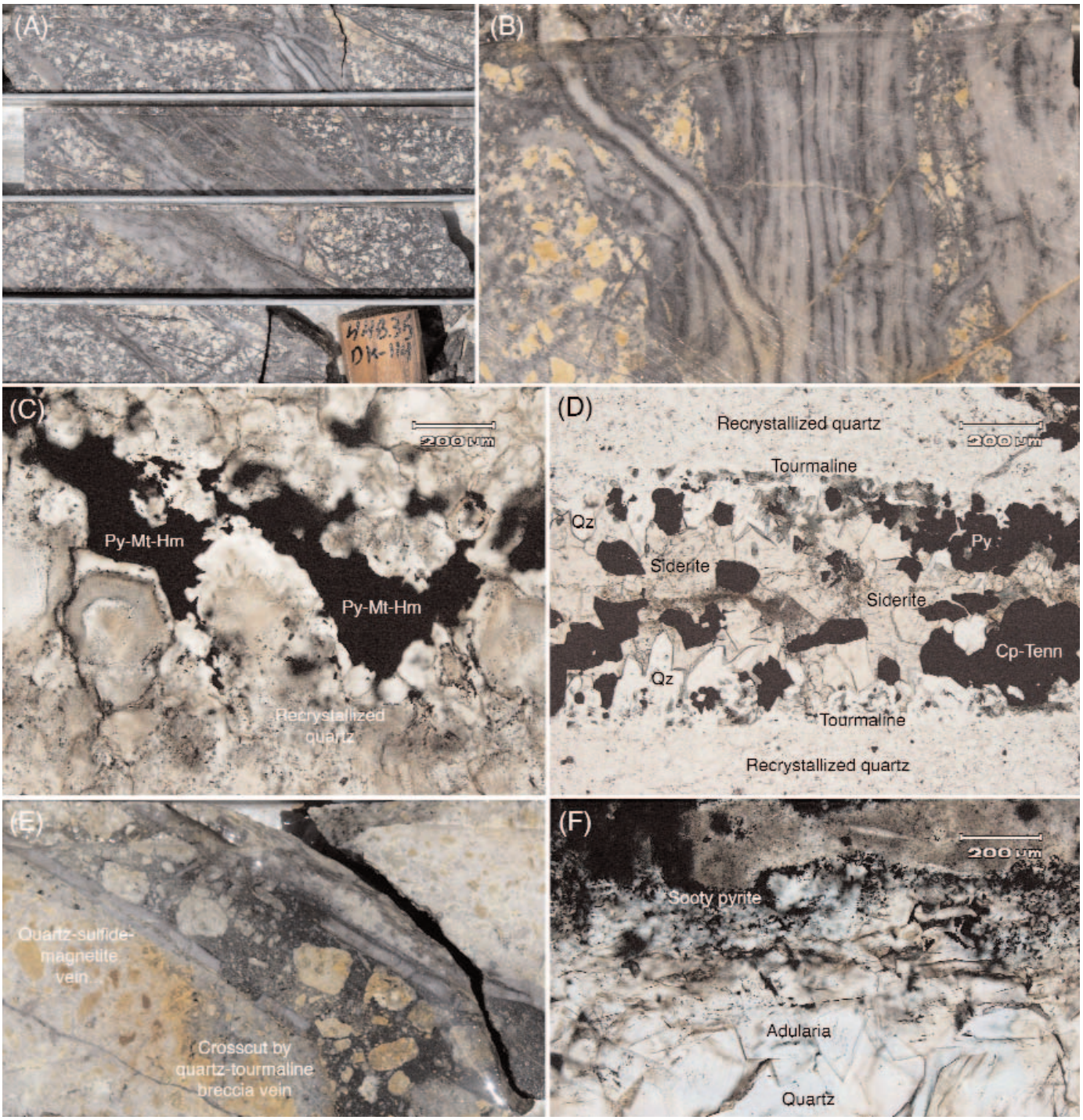

FIG. 17. Textures of early quartz-sulfide-magnetite veins (A–D) and quartz-tourmaline breccia veins (E–F). (A, B). Banded and sheeted quartz-magnetite veins cutting sericitized (white alteration) porphyry wall rocks in DDH114 (A: 445–448 m; B: sample DK78, ~479.3 m); cores are 4.5 cm wide (NQ). (C). Pyrite and magnetite partially replaced by hematite filling space between recrystallized but euhedrally terminated quartz, which is full of small vapor-rich fluid inclusions (sample DK78: DDH114, ~479.3 m). (D). Vuggy cavity in quartz-magnetite vein filled progressively (inward) by euhedral quartz and tourmaline, pyrite-chalcopyrite-tennantite, and siderite (sample DK74: DDH114, ~441.2 m). (E). Quartz-tourmaline breccia vein crosscutting and then following an earlier quartz-sulfide-magnetite vein (DDH104, ~407 m); core is 4.5 cm wide. (F). Adularia-quartz vein with fine-grained sooty pyrite at the vein margin and disseminated in sericitized wall rock (sample DK36: DDH19, ~336.8 m); this meter-length interval has a grade of 0.6 ppm Au. Abbreviations: Cp = chalcopyrite, Hm = hematite, Mt = magnetite, Py = pyrite, Qz = quartz, Tenn = tennantite.

carry significant gold grades. Adularia is also present in small amounts in early quartz-tourmaline vein stages but becomes increasingly important in later stages, displacing tourmaline to form quartz-adularia intergrowths and vuggy fillings (Fig. 17F).

The broad similarities in vein mineralogy (quartz + greater or lesser amounts of tourmaline) and alteration (sericite ± K-feldspar) between the early quartz-sulfide-magnetite veins and the later quartz-tourmaline veins provide a link between these two paragenetic stages, although the contrasting vein styles suggest a fairly abrupt transition in physical if not chemical conditions.

Epithermal quartz-pyrite-stibnite-realgar-orpiment veins: Gold was dominantly introduced in the Sari Gunay system during a late stage of epithermal veining, which largely followed the zone of structural permeability first formed by the diatreme breccias and then by the quartz-tourmaline breccias. Consequently, the large zone of quartz-tourmaline brecciation on the southeastern flank of Sari Gunay hosts the main zone of gold mineralization but did not introduce it.

The epithermal vein stage begins with the adularia-quartz veins noted above (Fig. 17F), and the best mineralized veins are recognized by the presence of "sooty pyrite," which gives the veins a dark gray to charcoal black appearance (Fig. 18A). The sooty pyrite is fine-grained ($\leq 10\ \mu$m) arsenical pyrite ± arsenopyrite, which forms at vein margins and in wall rocks, and commonly overgrows earlier pyritohedra (Fig. 18E). Gold appears to be present in solid solution within this sooty pyrite, and high gold grades are invariably related to the presence of these veins.

The epithermal veins are characterized by an increasing abundance of arsenic- and/or antimony-bearing minerals throughout their paragenesis. Early coarse-grained pyrite is overgrown by auriferous arsenical pyrite, then arsenopyrite and minor stibnite, followed by massive veins of stibnite (up to 0.5 m thick), and finally vuggy (locally massive) infillings of realgar, orpiment, and locally cinnabar (Fig. 18B-F). Fine wire gold very rarely occurs in late vuggy cavities in stibnite or realgar veins.

Base metal sulfide veins: Vuggy quartz-calcite-pyrite ± galena ± sphalerite veins containing elevated silver concentrations occur mainly outside the main gold-mineralized zones in areas of propylitic (chloritic) alteration. In this setting, they are similar to base metal sulfide veins found in the distal parts of porphyry copper and related epithermal deposits.

Vein structure

The dominant structural trend in the Sari Gunay hydrothermal system is 020°–030° (NNE–SSW), with dips from vertical to 70° WNW. This trend is displayed both by quartz-tourmaline veins and breccias, and by the later epithermal quartz-stibnite veins. Detailed structural studies have shown that this structural trend is formed by the combination of two separate north-south– and northeast-trending vein sets, both of which may be mineralized (D. L. Wilkinson, unpub. report for Zar Kuh Mining Co., 2005, 87 p.).

Reconnaissance Fluid Inclusion Study of the Sari Gunay Epithermal Deposit

Samples and methodology

Doubly polished thin sections (~100 µm thick) were cut from samples of quartz-sulfide-magnetite, quartz-tourmaline, and quartz-pyrite-stibnite veins (Table 4). Fluid inclusion assemblages were mapped and classified petrographically using the criteria of Roedder (1984) and Goldstein and Reynolds (1994) prior to microthermometric analysis using a Linkam THMSG600 heating and freezing stage. The stage was calibrated using a set of synthetic fluid inclusion standards from Syn Flinc, with a precision of ±0.1°C at subambient conditions and ±1°C at higher temperatures.

Salinities of liquid-rich fluid inclusions were calculated from measured ice-melting temperatures using the equation of Bodnar (1993), whereas the equation of Sterner et al. (1988) was used to calculate salinity from halite-melting temperatures in hypersaline inclusions.

Fluid inclusion types

Three types of primary fluid inclusions were recognized in vein samples from Sari Gunay: hypersaline inclusions (H) with halite daughter crystals at room temperature (Fig. 19A-B), liquid-rich inclusions (L) with small vapor bubbles (~5 vol %; Fig. 19C-E), and vapor-rich inclusions (V), rarely with a visible meniscus at room temperature and trace CO_2 (visible as small amounts of solid CO_2 at low temperature; Fig. 19A, E-F).

TABLE 4. Fluid Inclusion Samples

Sample no.	Description	Drill hole no.	Depth (m)	Surface or drill hole collar location (UTM 39S)		Fluid inclusion assemblages[1]
SG[2]	Vuggy quartz-carbonate vein		Surface	0234356E	3898539N	L, V
DK1	Quartz-pyrite breccia	DDH-11	61.6	0234258E	3898912N	L, V
DK7.1	Quartz-pyrite vein (0.7 ppm Au)	DDH-11	123	0234258E	3898912N	L+V
DK7.2	Quartz-stibnite vein + quartz-sericite wall-rock alteration	DDH-11	123	0234258E	3898912N	L, H+V
DK8	Quartz-pyrite vein + quartz-sericite wall-rock alteration	DDH-11	128.4	0234258E	3898912N	L+V, H+V
DK9	Quartz-pyrite vein	DDH-11	129	0234258E	3898912N	L
DK32	Quartz-stibnite vein (3.6 ppm Au)	DDH-9	125.3	0234489E	3898812N	L
DK34	Quartz-pyrite breccia (6.7 ppm Au)	DDH-9	194.6	0234489E	3898812N	L
DK37	Quartz-sericite-tourmaline altered porphyry (1.0 ppm Au)	DDH-9	376.8	0234489E	3898812N	L, H+V

Notes:
[1] Fluid inclusion types: H = hypersaline; L = liquid-rich; V = vapor-rich.
[2] Float sample from top of Sari Gunay hill; original location only approximately known

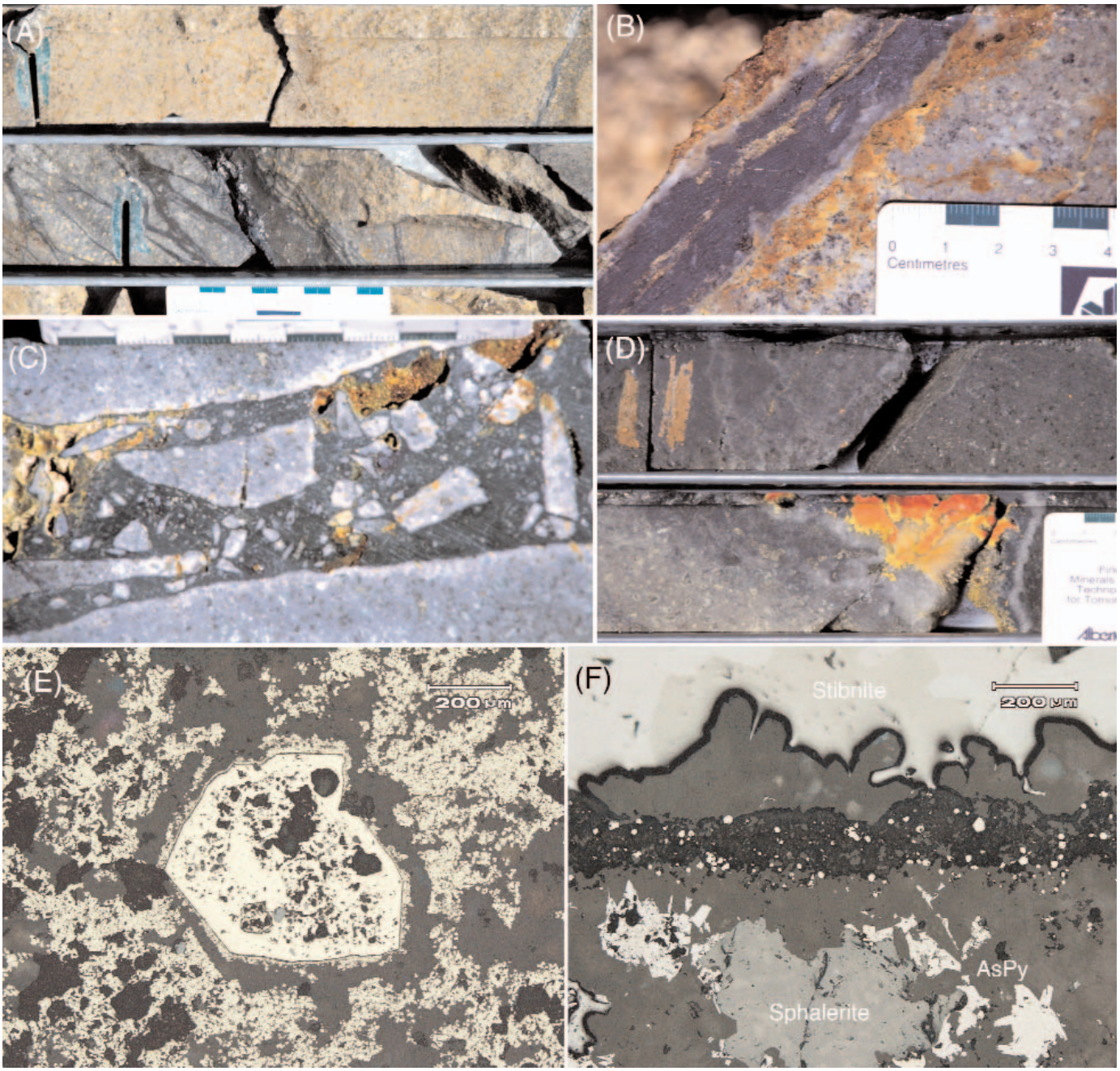

FIG. 18. Textures of epithermal quartz-pyrite-stibnite-realgar-orpiment veins; all drill core is 4.5 cm wide; photomicrographs are in reflected light. (A). Quartz-sooty pyrite-stibnite vein cutting earlier quartz-sulfide-magnetite veins and sericitic alteration (DDH113, ~503.6m). (B) Quartz-stibnite vein with orpiment impregnations in wall rock (sample DK32: DDH19, 125.3 m); this meter-length interval has a grade of 3.6 ppm Au. (C). Quartz-tourmaline breccia vein, with vuggy cavities infilling by late orpiment (DDH19, ~111 m). (D). Realgar and acicular orpiment overgrown by late chalcedony in a vug in a quartz-sooty pyrite vein (DDH43, ~322 m). (E). Early pyritohedron with small rutile inclusions (gray) overgrown by fine-grained sooty arsenical pyrite and stibnite (not in this field of view) set in fine-grained quartz (sample DK58: DDH43, 323.7). (F). Banded vein with early quartz-sphalerite-arsenopyrite-pyrite-galena (galena not in this field of view), followed by a band of sooty pyrite in fine-grained quartz, overgrown by euhedrally terminated quartz and vug-filling stibnite (sample DK52: DDH7; Agh Dagh), 114.3 m); this meter-length interval has a grade of 6.0 ppm Au.

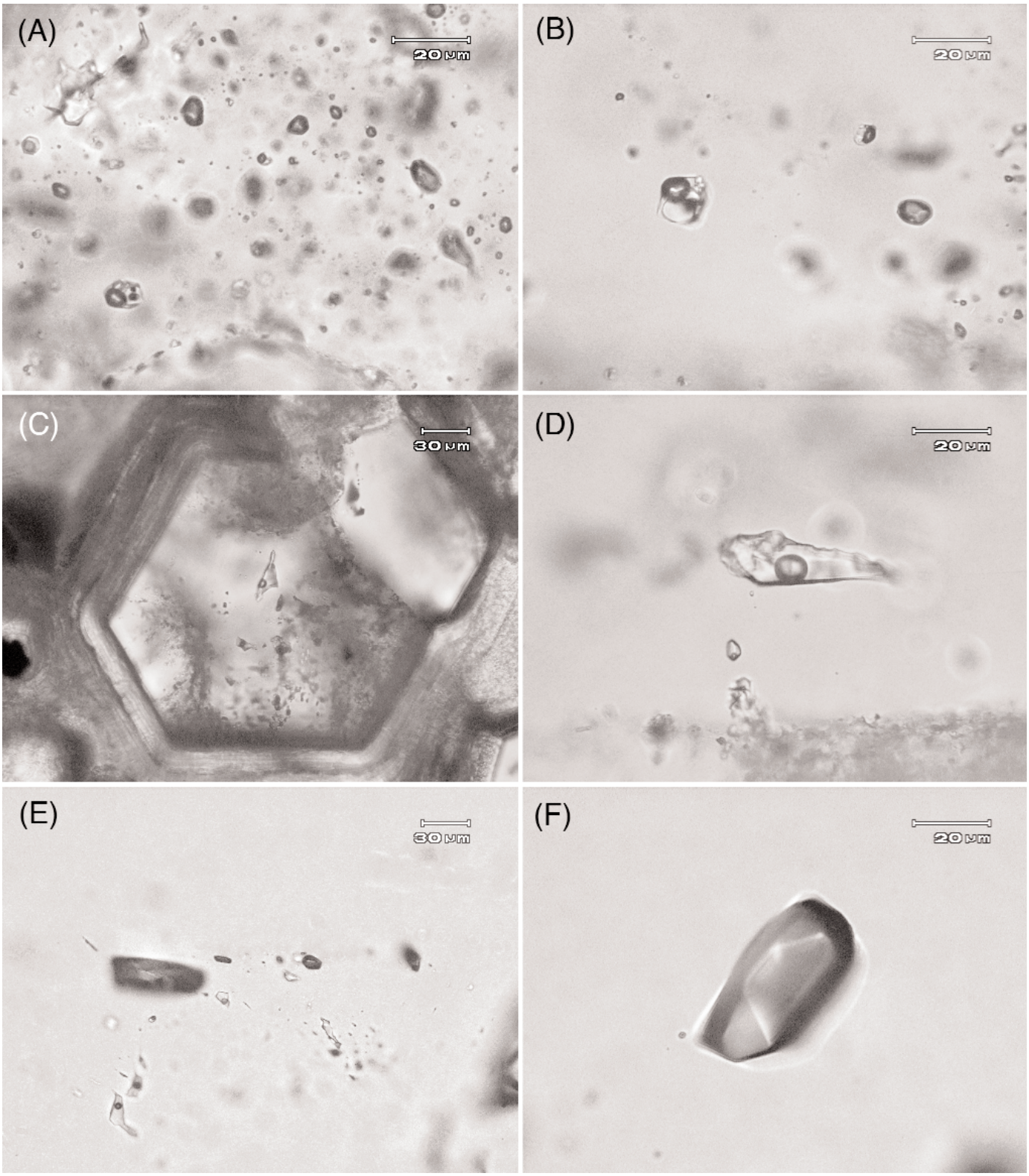

FIG. 19. Primary fluid inclusion types. (A). Abundant vapor-rich and sparse hypersaline fluid inclusions in partially recrystallized quartz from early quartz-magnetite vein (sample DK78: DDH114, 479.3 m; not analyzed). (B). Hypersaline and vapor-rich inclusions in quartz-tourmaline vein (DK37). (C). Liquid-rich inclusions in core of euhedral quartz crystal with chalcedony overgrowth, from quartz-pyrite-stibnite vein (sample DK7.2). (D). Liquid-rich inclusions from epithermal quartz-pyrite breccia vein (sample DK34). (E). Coexisting liquid- and vapor-rich inclusions in growth zone from epithermal quartz-carbonate vein; some necking visible (sample SG). (F). Large isolated vapor-rich inclusion (sample SG).

Four separate fluid inclusion assemblages were recognized (Table 4): (1) hypersaline inclusions commonly with vapor-rich inclusions (H + V), typically present in quartz-sulfide-magnetite and quartz-tourmaline veins, and their altered wall rocks; (2) and (3) liquid-rich inclusions (L), rarely with vapor-rich inclusions (L + V), typically present in quartz-pyrite-stibnite veins; and (4) vapor-rich inclusions (V), locally present in all vein types.

Fluid inclusions were best preserved in epithermal quartz-pyrite-stibnite veins (L, V, and rare L + V assemblages; Fig. 19C-F). In contrast, quartz-tourmaline veins contained few inclusions, and the quartz in quartz-sulfide-magnetite veins appears to have undergone extensive recrystallization, possibly from an original silica gel or amorphous silica (as suggested by Muntean and Einaudi, 2000). No data were obtained from the latter vein types, although abundant small vapor-rich and sparse hypersaline inclusions were visible (Fig. 19A).

Microthermometric observations

The results of fluid inclusion salinity and homogenization temperature measurements are illustrated in Figure 20 and are discussed in terms of host vein type below. The complete dataset is provided as a digital supplement to this paper at http://www.segweb.org.

Quartz-sulfide-magnetite veins: No microthermometric data were obtained from fluid inclusions in early quartz-sulfide-magnetite veins because of concerns about postentrapment modification, as noted above. However, the abundance of vapor-rich inclusions and the very high salinities of sparse hypersaline inclusions (as indicated by the large volume and variety of daughter minerals; Fig. 19A) suggest that these veins were formed at low pressures from a high-temperature fluid that had unmixed into a low-density vapor and a hydrosaline melt.

Quartz-tourmaline veins and quartz-sericite wall-rock alteration: Fluid inclusion assemblages from vein quartz intergrown with tourmaline (sample DK37) and secondary quartz in sericitized wall rocks (samples DK7.2 and DK8) consisted of hypersaline and rare vapor-rich inclusions. Hypersaline inclusions variably homogenized finally by halite or bubble disappearance, with a range of final homogenization temperatures from 246° to 360°C (although some inclusions contained daughter minerals that failed to dissolve at temperatures below 450°C). Salinities calculated for these hypersaline inclusions ranged from 34.4 to 46.1 wt percent NaCl equiv, and where halite dissolution also represented final homogenization, these inclusions define the halite saturation curve in Figure 20A.

Vapor-rich fluid inclusions commonly occurred in close proximity to hypersaline inclusions, suggesting low-pressure, two-phase fluid conditions at the time of trapping. The lack of a meniscus in these essentially monophase vapor inclusions made it impossible to determine salinities or homogenization temperatures. However, it was occasionally possible to detect melting of small amounts of solid at approximately –56.6°C, the melting point of pure CO_2, suggesting that the inclusions represent a low-density CO_2-rich vapor phase.

Secondary liquid-rich inclusions were commonly observed in tourmaline- and sericite-related quartz and are present as

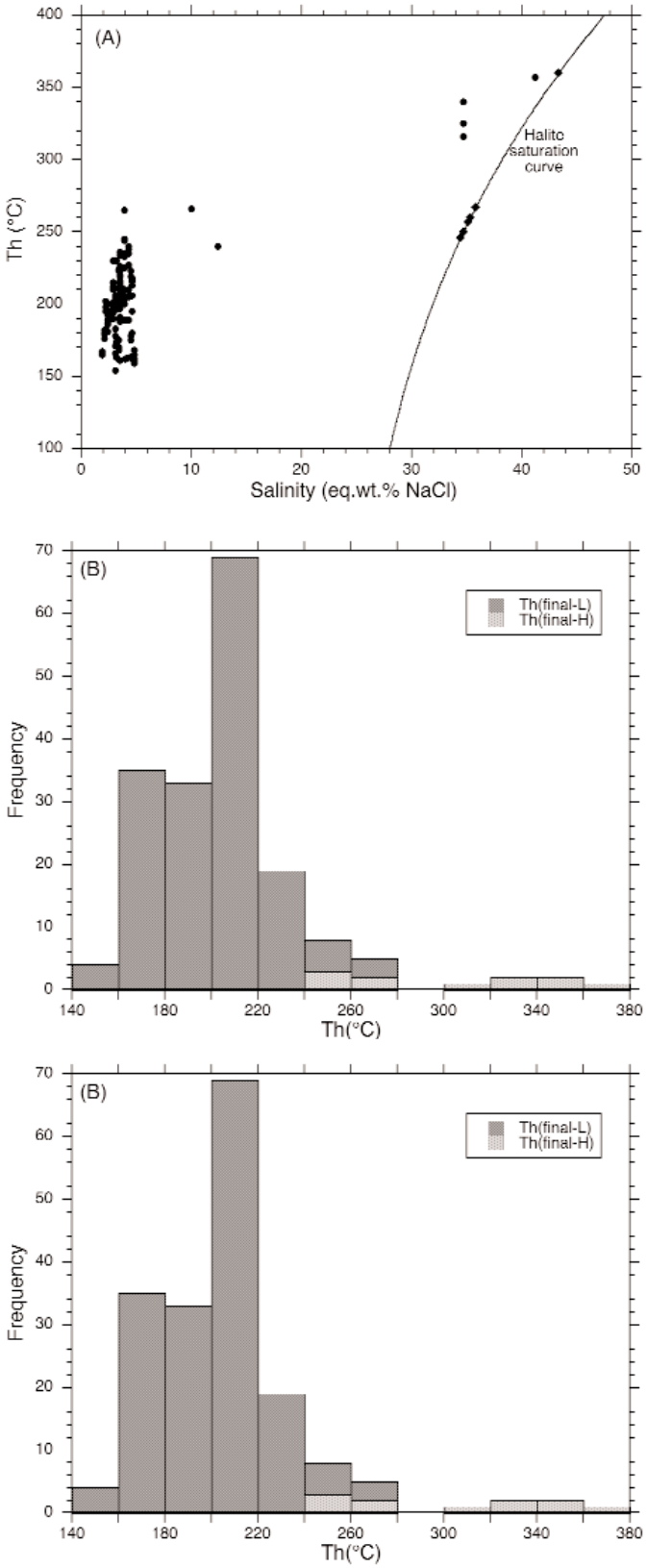

FIG. 20. (A). Salinity (wt % NaCl equiv) vs. final homogenization temperature (T_h) for all fluid inclusions from Sari Gunay for which paired data exist. (B). Histogram of homogenization temperatures for liquid-rich (L) and hypersaline (H) fluid inclusions. (C). Histogram of salinities for liquid-rich fluid inclusions.

primary inclusions in late-stage quartz in these veins, indicating transition to the later stage of epithermal mineralization.

Epithermal quartz-pyrite-stibnite veins: Low-salinity liquid-rich fluid inclusions are the most abundant type in epithermal quartz veins and define a relatively tightly grouped population with homogenization temperatures ranging from 143° to 267°C (avg = 199° ± 24°C) and salinities from 1.7 to 12.4 wt percent NaCl equiv (avg = 3.6 ± 1.1 wt % NaCl equiv; Fig. 20B-C).

Vapor-rich fluid inclusions were also present with liquid-rich inclusions in some assemblages or occurred as isolated groups. As in the quartz-tourmaline veins, no meniscus was visible in these vapor-rich inclusions, and observations of traces of solid CO_2 melting at ~–56.6°C similarly suggest that the vapor was CO_2 rich. Coexistence of fluid inclusions representing trapped vapor and liquid phases suggests that the system formed close to or on the two-phase field boundary and that homogenization temperatures (T_h) thus closely approximate trapping temperatures (T_t). Other evidence for shallow depths and low pressures of formation, such as the nature of the high-temperature fluid inclusion assemblages and the volcanic to subvolcanic geologic environment, support the interpretation that $T_h \approx T_t$ for most of these inclusions.

Estimates of trapping pressure are hampered by the lack of information about the composition and density of the coexisting vapor phase. However, pressures are unlikely to be much above the 15-bar vapor pressure of a boiling 5 wt percent NaCl solution (Haas, 1976), given the trace amounts of CO_2 detected in the vapor-phase inclusions. This low pressure indicates a shallow depth of formation of ~150 m (under hydrostatic pressure conditions).

Discussion

Regional tectonic and magmatic setting of the Sari Gunay volcanic complex

The central part of the Sari Gunay volcanic complex formed between 11.7 and 11.0 Ma (mostly from 11.2–11.0 Ma) with the eruption of latitic-trachytic lavas and emplacement of subvolcanic stocks and diatremes. A resurgence of felsic volcanism occurred locally at 8.0 Ma, and mafic to intermediate alkaline lavas and tephra were erupted ~20 km to the northwest in the Quaternary. Sericitic alteration associated with quartz-tourmaline veins in the gold deposit followed the main pulse of intermediate volcanism between approximately 10.8 and 10.3 Ma (best estimate of 10.69 ± 0.10 Ma: sample DK26).

The timing of magmatism and related hydrothermal activity at Sari Gunay are slightly younger than dates reported from the Sar Cheshmeh and Meiduk porphyry copper deposits in the Kerman segment of the Urumieh-Dokhtar magmatic arc (intrusion ages of 13.6 and 12.5 Ma, respectively; McInnes et al., 2003) and also unpublished dates for magmatism at the Sungun porphyry in northwestern Iran (12.5 Ma) and Reko Diq in the Chagai belt of western Pakistan (12–10 Ma; both dates cited in Hedenquist and Daneshfar, 2001). This middle Miocene pulse of calc-alkaline magmatism and associated porphyry-type mineralization in the Urumieh-Dokhtar and Chagai arcs has been related to final subduction of a segment of the Neo-Tethys ocean between the Afro-Arabian and Eurasian plates. However, the details of timing and location of this subduction and subsequent collisional event are unclear, with conflicting models proposing closure of a single Neo-Tethys ocean by the late Oligocene (e.g., Hooper et al., 1994; Agard et al., 2005) or closure of two separate oceans, Neo-Tethys I and II, in the Late Cretaceous and Miocene, respectively (e.g., Glennie, 2000; Fig. 2). Interpretation of the tectonic record in this part of the Tethyan suture zone is complicated by considerable postclosure faulting, extensive Quaternary cover, and the fact that subduction and collisional events were likely diachronous and localized (i.e., they involved a collage of oceanic and continental microplates, more analogous to the present-day southwest Pacific region than extensive, long-established destructive margins such as the western seaboard of the Americas). Indeed, subduction continues along the eastern continuation of the Eurasian continental margin beneath the Makran accretionary complex of southeastern Iran and western Pakistan (Fig. 1).

Reconciling these poorly constrained tectonic models with the magmatic history of central Iran is therefore difficult, but the evidence of widespread and voluminous calc-alkaline arc magmatism in the Urumieh-Dokhtar belt from the Eocene through the Miocene, followed by more alkaline volcanism, is consistent only with a model of subduction that continued beneath this region at least up to the Miocene, as suggested by Glennie (2000) and supported by plate motion studies that indicate subduction continued until ~10 Ma (McQuarrie et al., 2003; Fig. 2C–D).

A transition from calc-alkaline to alkaline magmatism in convergent orogens has been interpreted to signal the termination of subduction and readjustment to postcollisional tectonics (for example, as documented in the western extension of this collisional belt in Turkey: Pearce et al., 1990; Aldanmaz, 2002; Ilbeyli et al., 2004; see also Harris et al., 1986; Elburg and Foden, 1999; Paquette et al., 2003). The geochemically distinctive high K subalkaline to alkaline Sari Gunay suite, and related volcanic rocks along the Takab belt (Figs. 8, 12) may thus mark the onset of this tectonic transition in central-northwest Iran at ~11 Ma. This timing closely follows the main period of medium K calc-alkaline Eocene to Miocene magmatism that largely terminated with the emplacement of porphyry Cu deposits in the Kerman belt and at Sungun between 13.6 and 12.5 Ma. Subsequent volcanism along this belt became increasingly alkaline, with widespread but small volumes of undersaturated mafic lava being erupted in the Quaternary (Hassanzadeh, 1993; this study).

A collisional origin for the Takab belt magmas explains their slightly younger age and off-axis location with respect to the main Urumieh-Dokhtar arc (located ~100 km to the northeast; Figs. 1, 2D), in that the source of magmatism would no longer have been constrained to a narrow mantle wedge above the Benioff zone and beneath the overriding plate. Cessation of subduction leads to the rebound of mantle geotherms and has also been suggested to lead to slab breakoff or mantle lithosphere delamination, both processes potentially causing upwelling of hot asthenospheric material beneath the collisional orogen (e.g., Davies and von Blankenburg, 1995; Regard et al., 2003; Cloos et al., 2005).

Under such conditions, partial melting of previously subduction-modified mantle can generate small volumes of subalkaline to alkaline magma of the type recorded here (e.g., Johnson et al., 1978; Davies and von Blankenburg, 1995).

Metallogeny of collision-related alkaline versus calc-alkaline arc magmas

The onset of collision at destructive margins halts the process of mantle hydration and metasomatism that accompanies slab subduction and terminates the production of large volumes of calc-alkaline magma with which porphyry copper deposits are globally associated (see review by Richards, 2003b). In contrast, the smaller volumes of more alkaline magma formed during collisional and postcollisional readjustments are rarely but consistently associated with gold mineralization. Examples of postsubduction or back-arc alkalic-type gold deposits are the Porgera, Emperor, and Cripple Creek mines in Papua New Guinea, Fiji, and the United States, respectively. Each of these deposits is associated with hydrous mafic alkalic rocks ranging from basanites and trachybasalts through to trachytes and phonolites (see reviews by Richards, 1995, and Jensen and Barton, 2000).

The Sari Gunay magmatic suite is subalkaline in character rather than alkaline, but nevertheless consists of high K latites and trachytes, and shows significantly greater alkali and incompatible element enrichment than the medium K andesites and dacites typical of the older Urumieh-Dokhtar arc (Fig. 12D). The deposit is gold rich, with only weak development of porphyry-style Cu mineralization (at least in the presently explored system). In this respect, it more closely resembles the porphyry gold deposits of the Maricunga belt in Chile, as noted above, except that the main stage of gold deposition was related to the epithermal rather than the porphyry stage of hydrothermal activity.

It is likely that a continuum exists between calc-alkaline porphyry Cu and related epithermal Au-Cu deposits and alkalic-type porphyry Au and epithermal Au deposits, with end members reflecting established arc and postcollisional or back-arc tectonic settings, respectively (Richards, 1997; Kelley et al., 1998; Kelley and Ludington, 2002). The subalkaline nature of the Sari Gunay system may reflect a transitional timing between subduction and collision, as noted above. The cause of the change in metal endowment from Cu to Au rich with a switch from subduction to collision is not known, but several authors have speculated that it may relate to a breakdown of residual sulfide minerals in the subduction-modified asthenosphere, either by oxidation or multistage partial melting, leading to release of highly siderophile elements to the melt phase (e.g., Solomon, 1990; Richards and Kerrich, 1993; Spooner, 1993; Wyborn and Sun, 1994; Richards, 1995, 2005; Mungall, 2002). During subduction, a continuous flux of sulfur from the downgoing slab under moderately oxidizing conditions stabilizes at least some sulfide in the mantle wedge, although the bulk of the sulfur flux is present as SO_2. When subduction ceases, however, the flux of new sulfur diminishes and any further partial melting may cause the complete breakdown of residual sulfides, rendering highly siderophile elements incompatible with remaining mantle minerals (Jugo et al., 2005). As discussed by Richards (2005), this may explain the relatively low Au/Cu ratios of normal calc-alkaline porphyry systems (in which highly siderophile Au remains as a compatible element in residual sulfide phases in the mantle, whereas the bulk of more abundant and chalcophile Cu is dissolved in the melt), compared with the higher Au/Cu ratios of postsubduction alkaline systems, in which Au behaves as an incompatible element.

Formation of the Sari Gunay gold deposit

Sericitic hydrothermal alteration at the Sari Gunay gold deposit was formed within 0.7 m.y. (~10.8 to ~10.3 Ma) of the youngest dated intrusive rocks in the volcanic complex (11.0 Ma), with the best constrained age (sample DK26) being 10.69 ± 0.10 Ma. A younger rhyolitic pyroclastic deposit with an age of 8.0 Ma appears to represent a later, unrelated pulse of volcanic activity in the southwestern part of the complex. The even younger Quaternary basanitic and trachytic volcanism at Qezeljeh Kand, ~20 km to the northwest of the Sari Gunay volcanic complex, also appears to be unrelated to the Sari Gunay magmatic-hydrothermal system, except in terms of regional structural localization.

The hydrothermal system was superimposed on volcanic rocks and coeval hypabyssal intrusions of what is interpreted to have been a large composite volcano, and in particular was localized by zones of diatreme brecciation centered on the Sari Gunay and Agh Dagh hills. Because of the possibility of later block faulting with differential uplift, it is not possible accurately to determine the depth of formation of the currently exposed hydrothermal system. However, the close proximity to shallowly dipping volcanic rocks (Fig. 5) and the tuffaceous nature of much of the diatreme material suggest that depths were shallow, and the epithermal system may have formed within 150 m of the paleosurface, as suggested by the estimated trapping pressure of boiling fluid inclusion assemblages. The presence of voluminous lahar and debris avalanche deposits on the flanks of the complex furthermore suggest that erosional collapse of the volcanic edifice may have taken place coevally with hydrothermal activity.

The hydrothermal system everywhere postdates magmatic activity, with no intrusions having been observed to crosscut alteration or veining. However, the $^{40}Ar/^{39}Ar$ age determinations suggest that the interval between the last shallow-level intrusion and development of the hydrothermal system was ≤0.3 m.y. and may have in fact overlapped.

The earliest hydrothermal veining is associated with weakly developed potassic alteration and has only been encountered at depth (below ~300 m) beneath Sari Gunay. A core of locally intense, sheeted and banded quartz-magnetite veins is essentially barren of both Cu and Au, but this core appears to grade outward into a zone of sparse quartz-sulfide-magnetite veins, which generate grades typically of ~0.2 to 0.3 wt percent Cu and 0.3 to 0.5 ppm Au. Fine-grained recrystallized textures of the quartz-magnetite veins are similar to banded veins in the Maricunga porphyry gold systems of northern Chile, which Muntean and Einaudi (2000) attributed to formation at shallow depths of <1.5 km under hydrostatic pressure conditions. Aqueous fluids exsolved from a magma emplaced at such shallow depths would consist predominantly of a low-density vapor phase accompanied by a much smaller volume of high-salinity brine. Although fluid inclusions are not well preserved in these variably recrystallized veins, best

preserved assemblages do indeed consist of abundant vapor-rich (CO_2-bearing) inclusions, plus sparse very high salinity brine (hydrosaline melt) inclusions.

At shallower levels, but extending to unknown depth, zones of intense quartz-tourmaline veining and brecciation, with pervasive and intense sericitic wall-rock alteration, form the most noticeable manifestation of hydrothermal activity in the system. Although some tourmaline was noted in late-stage centerline fillings of quartz-sulfide-magnetite veins, the transition between these vein styles appears fairly abrupt and, together with the overlap in depth range, suggests telescoping of the system, perhaps due to unroofing as suggested above.

The quartz-tourmaline breccia bodies appear to have followed zones of structural weakness and high permeability formed by the diatreme breccias, with the largest silicified breccia system occurring on the southeast flank of Sari Gunay. Sparse fluid inclusions preserved in these veins and breccia cements consist of moderate-temperature brines (246°–360°C, 34.4–46.1 wt % NaCl equiv), locally coexisting with CO_2-bearing vapor-rich inclusions. Copper and gold grades in these breccias are low except where they are overprinted by later epithermal veins.

The main gold mineralized zone at Sari Gunay, although centered on the quartz-tourmaline breccia body, is in fact related to this later set of epithermal quartz-pyrite-stibnite-realgar-orpiment veins, which appear again to have followed the same zone of structural weakness and permeability first created by the diatreme system. Gold is present in these veins in solid solution in fine-grained (sooty) arsenical pyrite and minor arsenopyrite, and visible gold has only very rarely been observed in late vuggy cavities, in association with antimony and arsenic minerals such as stibnite, realgar, and orpiment. Fluid inclusion assemblages in these veins consist of much lower temperature and lower salinity liquid-rich inclusions (avg of 199° ± 24°C and 3.6 ± 1.1 wt % NaCl equiv), again locally coexisting with low-density, CO_2-bearing, vapor-rich inclusions.

The presence of carbonic vapor-rich fluid inclusions in all of the vein stages suggests that conditions were permanently in or close to the two-phase volume in pressure-temperature-composition (P-T-X) space. The presence of CO_2 will increase the pressure at a given temperature and salinity on the two-phase boundary, but only trace amounts of CO_2 were observed in these inclusions (never enough to form a condensed liquid phase), so the pressure increase is not likely to have been large. Thus, fluid pressures were likely below 100 bars in the quartz-tourmaline veins and perhaps as low as 15 bars in the epithermal veins (Haas, 1976), corresponding to depths at hydrostatic pressure conditions of less than 1 km to as shallow as 150 m. The decrease in pressure over time implied by these estimates again supports a scenario in which the volcano-plutonic complex was being actively unroofed at the time of hydrothermal vein formation, thereby telescoping a low P-T-X epithermal system onto an earlier higher P-T-X, but still quite shallow, porphyry-style system.

Gold appears to have largely remained in solution (or was not mobilized) throughout the earlier high-temperature hydrothermal stages and was only precipitated in significant concentrations during the lower temperature epithermal stage. Phase separation may have assisted gold deposition, as commonly proposed for epithermal vein deposits (e.g., Drummond and Ohmoto, 1985; Reed and Spycher, 1985; Seward, 1989; Cooke and Simmons, 2000). However, the intimate association with arsenical pyrite (in solid solution) suggests that a combination of sulfide precipitation and fluid cooling may have had a greater negative effect on gold solubility, by reducing dissolved sulfide concentrations in the fluid and thereby destabilizing gold-bisulfide complexes, as well as reducing overall metal solubility.

Conclusions

The Sari Gunay epithermal gold deposit was discovered in 1999 in central-northwest Iran, an area previously unknown for gold mineralization. The deposit was formed at ~10.7 Ma, shortly after construction of an 11.7 to 11.0 Ma composite volcano and diatreme complex. Hydrothermal activity may have coincided with destruction of the volcanic edifice by erosion and collapse.

Early hydrothermal activity produced weak porphyry-like quartz-sulfide-magnetite veining and potassic alteration but with low grades of copper and gold mineralization (~0.25 wt % Cu, ≤0.5 ppm Au). Later quartz-tourmaline veins and breccias similarly introduced little gold but provided a structurally prepared pathway for the passage of later epithermal fluids. The main stage of gold deposition occurred early in the paragenesis of quartz-pyrite-stibnite-realgar-orpiment veins, with the deposition of fine-grained, auriferous, sooty arsenical pyrite and minor arsenopyrite. Low and falling pressures throughout the hydrothermal history are suggested by the ubiquitous presence of low-density, CO_2-bearing vapor-phase fluid inclusions coexisting with liquids ranging from greater than 360°C and 46.1 wt percent NaCl equiv in porphyry-type veins, to ~200°C and 3.6 wt percent NaCl equiv (average) in epithermal veins. Pressures unlikely exceeded 100 bars and are estimated to have been as low as 15 bars during the epithermal stage. Gold deposition may have been assisted by phase separation, but codeposition as solid solution in arsenical pyrite suggests that pyrite precipitation in response to rapidly falling temperatures may have been the principal depositional mechanism.

The Sari Gunay gold deposit and its generative volcanic complex are located within the Takab belt, a north-northwest–trending structural corridor that appears to have localized other middle Miocene magmatic systems as far as Zarshuran (approximately 190 km to the north-northwest). Zarshuran is the only other significant epithermal gold deposit in this region, and although its mineralization is dominantly sediment hosted, the deposit also appears to be related to middle Miocene intrusive activity. The Takab belt may thus represent a distinct metallotect, slightly younger than, and displaced to the southwest from, the earlier middle Miocene porphyry belt hosted by the Urumieh-Dokhtar volcanic arc.

The mildly alkaline (high K) geochemical characteristics of the Takab belt igneous rocks are also distinct from the normal calc-alkaline compositions of the Urumieh-Dokhtar rocks, suggesting an association with collisional rather than normal subduction tectonics. Although the timing and architecture of Neo-Tethys ocean basin closure in Iran is poorly constrained, cessation of voluminous calc-alkaline magmatism in the Eocene-Miocene Urumieh-Dokhtar arc and a rapid switch to

increasingly alkaline magmatism from the middle Miocene is consistent with tectonic models that call for final ocean closure at this time. A collisional or transitional tectonic setting for the Sari Gunay gold deposit is similar to that proposed for alkalic-type epithermal systems worldwide.

Acknowledgments

This project would not have been possible without the generous support of Rio Tinto Mining and Exploration Ltd., and particular thanks are due to J. Bartram and N. McLaurin of the Bristol office, the late R. Andrew of the Melbourne office, and H. Iranmanesh, M. Samimi Namin, H. Martin, S. Martin, F. Parvinpour, H. Asadi, E. Heidari, and A. Raddock of the Tehran office. M. Mohajjel, M. Momenzadeh, A. Hushmand-Zadeh, M. Ghorbani, B. Samani, and F. Moore are thanked for sharing their knowledge of Iranian geology and extending warm hospitality during field visits. *Economic Geology* reviewers J. Dilles and A. Longo are thanked for constructive reviews of the manuscript. This research was supported by a Discovery grant to Richards from the Natural Sciences and Engineering Research Council of Canada.

June 19, November 13, 2006

REFERENCES

Agard, P., Omrani, J., Jolivet, L., and Mouthereau, F., 2005, Convergence history across Zagros (Iran): Constraints from collisional and earlier deformation: International Journal of Earth Sciences, v. 94, p. 401–419.

Alavi, M., 1994, Tectonics of the Zagros orogenic belt of Iran: New data and interpretations: Tectonophysics, v. 229, p. 211–238.

Aldanmaz, E., 2002, Mantle source characteristics of alkali basalts and basanites in an extensional intracontinental plate setting, western Anatolia, Turkey: Implications for multi-stage melting: International Geology Review, v. 44. p. 440–457.

Asadi, H.H., 2000, The Zarshuran gold deposit model applied in a mineral exploration GIS in Iran: Unpublished Ph.D. thesis, Netherlands, Delft University of Technology, Delft, 190 p.

Asadi, H.H., Voncken, J.H.L., and Hale M., 2000a, Invisible gold at Zarshuran, Iran: Economic Geology, v. 94, p. 1367–1374.

Asadi, H.H., Voncken, J.H.L., Kühnel, R.A., and Hale M., 2000b, Petrography, mineralogy and geochemistry of the Zarshuran Carlin-like gold deposit, northwest Iran: Mineralium Deposita, v. 35, p. 656–671.

Berberian, F., and King, G.C.P., 1981, Towards a paleogeography and tectonic evolution of Iran: Canadian Journal of Earth Sciences, v. 18, p. 210–265.

Bodnar, R.J., 1993, Revised equation and table for determining the freezing point depression of H_2O-NaCl solutions: Geochimica et Cosmochimica Acta, v. 57, p. 683–684.

Bonini, M., Corti, G., Sokoutis, D., Vannucci, G., Gasperini, P., and Cloetingh, S., 2003, Insights from scaled analogue modelling into the seismotectonics of the Iranian region: Tectonophysics, v. 376, p. 137–149.

Cloos, M., Sapiie, B., van Ufford, A.Q., Weiland, R.J., Warren, P.Q., and McMahon, T.P., 2005, Collisional delamination in New Guinea: The geotectonics of subducting slab breakoff: Geological Society of America Special Paper 400, 51 p.

Cooke, D.R., and Simmons, S.F., 2000, Characteristics and genesis of epithermal gold deposits: Reviews in Economic Geology, v. 13, p. 221–244.

Daliran, F., Hofstra, A., Walther, J., and Stuben, D., 2002, Agdarreh & Zarshuran SRHDG deposits, Takab region, NW-Iran [abs.]: Geological Society of America Abstracts with Programs, v. 34, no. 6, p. 141.

Dalrymple, G.B., Lanphere, M.A., and Pringle, M.S., 1988, Correlation diagrams in $^{40}Ar/^{39}Ar$ dating: Is there a correct choice?: Geophysical Research Letters, v. 15, p. 589–591.

Davies, J.H., and von Blankenburg, F., 1995, Slab breakoff: A model of lithosphere detachment and its test in the magmatism and deformation of collisional orogens: Earth and Planetary Science Letters, v. 129, p. 85–102.

Drummond, S.E., and Ohmoto, H., 1985, Chemical evolution and mineral deposition in boiling hydrothermal systems: Economic Geology, v. 80, p. 126–147.

Elburg, M.A., and Foden, J., 1999, Geochemical response to varying tectonic settings: An example from southern Sulawesi (Indonesia): Geochimica et Cosmochimica Acta, v. 63, p. 1155–1172.

Farhoudi, G., 1978, A comparison of Zagros geology to island arcs: Journal of Geology, v. 86, p. 323–334.

Farhoudi, D., and Karig, D.E., 1977, Makran of Iran and Pakistan as an active arc system: Geology, v. 5, p. 664–668.

Fleck, R.J., Sutter, J.F., and Elliot, D.H., 1977, Interpretation of discordant $^{40}Ar/^{39}Ar$ age-spectra of Mesozoic tholeiites from Antarctica: Geochimica et Cosmochimica Acta, v. 41, p. 15–32.

Förster, H., 1978, Mesozoic-Cenozoic metallogenesis in Iran: Journal of the Geological Society [London], v. 135, p. 443–455.

Frey, F.A., Chappell, B.W., and Roy, S.D., 1978, Fractionation of rare-earth elements in the Tuolumne intrusive series, Sierra Nevada batholith, California: Geology, v. 6, p. 239–242.

Geological Survey of Iran, 1989, Geological map of Iran: Tehran, Geological Survey of Iran, 1 sheet, 1:2,500,000.

Giese, P., Makris, J., Akashe, B., Röwer, P., Letz, H., and Mostaanpour, M., 1984, The crustal structure in southern Iran derived from seismic explosion data: Neues Jahrbuch fuer Geologie und Paläontologie, Abhandlungen, v. 168, p. 230–243.

Glennie, K.W., 2000, Cretaceous tectonic evolution of Arabia's eastern plate margin: A tale of two oceans: Society for Sedimentary Geology (SEPM) Special Publication. 69, p. 9–20.

Goldstein, R.H., and Reynolds, T.J., 1994, Systematics of fluid inclusions in diagenetic materials: Society for Sedimentary Geology Short Course 31, 199 p.

Haas, J.L., 1976, Physical properties of the coexisting phases and thermochemical properties of the H_2O component in boiling NaCl solutions: U.S. Geological Survey Bulletin 1421-A, 73 p.

Hassanzadeh, J., 1993, Metallogenic and tectonomagmatic events in the SE sector of the Cenozoic active continental margin of central Iran (Shahr e Babak area, Kerman province): Unpublished Ph.D. dissertation, University of California, Los Angeles, 204 p.

Hanson, G.N., 1980, Rare earth elements in petrogenetic studies of igneous systems: Annual Review of Earth Planetary Sciences, v. 8, p. 371–406.

Harris, N.B.W., Pearce, J.A., and Tindle, A.G., 1986, Geochemical characteristics of collision-zone magmatism: Geological Society of London Special Publication 19, p. 67–81.

Hedenquist, J.W., and Daneshfar, B., 2001, Strategic prospectivity review of mineral potential: Middle East region: Tokyo, Report to Metal Mining Agency of Japan, 68 p.

Heydari, E., Hassanzadeh, J., and Ghazi, M., 2002, Permian to Triassic evolution of the Sanandaj-Sirjan province of Iran [abs.]: Geological Society of America Abstracts with Programs, v. 34, no. 6, p. 331.

Hezarkhani, A., and Williams-Jones, A.E., 1998, Controls of alteration and mineralization in the Sungun porphyry copper deposit, Iran: Evidence from fluid inclusions and stable isotopes: Economic Geology, v. 93, p. 651–670.

Hooper, R.J., Baron, I., Hatcher, R.D., and Agah, S., 1994, The development of the southern Tethyan margin in Iran after the break-up of Gondwana—implications for the Zagros hydrocarbon province: Geoscience (Geological Survey of Iran), v. 4, p. 72–85.

Ilbeyli, N., Pearce, J.A., Thirlwall, M.F., and Mitchell, J.G., 2004, Petrogenesis of collision-related plutonics in Central Anatolia, Turkey: Lithos, v. 72, p. 163–182.

Jacob, K.H., and Quittmeyer, R.L., 1979, The Makran region of Pakistan and Iran: Trench–arc system with active plate subduction, *in* Farah, A., and De Jong, K.A., eds., Geodynamics of Pakistan: Quetta, Geological Survey of Pakistan, p. 305–317.

Jensen, E.P., and Barton, M.D., 2000, Gold deposits related to alkaline magmatism: Reviews in Economic Geology, v. 13, p. 279–314.

Johnson, R.W., Mackenzie, D.E., and Smith, I.E.M., 1978, Delayed partial melting of subduction-modified mantle in Papua New Guinea: Tectonophysics, v. 46, p. 197–216.

Jugo, P.J., Luth, R.W., and Richards, J.P., 2005, An experimental study of the sulfur content in basaltic melts saturated with immiscible sulfide or sulfate liquids at 1300°C and 1.0 GPa: Journal of Petrology, v. 46, p. 783–79

Kelley, K.D., and Ludington, S., 2002, Cripple Creek and other alkaline-related gold deposits in the southern Rocky Mountains, USA: Influence of regional tectonics: Mineralium Deposita, v. 37, p. 38–60.

Kelley, K.D., Romberger, S.B., Beaty, D.W., Pontius, J.A., Snee, L.W., Stein, H.J., and Thompson, T.B., 1998, Geochemical and geochronological

constraints on the genesis of Au-Te deposits at Cripple Creek, Colorado: Economic Geology, v. 93, p. 981–1012.
Lang, J.R., and Titley, S.R., 1998, Isotopic and geochemical characteristics of Laramide magmatic systems in Arizona and implications for the genesis of porphyry copper deposits: Economic Geology, v. 93, p. 138–170.
Lanphere, M.A., and Dalrymple, G.B., 1976, Identification of excess ^{40}Ar by the $^{40}Ar/^{39}Ar$ age spectrum technique: Earth and Planetary Science Letters, v. 32, p. 141–148.
Le Maitre, R.W., ed., 1989, A classification of igneous rocks and glossary of terms: Oxford, Blackwell Scientific Publications, 193 p.
Ludwig, K.R., 2003, Isoplot 3.09—a geochronological toolkit for Microsoft Excel: Berkeley Geochronology Center Special Publication 4, 70 p.
McCall, G.J.H., and Kidd, R.G.W., 1982, The Makran, southeastern Iran: the anatomy of a convergent plate margin active from Cretaceous to Present: Geological Society of London Special Publication 10, p. 387–397.
McInnes, B.I.A., Evans, N.J., Belousova, E., Griffin, W.T., and Andrew, R.L., 2003, Timing of mineralization and exhumation processes at the Sar Cheshmeh and Meiduk porphyry Cu deposits, Kerman belt, Iran, *in* Eliopoulos et al., eds., Mineral exploration and sustainable development: Rotterdam, Millpress, p. 1197–1200.
McQuarrie, N., Stock, J.M., Verdel, C., and Wernicke, B.P., 2003, Cenozoic evolution of Neotethys and implications for the causes of plate motions: Geophysical Research Letters, v. 30, no. 20, 2036, 4 p., doi: 10.1029/2003GL017992
Mehrabi, B., Yardley, B.W.D., and Cann, J.R., 1999, Sediment-hosted disseminated gold mineralization at Zarshuran, NW Iran: Mineralium Deposita, v. 34, p. 673–696.
Mohajjel, M., Fergusson, C.L., and Sahandi, M.R., 2003, Cretaceous-Tertiary convergence and continental collision, Sanandaj-Sirjan zone, western Iran: Journal of Asian Earth Sciences, v. 21, p. 397–412.
Mungall, J.E., 2002, Roasting the mantle: Slab melting and the genesis of major Au and Au-rich Cu deposits: Geology, v. 30, p. 915–918.
Muntean, J.L., and Einaudi, M.T., 2000, Porphyry gold deposits of the Refugio district, Maricunga belt, northern Chile: Economic Geology, v. 95, p. 1445–1472.
Paquette, J.-L., Ménot, R.-P., Pin, C., and Orsini, J.-B., 2003, Episodic and short-lived granitic pulses in a post-collisional setting: Evidence from precise U-Pb zircon dating through a crustal cross-section in Corsica: Chemical Geology, v. 198, p. 1–20.
Pearce, J.A., Bender, J.F., De Long, S.E., Kidd, W.S.F., Low, P.J., Güner, Y., Saroglu, F., Yilmaz, Y., Moorbath, S., and Mitchell, J.G., 1990, Genesis of collision volcanism in eastern Anatolia, Turkey: Journal of Volcanology and Geothermal Research, v. 44, p. 189–229.
Reed, M.H., and Spycher, N.F., 1985, Boiling, cooling, and oxidation in epithermal systems: A numerical modeling approach: Reviews in Economic Geology, v. 2, p. 249–272.
Regard, V., Faccenna, C., Martinod, J., Bellier, O., and Thomas, J.-C., 2003, From subduction to collision: Control of deep processes on the evolution of convergent plate boundary: Journal of Geophysical Research, v. 108, no. B4, 16 p., doi: 10.1029/2002JB001943
Regard, V., Bellier, O., Thomas, J.-C., Bourlès, D., Bonnet, S., Abbassi, M.R., Braucher, R., Mercier, J., Shabanian, E., Soleymani, S., and Feghhi, Kh., 2005, Cumulative right-lateral fault slip rate across the Zagros-Makran transfer zone: Role of the Minab-Zendan fault system in accommodating Arabia-Eurasia convergence in southeast Iran: Geophysical Journal International, v. 162, p. 177–203.
Renne, P.R., Swisher, C.C., Deino, A.L., Karner, D.B., Owens, T.L., and DePaolo, D.J., 1998, Intercalibration of standards, absolute ages and uncertainties in $^{40}Ar/^{39}Ar$ dating: Chemical Geology, v. 145, p. 117–152.
Richards, J.P., 1995, Alkalic-type epithermal gold deposits—a review: Mineralogical Association of Canada Short Course Series, v. 23, p. 367–400.
——1997, Controls on scale of Porgera-type porphyry/epithermal gold deposits associated with mafic alkalic magmatism: Institution of Mining and Metallurgy Transactions, v. 106, p. B1–B8.
——2003a, Metallogeny of the Neo-Tethys arc in central Iran [ext. abs.], *in* Eliopoulos et al., eds., Mineral exploration and sustainable development: Rotterdam, Millpress, p. 1237–1239.
——2003b, Tectono-magmatic precursors for porphyry Cu-(Mo-Au) deposit formation: Economic Geology, v. 98, p. 1515–1533.
——2005, Cumulative factors in the generation of giant calc-alkaline porphyry Cu deposits, *in* Porter, T.M., ed., Super porphyry copper and gold deposits: A global perspective: Linden Park, South Australia, PGC Publishing, v. 1, p. 7–25.
Richards, J.P., and Kerrich, R., 1993, The Porgera gold mine, Papua New Guinea: Magmatic-hydrothermal to epithermal evolution of an alkalic-type precious metal deposit: Economic Geology, v. 88, p. 1017–1052.
Roedder, E., 1984, Fluid inclusions: Reviews in Mineralogy, v. 12, 644 p.
Sandeman, H.A., Archibald, D.A., Grant, J.W., Villeneuve, M.E., and Ford, F.D., 1999, Characterisation of the chemical composition and ^{40}Ar-^{39}Ar systematics of intralaboratory standard MAC-83 biotite: Geological Survey of Canada Current Research 1999-F, p. 13–26.
Seward, T.M., 1989, The hydrothermal chemistry of gold and its implications for ore formation: Boiling and conductive cooling as examples: Economic Geology Monograph 6, p. 398–404.
Shahabpour, J., 2005, Tectonic evolution of the orogenic belt in the region located between Kerman and Neyriz: Journal of Asian Earth Sciences, v. 24, p. 405–417.
Shamanian, G.H., Hedenquist, J.W., Hattori, K.H., and Hassanzadeh, J., 2004, The Gandy and Abolhassani epithermal prospects in the Alborz magmatic arc, Semnan Province, northern Iran: Economic Geology, v. 99, p. 691–712.
Snyder, D.B., and Baranzangi, M., 1986, Deep crustal structure and flexure of the Arabian plate beneath the Zagros collisional mountain belt as inferred from gravity observations: Tectonics, v. 5, p. 361–373.
Solomon, M., 1990, Subduction, arc reversal, and the origin of porphyry copper-gold deposits in island arcs: Geology, v. 18, p. 630–633.
Spooner, E.T.C., 1993, Magmatic sulphide/volatile interaction as a mechanism for producing chalcophile element enriched, Archean Au-quartz, epithermal Au-Ag and Au skarn hydrothermal ore fluids: Ore Geology Reviews, v. 7, p. 359–379.
Stampfli, G.M., 2000, Tethyan oceans: Geological Society of London Special Publication 173, p. 1–23.
Sterner, S.M., Hall, D.L., and Bodnar, R.J., 1988, Synthetic fluid inclusions. V. Solubility relations in the system NaCl-KCl-H_2O under vapor-saturated conditions: Geochimica et Cosmochimica Acta, v. 52, p. 989–1005.
Stoneley, R., 1974, Evolution of the continental margins bounding a former southern Tethys, *in* Burk, C.A., and Drake, C.L., eds., The geology of continental margins: New York, Springer-Verlag, p. 873–903.
——1981, The geology of the Kuh-e Dalneshin area of southern Iran, and its bearing on the evolution of southern Tethys: Journal of the Geological Society [London], v. 138, p. 509–526.
Sun, S.-S., and McDonough, W.F., 1989, Chemical and isotopic systematics of oceanic basalts: Implications for mantle composition and processes: Geological Society of London Special Publication 42, p. 313–345.
Tosdal, R.M., and Richards, J.P., 2001, Magmatic and structural controls on the development of porphyry Cu ± Mo ± Au deposits: Reviews in Economic Geology, v. 14, 157–181.
Wyborn, D., and Sun, S.-S., 1994, Sulphur-undersaturated magmatism—a key factor for generating magma-related copper-gold deposits: Australian Geological Survey Organisation (AGSO) Research Newsletter 21, p. 7–8.
Yilmaz, Y., Güner, Y., and Saroglu, F., 1998, Geology of the Quaternary volcanic centres of the East Anatolia: Journal of Volcanology and Geothermal Research, v. 85, p. 173–210.
Zarasvandi, A., Liaghat, S., and Zentilli, K., 2005, Porphyry copper deposits of the Urumieh-Dokhtar magmatic arc, Iran, *in* Porter, T.M., ed., Super porphyry copper and gold deposits: A global perspective, v. 2: Linden Park, South Australia,PGC Publishing, p. 441–452.

TABLE A1. Major and Trace Element Analyses of Igneous Rocks from the Urumieh-Dokhtar Belt, Iran

Sample no.	IR1	IR2	IR4	IR5	IR6	IR7	IR8	IR10
Location (see Table 1 for UTM coordinates)	Sahand monogenetic vent	Sahand basaltic andesite	Sar Cheshmeh: Kuh-e-Ghool dacite dome	Sar Cheshmeh: Sar Kuh andesitic dike	Sar Cheshmeh: Sar Kuh granodiorite	Sar Cheshmeh: Altered dacitic volcanic rocks	Sar Cheshmeh: Trachybasaltic volcanic rocks	Sar Cheshmeh: Vesicular trachytic lava
Total alkali-silica lithology	Rhyolite (med K)	Basaltic andesite (med K)	Dacite (med K)	Andesite (med K)	Dacite (granodiorite) (hi K)	Dacite (med K)	Potassic trachybasalt (hi K)	Trachyte (hi K)
Weight %								
SiO_2	69.88	54.24	65.58	60.04	66.24	67.83	48.53	60.66
Al_2O_3	15.55	18.15	16.77	17.05	15.22	14.11	18.22	16.07
CaO	2.85	8.06	4.16	5.87	4.10	1.44	7.67	3.65
MgO	0.77	3.92	1.05	1.87	1.76	1.87	4.07	0.76
Na_2O	4.60	2.94	4.93	4.81	3.63	6.13	2.75	3.00
K_2O	2.27	1.14	2.43	1.51	3.09	1.04	3.54	5.76
$Fe_2O_3^T$	1.84	8.27	3.12	6.65	4.76	4.77	10.74	4.78
MnO	0.03	0.14	0.05	0.12	0.08	0.06	0.16	0.07
TiO_2	0.31	0.77	0.41	0.70	0.52	0.73	0.96	0.64
P_2O_5	0.12	0.20	0.18	0.28	0.08	0.22	0.34	0.26
LOI	1.70	0.95	0.95	0.50	0.65	1.55	2.75	3.20
Sum	99.90	98.78	99.63	99.39	100.10	99.75	99.72	98.85
Ppm								
Cs	0.39	0.48	0.71	0.98	0.70	0.11	0.43	15.76
Tl	0.307	0.088	0.221	0.196	0.317	0.119	0.239	0.388
Rb	23.8	13.5	36.0	27.3	33.7	13.0	53.0	266.6
Ba	235	86	323	23	157	66	115	330
Th	3.0	0.7	4.6	1.3	3.9	3.4	1.0	22.1
U	2.89	1.09	1.77	3.31	1.73	1.59	2.34	10.92
Nb	13.5	5.1	4.4	5.2	5.1	8.6	4.4	17.6
Ta	0.92	0.31	0.31	0.38	0.40	0.46	0.27	1.11
La	8.1	1.7	14.8	4.2	5.4	7.0	2.0	23.4
Ce	36.8	18.7	37.0	8.0	22.9	26.4	13.7	75.4
Pb	10.5	3.7	11.5	6.6	4.7	2.5	12.3	16.0
Pr	1.21	0.44	3.16	0.94	1.65	2.52	0.45	5.59
Mo	2.94	1.09	0.64	0.81	2.05	1.46	0.99	4.45
Sr	182	121	531	67	93	60	143	136
Nd	3.7	1.6	10.9	3.4	6.3	10.3	1.8	21.0
Zr	63.5	90.5	41.9	97.4	8.5	207.9	86.3	371.9
Hf	2.09	2.68	1.86	4.03	0.48	4.83	3.01	9.07
Sm	0.63	0.45	1.94	1.09	1.54	2.76	0.34	4.27
Eu	0.17	0.10	0.47	0.29	0.32	0.59	0.12	0.65
Gd	0.56	0.33	1.18	0.85	1.60	2.73	0.37	3.75
Tb	0.05	0.04	0.10	0.10	0.24	0.38	0.05	0.53
Dy	0.25	0.27	0.57	0.57	1.64	2.65	0.27	3.51
Li	14.4	6.2	13.2	11.8	9.6	13.8	15.0	13.5
Y	1.63	1.50	4.03	3.13	8.27	15.40	1.24	17.96
Ho	0.04	0.06	0.10	0.13	0.33	0.47	0.05	0.68
Er	0.18	0.19	0.28	0.43	1.06	1.51	0.14	2.25
Tm	0.02	0.02	0.03	0.07	0.18	0.27	0.02	0.37
Yb	<0.05	0.12	0.17	0.47	1.05	1.58	0.10	2.45
Lu	0.01	0.03	0.03	0.07	0.16	0.22	0.02	0.40
Be								4.71
Sc	4.59	17.63	5.80	11.50	12.17	19.23	22.44	12.38
V	26.61	183.89	62.82	78.99	100.08	107.42	253.53	67.10
Bi	0.13	0.04	0.04	0.09	0.08	0.06	0.08	0.03
P	592.36	1035.03	897.29	1323.40	414.00	1017.89	1739.54	1114.26
Ti	1877.65	5495.80	2559.98	4626.58	3380.78	4782.51	6836.50	3720.90
Cr	11.08	44.77	11.93	28.35	27.60	21.58	51.41	16.73
Co	4.84	29.97	8.41	13.14	13.39	12.32	44.00	9.36
Ni	4.43	14.74	3.16	2.54	3.39	2.71	24.88	2.88
Cu	17.65	44.42	45.65	23.19	55.45	3.51	12.08	30.14
Zn	43.09	72.60	57.02	71.51	40.72	42.10	91.79	56.54
As	0.83	1.46	2.43	10.85	4.79	7.81	10.60	10.90
Mo	2.82	1.25	0.70	0.83	1.91	1.19	1.39	4.24
Ag			0.09	0.22				
Cd	0.08	0.21		0.11	0.07	0.14	0.07	0.15
Sn	0.99	1.38	1.08	1.96	2.03	2.40	2.42	2.33
Sb	0.13	0.24	0.20	0.75	0.31	0.15	0.31	0.79
W	1.04	0.51	0.84	12.54	0.60	1.05	1.59	5.51

TABLE A1.

Sample no.	IR11	IR14	IR15	IR16	IR17	IR18	IR19	IR20	IR21	IR50
Location (see Table 1 for UTM coordinates)	Sar Cheshmeh: Oxidized rhyolitic lava	Abdar trachy-diorite	Meiduk late sho-shonite dike	Meiduk area latite volcanic rocks	Meiduk area andesite dike	Meiduk area andesite dike	Meiduk area andesite volcanic rocks	Iju area dacite dike	Iju area latite volcanic rocks	Dehgolan area 1
Total alkali-silica lithology	Rhyolite (hi K)	Benmoreite (med K)	Shoshonite (hi K)	Latite (hi K)	Andesite (med K)	Dacite (med K)	Andesite (med K)	Dacite (med K)	Benmoreite (med K)	Trachyte (hi K)
Weight %										
SiO_2	67.39	60.38	54.95	55.64	59.13	62.98	56.21	63.60	55.80	64.78
Al_2O_3	14.47	16.00	13.44	17.89	17.63	16.74	16.52	16.32	16.97	14.74
CaO	1.13	5.89	6.98	3.99	6.29	5.19	7.75	4.96	7.23	2.84
MgO	0.45	2.77	5.24	1.44	3.06	1.45	3.83	1.60	1.92	2.46
Na_2O	3.29	4.44	3.27	3.52	3.63	4.58	3.07	4.22	4.09	4.07
K_2O	5.84	2.43	2.70	6.72	1.66	2.09	1.73	1.98	1.82	5.28
$Fe_2O_3^T$	4.09	5.22	9.26	5.37	6.06	4.43	7.67	3.80	5.83	3.24
MnO	0.02	0.10	0.13	0.13	0.12	0.08	0.14	0.06	0.25	0.03
TiO_2	0.53	0.58	0.97	0.74	0.54	0.60	0.91	0.50	0.55	0.63
P_2O_5	0.17	0.29	0.58	0.41	0.18	0.26	0.40	0.19	0.23	0.57
LOI	1.25	1.15	1.65	3.45	1.65	1.10	1.45	2.40	3.45	1.23
Sum	98.63	99.25	99.20	99.29	100.00	99.51	99.70	99.62	98.14	99.87
Ppm										
Cs	7.14	1.27	1.78	2.24	0.81	0.54	0.16	0.21	0.37	13.03
Tl	1.413	0.371	0.139	0.541	0.127	0.257	0.090	0.181	0.163	>2
Rb	288.1	36.5	27.8	148.5	19.6	24.3	16.3	24.6	25.5	>150
Ba	424	348	698	96	39	47	141	182	117	>1400
Th	46.2	7.0	3.4	8.3	0.7	1.0	1.9	2.7	1.3	47.7
U	12.60	2.39	1.38	7.53	0.66	1.57	1.00	1.67	1.36	12.31
Nb	19.3	7.6	16.0	11.9	2.5	6.1	12.6	5.6	2.8	18.4
Ta	1.24	0.49	0.81	0.66	0.20	0.39	0.52	0.32	0.20	1.12
La	37.7	18.7	16.7	7.0	2.4	2.7	10.0	8.7	4.0	64.1
Ce	82.5	56.3	38.2	59.5	20.8	26.9	32.8	29.6	19.3	136.4
Pb	20.1	11.4	5.2	15.8	3.0	5.8	6.6	8.6	6.7	>40
Pr	8.52	4.01	3.87	1.85	0.64	0.74	2.78	1.83	1.03	16.25
Mo	5.30	1.40	0.99	2.33	0.96	0.47	2.10	0.42	1.41	1.35
Sr	231	554	526	176	159	247	407	430	237	719
Nd	31.3	14.5	15.5	7.2	2.6	3.0	11.2	7.3	4.0	67.7
Zr	425.8	30.0	101.5	202.3	69.0	125.4	239.1	65.2	85.2	302.5
Hf	11.52	1.40	3.18	5.28	2.29	3.62	4.56	1.99	2.49	7.50
Sm	6.18	2.41	2.69	1.62	0.71	0.64	2.25	1.26	0.93	11.46
Eu	0.79	0.64	0.69	0.35	0.19	0.17	0.63	0.36	0.27	2.27
Gd	5.64	1.69	2.26	1.60	0.65	0.71	2.25	1.02	0.96	6.55
Tb	0.81	0.21	0.24	0.18	0.07	0.06	0.30	0.10	0.13	0.71
Dy	5.27	1.10	1.31	1.20	0.48	0.39	1.80	0.67	0.80	3.24
Li	10.6	8.2	7.5	16.0	8.9	7.1	12.5	11.1	7.1	20
Y	26.42	5.93	6.97	6.51	2.73	2.52	12.78	4.79	4.32	15.09
Ho	1.04	0.20	0.24	0.25	0.10	0.06	0.33	0.12	0.16	0.54
Er	3.46	0.57	0.73	0.77	0.29	0.16	1.05	0.30	0.45	1.36
Tm	0.54	0.09	0.12	0.13	0.07	0.02	0.16	0.04	0.06	0.18
Yb	3.68	0.39	0.60	0.82	0.36	0.14	1.03	0.25	0.33	1.18
Lu	0.60	0.06	0.09	0.13	0.04	0.01	0.14	0.04	0.04	0.17
Be	4.80			4.31						
Sc	11.59	9.27	15.88	16.95	10.51	7.47	24.23	8.01	13.73	
V	51.34	111.26	164.56	99.52	120.17	75.43	172.91	78.61	147.12	
Bi	0.02	0.09	0.04	0.03	0.03	0.06	0.03	0.07	0.05	
P	777.28	1342.32	2884.37	1732.62	799.30	1180.04	1830.71	859.87	1055.28	
Ti	3312.53	3720.99	7231.94	4358.86	3284.68	3713.59	5817.10	3095.37	3320.57	
Cr	14.62	38.72	387.86	20.91	35.54	18.23	105.46	30.45	50.19	
Co	4.61	18.33	39.17	11.23	18.96	11.76	26.01	11.94	22.13	
Ni	1.13	18.57	135.36	4.46	13.05	4.83	27.62	14.29	24.94	
Cu	33.04	58.05	99.39	74.72	54.84	25.61	18.45	181.17	5.74	
Zn	29.98	61.59	74.55	65.42	56.60	62.51	71.77	59.53	70.52	
As	23.19	2.69	2.08	2.96	3.69	1.26	2.39	0.84	12.85	
Mo	5.31	1.66	1.15	2.22	0.97	0.43	1.44	0.41	1.25	
Ag		0.05		0.06		0.15	0.37	0.15	0.16	
Cd	0.10	0.12	0.15		0.13	0.15	0.05		0.08	
Sn	2.86	1.17	2.54	2.73	0.71	0.84	1.56	0.89	0.82	
Sb	1.39	0.36	0.20	0.48	0.13	0.47	0.18	0.73	0.94	
W	4.65	0.95	0.42	2.17	0.28	0.28	0.54	0.81	2.93	

(Cont.)

IR51	IR52	IR53	IR54	IR55	IR61	IR62	IR63	IR64	IR65
Dehgolan area 1	Dehgolan area 1	Dehgolan area 1	Dehgolan area 1	Dehgolan area 1	W Razan area 1	W Razan area 1	W Razan area 1	W Razan area 2	Zar Shuran
Rhyolite (hi K)	Dacite (hi K)	Latite (hi K)	Rhyolite (hi K)	Trachyte (hi K)	Basalt (gabbro; med K)	Basaltic andesite (diorite; med K)	Shoshonite (diorite; hi K)	Dacite (diorite; med K)	Andesite (hi K)
69.50	65.05	59.99	68.47	61.67	50.99	54.38	53.99	63.16	58.00
16.58	16.41	16.03	15.94	16.61	19.62	18.61	18.71	16.44	16.51
1.71	3.94	5.31	1.85	4.12	12.32	7.50	7.11	6.36	6.40
0.50	1.83	4.33	0.20	1.47	4.58	3.18	3.70	2.25	2.60
4.30	4.22	3.84	4.49	4.54	3.69	3.35	3.99	4.70	3.38
3.96	3.05	2.76	4.49	2.85	0.26	1.79	2.16	0.42	2.40
0.95	3.10	4.13	2.10	3.02	6.00	9.26	8.37	5.30	6.64
0.00	0.03	0.07	0.03	0.03	0.07	0.33	0.15	0.05	0.10
0.30	0.50	0.58	0.33	0.41	1.37	0.97	0.94	0.71	0.81
0.15	0.20	0.22	0.14	0.20	0.25	0.17	0.18	0.12	0.12
1.70	2.12	2.50	1.53	4.57	1.36	1.38	1.54	1.04	3.52
99.68	100.44	99.74	99.57	99.49	100.50	100.92	100.84	100.56	100.48
12.85	8.00	5.85	9.59	9.08	0.10	3.40	0.82	0.19	2.73
>2	0.710	0.640	1.360	0.920	0.010	0.190	0.160	0.050	0.560
147.1	77.9	91.8	>150	93.5	3.7	70.6	59.7	12.7	70.4
>1400	1185	860	1264	1197	113	372	288	170	450
20.7	12.2	13.1	29.5	20.4	1.5	2.9	3.2	7.7	7.6
7.92	4.60	4.79	8.03	5.34	0.44	0.87	0.92	2.20	2.73
15.0	11.3	12.3	19.9	15.0	13.2	10.0	11.2	11.6	10.6
1.11	0.76	0.79	1.30	0.99	0.81	0.63	0.70	0.80	0.95
38.4	25.1	27.2	33.1	49.3	7.8	15.4	13.7	19.7	19.2
68.4	48.0	50.7	60.6	88.6	17.6	30.6	30.0	40.3	39.8
>40	29.6	26.1	34.8	39.6	1.1	5.1	2.1	3.3	17.6
6.94	5.33	5.47	7.28	8.94	2.38	3.69	3.74	4.70	4.76
0.91	0.86	2.12	1.25	1.48	0.30	1.11	1.42	1.06	2.04
592	517	535	562	816	386	352	320	252	202
23.7	19.4	19.8	27.1	30.9	11.1	15.3	15.6	18.7	18.9
127.3	159.3	164.7	221.3	147.7	76.3	123.5	141.4	83.2	139.4
3.40	4.10	4.10	6.00	3.70	2.00	3.10	3.40	2.50	3.80
3.64	3.36	3.41	4.30	4.70	2.79	3.36	3.52	3.93	4.16
0.97	0.90	0.92	1.04	1.20	0.97	1.09	1.00	0.89	1.00
2.60	2.71	2.79	2.76	3.42	3.12	3.60	3.67	4.04	4.33
0.34	0.38	0.39	0.38	0.46	0.50	0.59	0.60	0.67	0.73
1.77	1.99	2.12	2.03	2.38	3.05	3.66	3.72	4.26	4.52
10	9	12	28	26	1	21	15	2	30
8.95	10.54	11.08	11.04	12.26	16.24	20.76	20.76	24.54	25.93
0.31	0.38	0.40	0.37	0.43	0.62	0.78	0.78	0.89	0.94
0.84	1.03	1.09	1.06	1.16	1.79	2.31	2.28	2.66	2.84
0.12	0.15	0.16	0.16	0.17	0.26	0.34	0.34	0.40	0.42
0.76	0.96	1.01	1.04	1.07	1.62	2.24	2.23	2.66	2.78
0.11	0.14	0.15	0.16	0.15	0.24	0.35	0.34	0.40	0.42

TABLE A1. *(Cont.)*

Sample no.	IR66	IR67	IR68	IR69	IR70	IR71	IR72	IR73	IR74	IR75	IR76
Location (see Table 1 for UTM coordinates)	Zar Shuran	Zar Shuran	Zar Shuran	Badamlu	Badamlu	Badamlu	Badamlu	Shebe Jazireh Shahi	Shebe Jazireh Shahi	Sahand volcano	Sahand volcano
Total alkali-silica lithology	Latite (hi K)	Andesite (microdiorite; med K)	Andesite (hi K)	Trachyte (hi K)	Shoshonite (hi K)	Trachyte (granite; hi K)	Trachyte (granite; hi K)	Basanite (hi K)	Basanite (hi K)	Dacite (med K)	Dacite (med K)
Weight %											
SiO_2	56.99	60.25	57.44	63.06	49.68	60.17	58.43	45.31	44.27	65.65	66.23
Al_2O_3	17.89	16.12	17.05	15.89	17.10	17.62	19.66	12.00	13.50	16.41	16.32
CaO	7.66	2.06	7.44	5.25	7.91	3.52	4.23	11.70	12.12	4.48	4.02
MgO	1.12	4.90	1.48	0.89	3.64	1.99	1.53	8.10	7.44	1.48	1.18
Na_2O	3.82	3.65	3.03	4.68	3.36	4.95	4.90	1.75	2.10	4.03	4.71
K_2O	2.36	1.48	2.55	3.06	3.13	5.06	6.04	6.26	5.95	2.27	2.37
$Fe_2O_3^T$	6.00	6.83	6.30	3.52	9.34	4.80	3.80	9.88	10.09	3.20	3.10
MnO	0.14	0.03	0.07	0.05	0.17	0.08	0.07	0.18	0.17	0.05	0.05
TiO_2	0.75	0.72	0.74	0.56	0.98	0.60	0.63	1.01	1.17	0.41	0.40
P_2O_5	0.18	0.12	0.14	0.21	0.34	0.35	0.31	1.37	1.18	0.16	0.16
LOI	3.56	4.48	3.40	2.47	4.96	1.01	0.57	2.13	1.51	2.18	0.54
Sum	100.47	100.62	99.66	99.64	100.61	100.14	100.18	99.68	99.48	100.34	99.09
Ppm											
Cs	1.76	1.61	4.94	1.49	1.83	6.46	3.41	12.70	10.12	3.48	1.48
Tl	0.260	0.250	0.520	0.160	0.120	0.430	0.250	0.230	0.110	0.400	0.240
Rb	68.1	33.4	83.9	61.8	67.2	>150	139.7	>150	>150	54.6	54.6
Ba	445	329	480	1139	517	615	655	>1400	>1400	606	665
Th	5.7	9.3	7.9	6.6	3.7	19.7	5.2	23.8	18.9	6.4	7.9
U	2.21	5.68	3.14	2.03	0.88	4.26	1.72	7.22	4.44	2.89	2.79
Nb	13.8	11.6	12.8	16.5	15.3	32.3	16.1	34.6	36.5	10.3	10.7
Ta	1.06	1.04	1.07	1.22	1.09	2.33	1.09	1.63	1.71	0.96	0.94
La	18.4	36.7	17.8	32.2	19.6	33.1	18.8	83.9	66.8	16.3	24.1
Ce	38.0	68.7	36.6	58.2	39.5	60.2	33.7	177.0	137.4	27.9	42.7
Pb	12.6	4.4	12.8	20.8	3.3	16.6	19.8	34.0	>40	14.5	14.5
Pr	4.50	7.20	4.35	6.08	4.87	6.37	3.69	20.72	15.92	3.05	4.41
Mo	1.56	1.05	2.12	1.23	0.72	3.26	2.41	1.44	3.00	2.36	1.14
Sr	269	142	214	993	638	630	646	1194	1059	453	423
Nd	17.9	26.7	16.9	21.6	20.3	22.6	13.4	82.1	62.5	10.9	15.3
Zr	161.6	151.1	153.8	106.5	148.7	85.8	61.8	386.2	335.5	92.4	130.8
Hf	4.00	4.10	4.00	2.70	3.50	2.50	1.50	8.90	7.30	2.40	3.20
Sm	3.81	5.61	3.65	3.26	4.30	3.88	2.43	16.28	12.32	1.90	2.54
Eu	1.00	1.01	0.90	1.03	1.29	0.86	0.89	3.67	2.97	0.54	0.69
Gd	3.86	5.93	3.78	2.30	4.23	3.24	2.11	13.73	10.56	1.51	1.98
Tb	0.63	1.03	0.63	0.29	0.66	0.50	0.31	1.80	1.40	0.21	0.27
Dy	3.90	6.66	3.89	1.54	3.90	2.92	1.84	8.90	7.05	1.11	1.40
Li	9	43	29	13	18	21	25	15	11	17	17
Y	21.61	36.30	21.73	7.70	20.84	16.70	10.09	41.03	32.24	5.75	7.21
Ho	0.80	1.41	0.80	0.28	0.78	0.60	0.37	1.51	1.20	0.21	0.26
Er	2.36	4.20	2.39	0.77	2.26	1.80	1.08	3.73	3.01	0.57	0.71
Tm	0.35	0.61	0.35	0.10	0.32	0.27	0.16	0.48	0.37	0.08	0.10
Yb	2.29	3.92	2.29	0.70	2.08	1.88	1.05	2.98	2.32	0.53	0.64
Lu	0.34	0.59	0.34	0.10	0.30	0.28	0.16	0.41	0.31	0.08	0.09
Be											
Sc											
V											
Bi											
P											
Ti											
Cr											
Co											
Ni											
Cu											
Zn											
As											
Mo											
Ag											
Cd											
Sn											
Sb											
W											

Notes: hi K = high K, med K = medium K; samples IR1–IR21 analyzed by XRAL Laboratories, Toronto, Ontario, Canada (XRF analysis of major elements), and Dept. Geological Sciences, University of Saskatchewan, Saskatoon, Saskatchewan, Canada (ICP-MS analysis of trace elements; samples IR50–IR76 analyzed by GEOLABS Geoscience Laboratories, Sudbury, Ontario, Canada (XRF for major elements, ICP-MS and ICP-AES for trace elements)

TABLE A2. Argon Step-Heating Isotope Data for Samples from the Sari Gunay and Qezeljeh Kand Volcanic Complexes (all errors reported at 2σ)

DK3 Biotite

Laser power(%)	$^{40}Ar/^{39}Ar$	$^{38}Ar/^{39}Ar$	$^{37}Ar/^{39}Ar$	$^{36}Ar/^{39}Ar$	Ca/K	Cl/K	%^{40}Ar atm	f ^{39}Ar	$^{40}Ar^{*}/^{39}Ar_K$	Apparent age (Ma)
1.8	56.166 ± 0.020	0.125 ± 0.051	0.008 ± 0.144	0.187 ± 0.032	0.041	0.018	98.67	0.71	0.687 ± 1.437	6.93 ±14.46
2.0	17.820 ± 0.030	0.075 ± 0.048	0.005 ± 0.100	0.056 ± 0.061	0.026	0.012	93.01	1.08	1.111 ± 0.989	11.18 ± 9.92
2.2	14.564 ± 0.042	0.089 ± 0.065	0.006 ± 0.117	0.048 ± 0.071	0.028	0.015	98.45	0.92	0.169 ± 0.980	1.71 ± 9.89
2.4	11.662 ± 0.021	0.120 ± 0.055	0.005 ± 0.223	0.039 ± 0.063	0.024	0.023	100.54	1.09	–0.086 ± 0.702	–0.86 ± 7.10
2.6	3.783 ± 0.010	0.184 ± 0.018	0.001 ± 0.083	0.009 ± 0.030	0.008	0.039	70.54	5.75	1.001 ± 0.082	10.08 ± 0.83
2.8	2.807 ± 0.009	0.201 ± 0.019	0.001 ± 0.164	0.006 ± 0.038	0.005	0.043	57.02	7.57	1.084 ± 0.065	10.91 ± 0.65
3.0	2.169 ± 0.011	0.213 ± 0.012	0.000 ± 0.280	0.004 ± 0.029	0.001	0.046	44.41	11.09	1.093 ± 0.035	11.01 ± 0.35
3.2	1.916 ± 0.009	0.221 ± 0.015	0.000 ± 0.429	0.003 ± 0.056	0.003	0.047	36.94	13.93	1.103 ± 0.045	11.11 ± 0.46
3.4	1.927 ± 0.015	0.222 ± 0.019	0.001 ± 0.877	0.003 ± 0.044	0.007	0.048	37.10	14.49	1.110 ± 0.043	11.18 ± 0.43
3.6	2.108 ± 0.008	0.221 ± 0.012	0.001 ± 0.129	0.003 ± 0.052	0.003	0.048	42.79	10.43	1.086 ± 0.054	10.94 ± 0.54
3.9	2.147 ± 0.006	0.229 ± 0.018	0.001 ± 0.140	0.004 ± 0.064	0.008	0.049	44.75	8.57	1.051 ± 0.069	10.59 ± 0.69
4.4	1.667 ± 0.014	0.224 ± 0.012	0.000 ± 0.120	0.002 ± 0.026	0.000	0.048	28.29	17.99	1.099 ± 0.025	11.07 ± 0.25
5.0	2.494 ± 0.018	0.228 ± 0.016	0.002 ± 0.192	0.005 ± 0.070	0.011	0.049	54.07	5.39	0.977 ± 0.110	9.84 ± 1.11
6.0	8.544 ± 0.015	0.181 ± 0.044	0.005 ± 0.056	0.027 ± 0.078	0.026	0.037	92.42	0.98	0.494 ± 0.612	4.98 ± 6.17
Total/ Average	2.765 ± 0.002	0.213 ± 0.003	0.003 ± 0.028	0.006 ± 0.007		0.037		100.00	1.087 ± 0.013	

J = 0.005599 ± 0.000016
Volume $^{39}Ar_K$ = 1458.9 E^{-13} cm^3 NPT
Integrated age = 10.59 ± 0.27 Ma

DK20 Biotite

Laser power(%)	$^{40}Ar/^{39}Ar$	$^{38}Ar/^{39}Ar$	$^{37}Ar/^{39}Ar$	$^{36}Ar/^{39}Ar$	Ca/K	Cl/K	%^{40}Ar atm	f ^{39}Ar	$^{40}Ar^{*}/^{39}Ar_K$	Apparent age (Ma)
1.8	172.360 ± 0.044	0.218 ± 0.086	0.046 ± 0.173	0.623 ± 0.067	0.283	0.021	107.83	0.15	–12.776 ± 9.657	–134.00 ± 105.15
2.0	43.079 ± 0.019	0.176 ± 0.042	0.022 ± 0.219	0.165 ± 0.080	0.103	0.031	116.41	0.24	–6.039 ± 3.839	–62.10 ± 40.16
2.2	13.919 ± 0.016	0.189 ± 0.050	0.009 ± 0.198	0.046 ± 0.060	0.043	0.039	97.83	0.54	0.209 ± 0.786	2.11 ± 7.93
2.4	6.193 ± 0.017	0.191 ± 0.032	0.004 ± 0.128	0.019 ± 0.064	0.018	0.040	87.87	1.28	0.572 ± 0.348	5.77 ± 3.51
2.6	3.599 ± 0.011	0.194 ± 0.017	0.002 ± 0.147	0.009 ± 0.074	0.010	0.041	71.75	3.21	0.847 ± 0.202	8.55 ± 2.03
2.8	2.223 ± 0.011	0.190 ± 0.025	0.001 ± 0.165	0.004 ± 0.087	0.005	0.040	44.82	7.08	1.073 ± 0.099	10.81 ± 1.00
3.0	1.851 ± 0.012	0.192 ± 0.018	0.001 ± 0.179	0.003 ± 0.063	0.002	0.041	34.97	10.22	1.072 ± 0.050	10.80 ± 0.50
3.2	2.546 ± 0.016	0.196 ± 0.017	0.001 ± 0.062	0.005 ± 0.062	0.004	0.042	47.65	5.37	1.147 ± 0.089	11.56 ± 0.89
3.4	1.842 ± 0.009	0.197 ± 0.014	0.000 ± 0.278	0.002 ± 0.057	0.002	0.042	32.10	11.44	1.125 ± 0.042	11.34 ± 0.42
3.6	1.546 ± 0.008	0.197 ± 0.014	0.000 ± 0.194	0.001 ± 0.060	0.001	0.042	22.92	23.75	1.109 ± 0.026	11.17 ± 0.26
3.9	1.885 ± 0.015	0.197 ± 0.012	0.001 ± 0.134	0.003 ± 0.038	0.003	0.042	35.39	12.29	1.103 ± 0.039	11.12 ± 0.39
4.1	1.994 ± 0.010	0.200 ± 0.013	0.001 ± 0.063	0.003 ± 0.056	0.012	0.043	38.14	11.24	1.115 ± 0.050	11.24 ± 0.51
4.5	1.729 ± 0.010	0.215 ± 0.013	0.001 ± 0.830	0.002 ± 0.097	0.004	0.046	29.44	13.20	1.104 ± 0.060	11.13 ± 0.60
Total/ Average	2.168 ± 0.002	0.198 ± 0.003	0.003 ± 0.014	0.004 ± 0.011		0.039		100.00	1.106 ± 0.013	

J = 0.005603 ± 0.000016
Volume $^{39}Ar_K$ = 1487.67 E^{-13} cm^3 NPT
Integrated age = 10.56 ± 0.26 Ma

DK26 Sericite

Laser power(%)	$^{40}Ar/^{39}Ar$	$^{38}Ar/^{39}Ar$	$^{37}Ar/^{39}Ar$	$^{36}Ar/^{39}Ar$	Ca/K	Cl/K	%^{40}Ar atm	f ^{39}Ar	$^{40}Ar^{*}/^{39}Ar_K$	Apparent age (Ma)
0.5	13.148 ± 0.007	0.036 ± 0.045	0.007 ± 0.109	0.038 ± 0.025	0.021	0.003	82.93	2.05	2.218 ± 0.282	9.86 ± 1.25
1.0	4.625 ± 0.004	0.017 ± 0.024	0.004 ± 0.048	0.008 ± 0.025	0.012	0.000	45.51	6.71	2.493 ± 0.058	11.08 ± 0.26
1.5	3.085 ± 0.003	0.014 ± 0.017	0.003 ± 0.037	0.002 ± 0.032	0.009	–0.000	19.43	17.32	2.461 ± 0.023	10.93 ± 0.10
2.0	2.807 ± 0.003	0.013 ± 0.015	0.002 ± 0.035	0.001 ± 0.037	0.008	–0.000	11.92	20.06	2.448 ± 0.016	10.88 ± 0.07
2.5	2.761 ± 0.004	0.013 ± 0.023	0.002 ± 0.049	0.001 ± 0.051	0.007	–0.000	11.35	12.98	2.420 ± 0.023	10.75 ± 0.10
3.0	2.723 ± 0.003	0.013 ± 0.021	0.002 ± 0.069	0.001 ± 0.084	0.005	–0.000	10.11	10.08	2.418 ± 0.030	10.74 ± 0.13
3.5	2.868 ± 0.003	0.013 ± 0.022	0.001 ± 0.083	0.002 ± 0.055	0.004	–0.000	13.60	10.03	2.449 ± 0.028	10.88 ± 0.12
4.3	2.910 ± 0.004	0.014 ± 0.037	0.002 ± 0.099	0.002 ± 0.066	0.005	–0.000	15.04	6.37	2.437 ± 0.039	10.83 ± 0.17
6.0	2.953 ± 0.004	0.014 ± 0.032	0.003 ± 0.081	0.002 ± 0.055	0.007	–0.000	17.81	5.62	2.391 ± 0.038	10.62 ± 0.17
7.0	3.737 ± 0.003	0.018 ± 0.019	0.009 ± 0.025	0.005 ± 0.028	0.029	0.001	33.96	8.77	2.440 ± 0.040	10.84 ± 0.18
Total/ Average	3.281 ± 0.001	0.014 ± 0.004	0.005 ± 0.005	0.003 ± 0.006		0.000		100.00	2.427 ± 0.006	

J = 0.002470 ± 0.000018
Volume $^{39}Ar_K$ = 378.13 E^{-13} cm^3 NPT
Integrated age = 10.83 ± 0.10 Ma

TABLE A2. *(Cont.)*

DK28 Sericite

Laser power(%)	$^{40}Ar/^{39}Ar$	$^{38}Ar/^{39}Ar$	$^{37}Ar/^{39}Ar$	$^{36}Ar/^{39}Ar$	Ca/K	Cl/K	$\%^{40}Ar$ atm	f ^{39}Ar	$^{40}Ar^{*}/^{39}Ar_K$	Apparent age (Ma)
0.5	38.078 ± 0.009	0.050 ± 0.038	0.013 ± 0.061	0.125 ± 0.017	0.042	0.003	93.78	1.96	2.350 ± 0.591	10.45 ± 2.62
1.0	4.693 ± 0.005	0.018 ± 0.019	0.009 ± 0.021	0.007 ± 0.020	0.030	0.001	39.48	15.67	2.820 ± 0.045	12.53 ± 0.20
1.5	2.917 ± 0.004	0.014 ± 0.018	0.006 ± 0.022	0.001 ± 0.061	0.021	–0.000	6.41	28.00	2.709 ± 0.018	12.04 ± 0.08
1.75	2.690 ± 0.004	0.013 ± 0.019	0.005 ± 0.028	0.001 ± 0.086	0.015	–0.000	3.00	16.79	2.586 ± 0.017	11.49 ± 0.08
2.0	2.483 ± 0.003	0.013 ± 0.023	0.002 ± 0.061	0.001 ± 0.126	0.007	–0.000	1.99	9.41	2.402 ± 0.023	10.68 ± 0.10
2.5	2.442 ± 0.004	0.013 ± 0.028	0.002 ± 0.096	0.001 ± 0.148	0.005	–0.000	2.41	5.90	2.344 ± 0.034	10.42 ± 0.15
3.0	2.407 ± 0.004	0.013 ± 0.032	0.002 ± 0.101	0.001 ± 0.133	0.003	–0.000	2.09	6.03	2.317 ± 0.029	10.30 ± 0.13
4.5	2.390 ± 0.003	0.013 ± 0.024	0.001 ± 0.139	0.001 ± 0.132	0.003	–0.000	2.35	7.68	2.299 ± 0.024	10.22 ± 0.11
6.0	2.403 ± 0.004	0.014 ± 0.032	0.001 ± 0.180	0.001 ± 0.190	0.003	–0.000	1.18	5.66	2.334 ± 0.040	10.38 ± 0.18
7.0	2.465 ± 0.004	0.016 ± 0.036	0.002 ± 0.170	0.001 ± 0.155	0.003	0.000	5.61	2.89	2.267 ± 0.066	10.08 ± 0.29
Total/ Average	3.673 ± 0.001	0.015 ± 0.004	0.009 ± 0.004	0.004 ± 0.007		0.000		100.00	2.312 ± 0.008	

J = 0.002472 ± 0.000018
Volume $^{39}Ar_K$ = 385.77 E^{-13} cm^3 NPT
Integrated age = 11.38 ± 0.11 Ma

DK41 Biotite

Laser power(%)	$^{40}Ar/^{39}Ar$	$^{38}Ar/^{39}Ar$	$^{37}Ar/^{39}Ar$	$^{36}Ar/^{39}Ar$	Ca/K	Cl/K	$\%^{40}Ar$ atm	f ^{39}Ar	$^{40}Ar^{*}/^{39}Ar_K$	Apparent age (Ma)
0.5	213.471 ± 0.012	0.214 ± 0.030	0.073 ± 0.059	0.729 ± 0.019	0.212	0.013	97.87	0.69	4.607 ± 3.499	20.31 ± 15.34
1.0	30.302 ± 0.005	0.053 ± 0.029	0.037 ± 0.035	0.096 ± 0.019	0.118	0.005	90.32	3.04	2.920 ± 0.528	12.90 ± 2.32
1.5	11.531 ± 0.005	0.055 ± 0.035	0.033 ± 0.042	0.033 ± 0.032	0.103	0.008	76.54	2.70	2.677 ± 0.308	11.83 ± 1.35
1.75	6.393 ± 0.005	0.082 ± 0.021	0.022 ± 0.038	0.014 ± 0.038	0.067	0.015	59.25	3.72	2.567 ± 0.164	11.34 ± 0.72
2.0	6.540 ± 0.005	0.132 ± 0.021	0.015 ± 0.079	0.015 ± 0.039	0.044	0.026	58.55	2.93	2.666 ± 0.176	11.78 ± 0.78
2.50	5.250 ± 0.004	0.156 ± 0.013	0.012 ± 0.046	0.010 ± 0.040	0.035	0.032	51.68	4.85	2.498 ± 0.126	11.04 ± 0.55
3.0	4.595 ± 0.004	0.166 ± 0.013	0.011 ± 0.047	0.008 ± 0.040	0.035	0.034	44.07	5.52	2.530 ± 0.097	11.18 ± 0.43
3.5	3.800 ± 0.005	0.170 ± 0.012	0.014 ± 0.034	0.005 ± 0.057	0.044	0.035	30.82	6.63	2.588 ± 0.082	11.43 ± 0.36
4.25	3.450 ± 0.004	0.176 ± 0.013	0.015 ± 0.044	0.004 ± 0.077	0.046	0.037	26.37	4.85	2.488 ± 0.096	10.99 ± 0.42
5.25	3.333 ± 0.004	0.193 ± 0.010	0.026 ± 0.022	0.003 ± 0.046	0.085	0.041	24.01	11.16	2.499 ± 0.046	11.05 ± 0.20
7.0	2.869 ± 0.003	0.209 ± 0.007	0.029 ± 0.011	0.001 ± 0.028	0.094	0.045	11.66	53.91	2.513 ± 0.014	11.10 ± 0.06
Total/ Average	6.024 ± 0.001	0.181 ± 0.002	0.044 ± 0.003	0.012 ± 0.005		0.026		100.00	2.509 ± 0.018	

J = 0.002457 ± 0.000020
Volume $^{39}Ar_K$ = 179.01 E^{-13} cm3 NPT
Integrated age = 11.28 ± 0.19 Ma

DK42 Sericite

Laser power(%)	$^{40}Ar/^{39}Ar$	$^{38}Ar/^{39}Ar$	$^{37}Ar/^{39}Ar$	$^{36}Ar/^{39}Ar$	Ca/K	Cl/K	$\%^{40}Ar$ atm	f ^{39}Ar	$^{40}Ar^{*}/^{39}Ar_K$	Apparent age (Ma)
0.5	84.346 ± 0.008	0.087 ± 0.032	0.012 ± 0.088	0.275 ± 0.016	0.037	0.005	94.23	2.46	4.869 ± 1.217	21.59 ± 5.37
1.0	4.734 ± 0.004	0.016 ± 0.017	0.004 ± 0.031	0.007 ± 0.019	0.013	0.000	43.79	18.79	2.640 ± 0.043	11.74 ± 0.19
1.5	2.802 ± 0.003	0.013 ± 0.016	0.002 ± 0.041	0.001 ± 0.037	0.006	–0.000	10.41	31.35	2.488 ± 0.015	11.06 ± 0.07
2.0	2.673 ± 0.003	0.013 ± 0.019	0.002 ± 0.060	0.001 ± 0.063	0.006	–0.000	6.68	17.47	2.469 ± 0.017	10.98 ± 0.08
2.5	2.643 ± 0.003	0.013 ± 0.025	0.002 ± 0.065	0.001 ± 0.078	0.006	–0.000	6.37	12.23	2.445 ± 0.021	10.88 ± 0.09
3.0	2.713 ± 0.004	0.014 ± 0.037	0.002 ± 0.103	0.001 ± 0.106	0.006	–0.000	7.95	4.92	2.452 ± 0.045	10.91 ± 0.20
4.0	2.819 ± 0.004	0.014 ± 0.039	0.003 ± 0.100	0.002 ± 0.089	0.007	–0.000	12.58	4.29	2.418 ± 0.052	10.76 ± 0.23
5.5	2.967 ± 0.005	0.015 ± 0.041	0.003 ± 0.109	0.003 ± 0.081	0.008	–0.000	15.99	3.54	2.441 ± 0.064	10.86 ± 0.28
7.0	3.337 ± 0.004	0.017 ± 0.030	0.004 ± 0.067	0.004 ± 0.050	0.012	0.000	27.36	4.95	2.385 ± 0.055	10.61 ± 0.24
Total/ Average	5.173 ± 0.001	0.015 ± 0.004	0.005 ± 0.006	0.009 ± 0.006		0.000		100.00	2.385 ± 0.017	

J = 0.002473 ± 0.000018
Volume $^{39}Ar_K$ = 334.91 E^{-13} cm3 NPT
Integrated age = 11.36 ± 0.17 Ma

TABLE A2. *(Cont.)*

DK44 Biotite

Laser power(%)	$^{40}Ar/^{39}Ar$	$^{38}Ar/^{39}Ar$	$^{37}Ar/^{39}Ar$	$^{36}Ar/^{39}Ar$	Ca/K	Cl/K	$\%^{40}Ar$ atm	f ^{39}Ar	$^{40}Ar^*/^{39}Ar_K$	Apparent age (Ma)
0.5	70.699 ± 0.008	0.107 ± 0.031	0.020 ± 0.092	0.238 ± 0.017	0.057	0.011	96.13	0.53	2.734 ± 1.135	12.12 ± 5.01
1.0	18.903 ± 0.005	0.055 ± 0.024	0.010 ± 0.068	0.058 ± 0.019	0.028	0.007	87.01	1.46	2.434 ± 0.319	10.79 ± 1.41
1.5	5.550 ± 0.004	0.062 ± 0.016	0.007 ± 0.044	0.011 ± 0.025	0.022	0.010	55.00	3.03	2.470 ± 0.083	10.95 ± 0.37
2.0	3.515 ± 0.004	0.113 ± 0.015	0.007 ± 0.051	0.004 ± 0.063	0.023	0.023	23.68	3.38	2.646 ± 0.067	11.73 ± 0.30
2.75	3.146 ± 0.003	0.166 ± 0.009	0.006 ± 0.036	0.002 ± 0.051	0.020	0.035	14.27	5.53	2.669 ± 0.031	11.83 ± 0.14
3.75	3.009 ± 0.003	0.185 ± 0.008	0.004 ± 0.044	0.001 ± 0.051	0.012	0.039	11.52	7.30	2.637 ± 0.025	11.69 ± 0.11
4.75	2.812 ± 0.003	0.185 ± 0.008	0.003 ± 0.048	0.001 ± 0.069	0.008	0.039	6.52	7.99	2.603 ± 0.020	11.54 ± 0.09
5.75	2.811 ± 0.003	0.189 ± 0.008	0.001 ± 0.067	0.001 ± 0.064	0.004	0.040	6.70	8.38	2.598 ± 0.019	11.51 ± 0.08
6.75	2.759 ± 0.003	0.188 ± 0.007	0.001 ± 0.090	0.001 ± 0.056	0.002	0.040	5.60	21.39	2.584 ± 0.014	11.45 ± 0.06
7.75	2.764 ± 0.003	0.190 ± 0.007	0.001 ± 0.066	0.001 ± 0.050	0.002	0.040	5.93	17.05	2.579 ± 0.013	11.43 ± 0.06
8.0	2.724 ± 0.003	0.188 ± 0.007	0.001 ± 0.040	0.001 ± 0.051	0.004	0.040	5.42	23.96	2.556 ± 0.012	11.33 ± 0.05
Total/ Average	3.515 ± 0.001	0.177 ± 0.001	0.004 ± 0.005	0.003 ± 0.005		0.029		100.00	2.572 ± 0.006	

J = 0.002465 ± 0.000020
Volume $^{39}Ar_K$ = 565.58 E^{-13} cm^3 NPT
Integrated age = 11.46 ± 0.11 Ma(Inverse isochron calcuated using steps 6 through 11)

DK60 Biotite

Laser power(%)	$^{40}Ar/^{39}Ar$	$^{38}Ar/^{39}Ar$	$^{37}Ar/^{39}Ar$	$^{36}Ar/^{39}Ar$	Ca/K	Cl/K	$\%^{40}Ar$ atm	f ^{39}Ar	$^{40}Ar^*/^{39}Ar_K$	Apparent age (Ma)
2.0	202.071 ± 0.006	0.252 ± 0.051	0.042 ± 0.096	0.675 ± 0.018	0.177	0.025	98.77	0.50	2.432 ± 3.484	4.81 ± 6.89
2.3	54.997 ± 0.009	0.154 ± 0.033	0.038 ± 0.053	0.180 ± 0.020	0.165	0.024	96.30	0.84	1.978 ± 0.989	3.92 ± 1.96
2.6	38.545 ± 0.007	0.144 ± 0.021	0.029 ± 0.066	0.121 ± 0.022	0.127	0.025	92.27	1.32	2.914 ± 0.771	5.77 ± 1.52
3.0	23.136 ± 0.005	0.140 ± 0.033	0.022 ± 0.070	0.064 ± 0.023	0.100	0.026	81.47	1.87	4.197 ± 0.444	8.30 ± 0.88
3.4	16.206 ± 0.032	0.131 ± 0.028	0.012 ± 0.055	0.037 ± 0.032	0.057	0.025	67.98	5.20	5.120 ± 0.489	10.12 ± 0.97
3.8	11.027 ± 0.009	0.132 ± 0.018	0.007 ± 0.059	0.018 ± 0.027	0.037	0.026	48.86	10.70	5.576 ± 0.153	11.02 ± 0.30
4.2	9.796 ± 0.004	0.132 ± 0.011	0.008 ± 0.035	0.014 ± 0.018	0.036	0.027	41.86	20.01	5.642 ± 0.079	11.15 ± 0.16
4.6	9.335 ± 0.004	0.144 ± 0.010	0.022 ± 0.021	0.012 ± 0.022	0.120	0.029	39.31	25.00	5.615 ± 0.084	11.10 ± 0.16
4.9	8.558 ± 0.004	0.139 ± 0.011	0.020 ± 0.019	0.010 ± 0.019	0.097	0.028	33.98	27.92	5.600 ± 0.062	11.07 ± 0.12
5.2	8.067 ± 0.006	0.213 ± 0.013	0.091 ± 0.023	0.008 ± 0.032	0.486	0.045	26.54	4.46	5.796 ± 0.084	11.46 ± 0.17
5.5	8.249 ± 0.008	0.232 ± 0.019	0.119 ± 0.034	0.008 ± 0.058	0.563	0.050	26.27	2.18	5.853 ± 0.152	11.57 ± 0.30
Total/ Average	11.590 ± 0.001	0.144 ± 0.003	0.061 ± 0.002	0.021 ± 0.004		0.030		100.00	5.583 ± 0.028	

J = 0.001099 ± 0.000002
Volume $^{39}Ar_K$ = 964.5 E^{-13} cm^3 NPT
Integrated age = 10.85 ± 0.11 Ma

DK62 Hornblende

Laser power(%)	$^{40}Ar/^{39}Ar$	$^{38}Ar/^{39}Ar$	$^{37}Ar/^{39}Ar$	$^{36}Ar/^{39}Ar$	Ca/K	Cl/K	$\%^{40}Ar$ atm	f ^{39}Ar	$^{40}Ar^*/^{39}Ar_K$	Apparent age (Ma)
2.0	895.474 ± 0.022	0.904 ± 0.036	2.313 ± 0.029	3.018 ± 0.030	11.307	0.073	99.70	0.47	2.619 ± 19.108	5.18 ± 37.71
2.4	166.506 ± 0.007	0.165 ± 0.040	2.372 ± 0.017	0.543 ± 0.022	11.632	0.011	96.04	1.52	6.515 ± 3.465	12.85 ± 6.81
2.8	20.644 ± 0.008	0.048 ± 0.055	1.543 ± 0.019	0.052 ± 0.033	7.557	0.005	71.94	4.84	5.616 ± 0.497	11.08 ± 0.98
3.2	9.321 ± 0.006	0.064 ± 0.038	0.843 ± 0.018	0.012 ± 0.061	4.124	0.011	32.48	7.76	6.030 ± 0.218	11.89 ± 0.43
3.6	8.323 ± 0.007	0.141 ± 0.022	0.711 ± 0.017	0.009 ± 0.082	3.506	0.029	25.22	9.55	5.982 ± 0.211	11.80 ± 0.41
4.0	8.070 ± 0.005	0.346 ± 0.013	1.660 ± 0.013	0.008 ± 0.041	8.212	0.076	24.81	23.62	5.964 ± 0.105	11.76 ± 0.21
4.4	7.262 ± 0.005	0.415 ± 0.011	2.280 ± 0.013	0.006 ± 0.030	11.517	0.092	17.72	36.39	5.903 ± 0.064	11.65 ± 0.13
4.8	6.827 ± 0.006	0.568 ± 0.013	2.808 ± 0.014	0.006 ± 0.070	14.204	0.128	14.02	15.86	5.717 ± 0.130	11.28 ± 0.26
Total/ Average	14.695 ± 0.001	0.350 ± 0.003	5.242 ± 0.002	0.031 ± 0.006		0.053		100.00	5.925 ± 0.061	

J = 0.001097 ± 0.000002
Volume $^{39}Ar_K$ = 205.15 E^{-13} cm^3 NPT
Integrated age = 11.61 ± 0.24 Ma

TABLE A2. *(Cont.)*

DK64 Biotite

Laser power(%)	$^{40}Ar/^{39}Ar$	$^{38}Ar/^{39}Ar$	$^{37}Ar/^{39}Ar$	$^{36}Ar/^{39}Ar$	Ca/K	Cl/K	$\%^{40}Ar$ atm	f ^{39}Ar	$^{40}Ar^*/^{39}Ar_K$	Apparent age (Ma)
2.0	268.729 ± 0.030	0.277 ± 0.128	0.120 ± 0.181	0.913 ± 0.050	0.304	0.017	98.07	0.08	4.965 ± 11.000	9.83 ± 21.71
2.4	127.491 ± 0.010	0.134 ± 0.058	0.053 ± 0.098	0.425 ± 0.028	0.188	0.008	96.81	0.33	3.964 ± 3.308	7.85 ± 6.54
2.8	71.978 ± 0.006	0.089 ± 0.064	0.026 ± 0.153	0.230 ± 0.027	0.110	0.007	92.91	0.89	5.008 ± 1.806	9.91 ± 3.56
3.2	26.076 ± 0.007	0.070 ± 0.064	0.013 ± 0.172	0.078 ± 0.029	0.057	0.009	86.56	2.15	3.422 ± 0.655	6.78 ± 1.29
3.6	14.324 ± 0.006	0.062 ± 0.025	0.008 ± 0.086	0.036 ± 0.029	0.040	0.009	72.34	4.98	3.887 ± 0.310	7.70 ± 0.61
4.0	7.330 ± 0.005	0.059 ± 0.027	0.007 ± 0.043	0.011 ± 0.026	0.035	0.010	44.16	17.23	4.039 ± 0.090	8.00 ± 0.18
4.4	5.241 ± 0.005	0.058 ± 0.020	0.007 ± 0.049	0.004 ± 0.029	0.037	0.010	21.22	21.46	4.071 ± 0.040	8.06 ± 0.08
4.8	4.993 ± 0.005	0.059 ± 0.021	0.010 ± 0.054	0.003 ± 0.033	0.051	0.010	17.74	27.34	4.056 ± 0.037	8.03 ± 0.07
5.2	4.809 ± 0.005	0.059 ± 0.019	0.013 ± 0.021	0.003 ± 0.047	0.060	0.010	14.65	25.54	4.050 ± 0.042	8.02 ± 0.08
Total/ Average	7.461 ± 0.001	0.060 ± 0.005	0.026 ± 0.004	0.011 ± 0.005		0.010		100.00	4.046 ± 0.020	

J = 0.001100 ± 0.000002
Volume $^{39}Ar_K$ = 582.49 E^{-13} cm^3 NPT
Integrated age = 8.00 ± 0.08 Ma

DK66 Hornblende

Laser power(%)	$^{40}Ar/^{39}Ar$	$^{38}Ar/^{39}Ar$	$^{37}Ar/^{39}Ar$	$^{36}Ar/^{39}Ar$	Ca/K	Cl/K	$\%^{40}Ar$ atm	f ^{39}Ar	$^{40}Ar^*/^{39}Ar_K$	Apparent age (Ma)
2.0	280.511 ± 0.016	0.393 ± 0.033	0.158 ± 0.077	0.936 ± 0.026	0.742	0.047	98.94	0.54	2.884 ± 5.816	5.70 ± 11.47
2.3	54.942 ± 0.010	0.194 ± 0.043	0.128 ± 0.036	0.166 ± 0.022	0.600	0.034	89.37	2.08	5.642 ± 0.990	11.13 ± 1.95
2.6	34.671 ± 0.009	0.173 ± 0.031	0.217 ± 0.023	0.099 ± 0.022	1.018	0.032	84.51	2.77	5.159 ± 0.599	10.18 ± 1.18
3.0	23.928 ± 0.006	0.137 ± 0.027	0.425 ± 0.016	0.063 ± 0.029	1.996	0.026	76.60	3.54	5.355 ± 0.540	10.57 ± 1.06
3.4	51.165 ± 0.007	0.136 ± 0.028	0.319 ± 0.024	0.153 ± 0.020	1.499	0.022	88.50	3.57	5.748 ± 0.882	11.34 ± 1.73
3.8	30.995 ± 0.008	0.164 ± 0.047	0.716 ± 0.028	0.085 ± 0.029	3.367	0.031	79.88	2.94	5.988 ± 0.702	11.81 ± 1.38
4.2	19.007 ± 0.009	0.287 ± 0.022	2.187 ± 0.017	0.046 ± 0.024	10.317	0.061	69.23	8.37	5.717 ± 0.322	11.28 ± 0.63
4.6	10.505 ± 0.005	0.311 ± 0.011	2.582 ± 0.013	0.018 ± 0.022	12.188	0.068	44.66	26.16	5.737 ± 0.118	11.32 ± 0.23
5.0	11.901 ± 0.004	0.306 ± 0.010	2.648 ± 0.013	0.023 ± 0.020	12.502	0.067	51.83	36.68	5.682 ± 0.140	11.21 ± 0.28
5.5	7.726 ± 0.005	0.301 ± 0.012	2.620 ± 0.013	0.009 ± 0.029	12.371	0.066	24.15	13.36	5.669 ± 0.083	11.18 ± 0.16
Total/ Average	16.589 ± 0.001	0.283 ± 0.003	5.743 ± 0.002	0.039 ± 0.004		0.045		100.00	5.682 ± 0.049	

J = 0.001097 ± 0.000002
Volume $^{39}Ar_K$ = 295.61 E^{-13} cm^3 NPT
Integrated age = 11.18 ± 0.19 Ma

IR57 Biotite

Laser power(%)	$^{40}Ar/^{39}Ar$	$^{38}Ar/^{39}Ar$	$^{37}Ar/^{39}Ar$	$^{36}Ar/^{39}Ar$	Ca/K	Cl/K	$\%^{40}Ar$ atm	f ^{39}Ar	$^{40}Ar^*/^{39}Ar_K$	Apparent age (Ma)
2.0	327.937 ± 0.017	0.297 ± 0.052	0.089 ± 0.161	1.120 ± 0.028	0.351	0.017	101.04	0.71	–3.418 ± 7.283	–6.80 ± 14.52
2.4	51.469 ± 0.012	0.124 ± 0.051	0.184 ± 0.045	0.177 ± 0.029	0.770	0.018	101.83	2.57	–0.964 ± 1.404	–1.91 ± 2.79
2.8	6.756 ± 0.009	0.076 ± 0.038	0.023 ± 0.113	0.022 ± 0.035	0.093	0.013	95.27	5.96	0.282 ± 0.220	0.56 ± 0.44
3.2	3.007 ± 0.007	0.068 ± 0.042	0.015 ± 0.069	0.009 ± 0.041	0.060	0.012	91.18	15.88	0.230 ± 0.113	0.46 ± 0.22
3.6	1.921 ± 0.007	0.068 ± 0.030	0.016 ± 0.071	0.005 ± 0.085	0.066	0.012	82.06	18.10	0.305 ± 0.136	0.61 ± 0.27
4.0	1.305 ± 0.028	0.070 ± 0.047	0.019 ± 0.052	0.003 ± 0.056	0.077	0.013	68.57	27.88	0.370 ± 0.048	0.73 ± 0.09
4.5	0.990 ± 0.008	0.073 ± 0.027	0.023 ± 0.056	0.002 ± 0.077	0.093	0.013	54.06	21.86	0.406 ± 0.044	0.81 ± 0.09
5.0	1.341 ± 0.008	0.079 ± 0.046	0.028 ± 0.064	0.003 ± 0.126	0.112	0.015	67.65	4.90	0.345 ± 0.129	0.68 ± 0.26
5.5	17.501 ± 0.011	0.080 ± 0.103	0.021 ± 0.103	0.057 ± 0.055	0.078	0.013	95.04	2.13	0.816 ± 0.901	1.62 ± 1.79
Total/ Average	5.826 ± 0.004	0.074 ± 0.008	0.054 ± 0.006	0.019 ± 0.008		0.014		100.00	0.376 ± 0.039	

J = 0.001101 ± 0.000002
Volume $^{39}Ar_K$ = 508.57 E^{-13} cm^3 NPT
Integrated age = 0.57 ± 0.15 Ma

Notes:
Isotope production ratios: $(^{40}Ar/^{39}Ar)_K = 0.0302 \pm 0.00006$, $(^{37}Ar/^{39}Ar)_{Ca} = 1416.4 \pm 0.5$, $(^{36}Ar/^{39}Ar)_{Ca} = 0.3952 \pm 0.0004$, Ca/K = 1.83 ± 0.01($^{37}Ar_{Ca}/^{39}Ar_K$).
Neutron flux monitors: 28.02 Ma FCs (Renne et al., 1998) and MAC-83 (Sandeman et al., 1999).